Computational Modelling of Auxetic Materials and Structures

The Static and Dynamic Response of Materials and Structures with a Negative Poisson's Ratio

S. Bhattarai

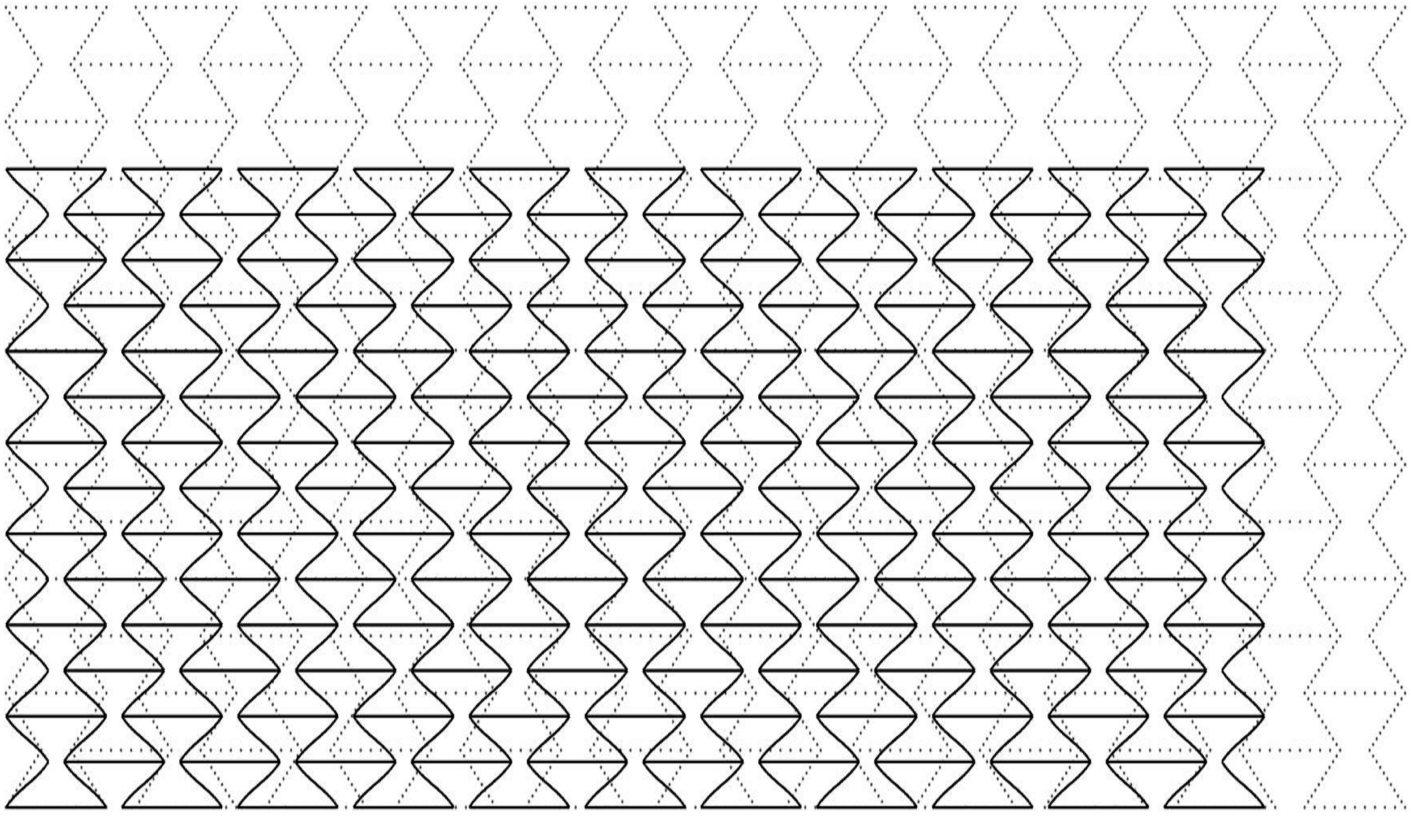

TU Delft

COMPUTATIONAL MODELLING OF AUXETIC MATERIALS AND STRUCTURES

THE STATIC AND DYNAMIC RESPONSE OF MATERIALS AND STRUCTURES WITH A NEGATIVE POISSON'S RATIO

by

S. Bhattarai

in partial fulfillment of the requirements for the degree of

Master of Science
in Civil Engineering

at the Delft University of Technology
to be defended publicly on Friday September 21, 2018 at 02:00 PM.

Student number:	4581644	
Project duration:	January 19, 2018 – September 21, 2018	
Thesis Committee:	Prof. dr. ir. L. J. Sluijs,	TU Delft, chair & mentor
	Dr. ir. J. Weerheijm,	TU Delft; TNO, mentor
	Dr. ir. A. Diederen,	TNO, supervisor
	Ir. L. J. M. Houben,	TU Delft, supervisor

This thesis is confidential and cannot be made public until September 30, 2021.

An electronic version of this thesis is available at `http://repository.tudelft.nl/`.

TU Delft Delft University of Technology

ACKNOWLEDGMENTS

This thesis presents the findings of the research carried out at the Computational Mechanics research group of Delft University of Technology. I would like to thank the people who helped me complete this thesis:

First of all, I would like to thank my mentor and the chair of my thesis committee, Bert Sluijs, for introducing me to the field of computational mechanics and giving me the opportunity to work on such an interesting and innovative topic. Despite having a busy schedule, you were always available to discuss my results, guide me and inspire me to push the boundaries. Thank you for your open door policy, motivating support and constructive feedback throughout the thesis. I would also like to thank, Jaap Weerheijm, for his guidance during the research. I have learned a lot from your critical remarks and invaluable feedback during the meetings. It was an enriching learning experience to work with the two of you.

Furthermore, I would like to thank André Diederen for the interesting discussions during the thesis meetings. Your suggestions were very insightful and helpful to complete this research. Similarly, I would like to thank Lambert Houben for being a part of my thesis committee, and helping me to complete all the formalities required during the graduation.

Finally, I would like to thank my family and friends for their unconditional love, help and support. My sincere gratitude to Justus en Louise van Effen Foundation for financing my studies and stay at The Netherlands. Friends in Delft, thank you for making my masters at TU Delft a memorable one. Especially my roommates, friends from room 6.54, Robbie, Naomi, Suraksha and Subigya, thank you for bearing with my talks about a material with a negative Poisson's ratio. My parents, Sumira, Bhinaju and Sansa, thank you for your love, support, motivation and patience throughout my masters.

Many thanks to everyone who helped me complete this thesis and MSc at TU Delft. Dhanyabaad!

S. Bhattarai
Delft, September 2018

ABSTRACT

Auxetic materials are increasingly used in the field of sports, defense, bio-medicine, and acoustic-filtering due to their unconventional behavior of exhibiting a negative Poisson's effect. The prospective use of auxetics to mitigate shock and impact forces have proven the relevance of research on auxetics. It becomes of paramount importance to understand their behavior and mechanics of deformation, especially regarding their response to dynamic loading conditions. Although auxetics have caught attention from several researchers, a detailed overview of computational modeling of auxetics is still missing and the deformation behavior of auxetics subjected to different loading conditions is an unfolded topic in structural mechanics.

In this thesis, computational tools are developed and validated to investigate the effect of auxeticity in a linear elastic continuum and a re-entrant honeycomb structure under different static and dynamic loading conditions. The possibility to assess the global behavior of an assembly of re-entrant honeycomb unit cells by the analysis of an equivalent continuum model with the same global dimensions and homogenized mechanical properties has been examined. The dynamic analysis of a continuum model of an isotropic auxetic material presented the influence of auxeticity in increasing the ratio of shear wave velocity to dilatation wave velocity. The finite element analysis of a simply supported auxetic beam subjected to impact at mid-span affirmed the hypothesis that in auxetics, the material flows towards the point of impact, thus increasing the indentation resistance. Computational challenges in analyzing a beam impact problem are discussed through the comparison of results from the standard finite element analysis, modal analysis, and the B-Bar method. It is recommended to further develop the proposed models to have a more robust approach on analyzing the continuum beam impact problem.

The assembly of a re-entrant honeycomb structure used in the finite element simulations were modelled with different unit cells by the variation of the two dominant geometrical parameters of the unit cell members. The results highlighted the strong correlation between the effective mechanical properties and the geometrical parameters, therefore indicating the possibility of achieving the desired values of the Poisson's ratio by simply modifying the necessary geometrical parameters. The results also showed that it is possible to obtain a Poisson's ratio more negative than -1 which can be exploited to design a displacement amplifier especially suitable for defense applications. The close comparison of the analytical and the computational results provided a groundwork to extend the numerical study to geometrical nonlinear analysis and other loading conditions like bi-axial loading and bending at the structural level. The comparison of results obtained from the analysis of an assembled cellular structure and an equivalent continuum model subjected to bi-axial loading and bending demonstrated the possibility of assessing the global behavior of cellular structure using the continuum model.

Dynamic analyses of a re-entrant honeycomb structure revealed that the wave propagation phenomenon in a re-entrant honeycomb structure is a result of several reflections, transmissions, mode conversions and superposition of waves occurring at the connection of cell members. The proportion of reflection, transmission and mode conversion of incident wave when it passes the connection can be controlled by varying the re-entrant angle between the cell members. For the lower frequency regime, the speed of wave propagation in re-entrant structures can be estimated using the continuum approach.

Furthermore, in a secondary study, the influence of the geometrical parameters of a re-entrant honeycomb structure to exhibit the stop-pass band was examined. Recommendations are provided for the further development of computational tools to analyze the three-dimensional and disordered re-entrant structures. In addition, it is also suggested to investigate the beam impact problem in the cellular model, the effect of rigidity of connection of cell members and research the possibility of having an isotropic re-entrant honeycomb structure as the present model is orthotropic in nature.

CONTENTS

1

INTRODUCTION

1.1. GENERAL OVERVIEW

Metamaterial, derived from a Greek word 'meta' meaning 'to go beyond', is defined as a material which possesses properties that usually do not exist in nature. The properties exhibited by metamaterials are unconventional, such as negative permeability, negative refractive index, negative incremental stiffness, negative compressibility, negative Poisson's ratio etc. The micro-structural arrangement of materials like metals, plastics and alloys compose metamaterials. The physical properties of the base materials that form the metamaterials are not responsible for such peculiar properties. Metamaterials exhibit unconventional and exotic properties solely based on their geometrical configuration and geometrical parameters.

Initially, metamaterials were designed, researched and used in the field of optics and electromagnetic. In the course of time, the notion of metamaterials has widened to various fields such as defense, structures, automotive, aerospace, textiles, sports, bio-medicine etc. A type of metamaterial which is drawing attention lately is auxetic material. Auxetic materials are defined as materials with a negative Poisson's ratio. Most of the materials found in nature have a positive Poisson's ratio in the range $0 \leq \nu \leq 0.5$. Such materials expand laterally when compressed in longitudinal direction, and contract when stretched. However, auxetic materials deform in an unconventional manner. They are observed to expand in both lateral and longitudinal direction when stretched, and contract when compressed.

Cork is an example of a material with a Poisson's ratio approximately equal to zero. The zero Poisson's ratio of cork makes it useful to seal bottles. Due to zero Poisson's ratio, the cork does not expand/contract in radial direction when compressed at the top to insert into a bottle. The studies have shown that the micro-structure of the cork is responsible for the zero Poisson's ratio it exhibits. Similar micro-structures when designed with specific geometric configuration and parameters can exhibit atypical negative Poisson's ratio as well.

For linear elastic isotropic materials, the decrease in the value of Poisson's ratio relates to an increase in shear and indentation resistance. This feature of auxetics is favorable to mitigate the shock and impact force on a structure. When an auxetic structure is subjected to impact, the material flows towards the point of impact rather than flowing away from it. This has increased the prospects of using auxetics in protective wears like helmets, knee pads, bullet proof vests etc.

Besides their increasing use in protective devices, auxetics are gaining popularity in various other applications like bio-medicine, textiles and fashion apparels. In addition to exhibiting a negative Poisson's effect, micro-structures assembled to form auxetics are also capable of filtering propagating waves in a certain frequency range. This feature is called band gap, and is used in photonic applications, acoustic filtering etc. All these exotic properties exhibited by auxetics have raised interests in understanding the response of auxetic structures subjected to various static and dynamic loading conditions. Since the first time auxetics was introduced in the 1980s, numerous attempts have been made to study, design and manufacture auxetic structures. However, many issues related to their behavior still remain an unfolded topic in the structural mechanics domain.

This thesis aims to examine the response of auxetics from the perspective of both continuum modelling and micro-structure modelling. Computational tools and models are developed to understand the mechanics of auxetic structures. A detailed overview of the numerical analysis of auxetic continuum and auxetic cellular structure will be presented with focus on their dynamic characteristics.

1.2. RESEARCH OBJECTIVES

The goal of this thesis is to examine the deformation behavior of a material with negative Poisson's ratio when subjected to different loading conditions. The unconventional behavior of continuum models and honeycomb cellular structures exhibiting a negative Poisson's effect is studied through computational analysis. The effect of negative Poisson's ratio on the speed of wave propagation and impact resistance is to be investigated. The computational tools required to realize these objectives are built upon a finite element code programmed at Delft University of Technology for academic purposes [23, 25].

The following research questions are formulated to achieve the objectives of the research:

Box 1.2.1: Research Questions

1. How is dynamic wave propagation affected in an auxetic continuum?
2. How can a cellular structure be modelled in order to exhibit a negative Poisson's ratio?
3. How do auxetic cellular structures respond to dynamic loading conditions?
4. What are the mechanical requirements of a cellular structure elements and nodes to enable auxetic dynamic behavior?

1.3. RESEARCH METHODOLOGIES

The research was initiated with a literature review to understand the theoretical background of auxetic structures. The literature studies highlighted the structures that exhibit auxeticity, geometrical and mechanical features of such structures, characteristics and application of auxetics, and previous researches on the topic. As the research is focused on examining the behavior of auxetic structures, computational tools are developed to run the numerical analysis of auxetic structures subjected to different static and dynamic loading conditions. The finite element codes programmed by Wells [25] and van der Meer [23] in MATLAB were modified to include dynamic analysis and various other tools required for the post-processing of results. The finite element code was validated using different numerical techniques and compared with commercial finite element software. The research will be limited to the study of a two-dimensional continuum model and a re-entrant honeycomb micro-structure using linear elastic material properties.

1.4. THESIS OUTLINE

The thesis is structured in such a way that all topics of the research are addressed separately in detail but also provides a coherent connection with each other. Chapter 2 presents a critical review of literature related to auxetic structures, characteristics of auxetics, different types of cellular structures exhibiting auxeticity, previous research overview and the application of auxetics. The first research question is addressed in chapters 3 and 4. These chapters highlight the deformation behavior of an auxetic continuum loaded under different static and dynamic loading conditions. Chapter 5 focuses on the second and fourth research questions. Re-entrant honeycomb structures are analyzed for various static loading conditions to examine the deformation mechanism of a micro-structure exhibiting auxeticity. The global behavior of the assembly of re-entrant honeycomb unit cells are related to the behavior of a continuum model with the same geometrical dimension and effective mechanical properties. This creates a logical connection between chapters 3 and 5. In chapter 6, wave propagation in a re-entrant honeycomb unit cell and structure formed from the assembly of several unit cells is investigated. The issues related to the third and fourth research question are discussed in this chapter. In addition, the wave speed in re-entrant honeycomb structure computed from numerical analyses is compared with the continuum approach estimation. Chapter 7 presents an interesting application of re-entrant -honeycomb cellular structures, the stop-pass band. The possibility of having an isotropic re-entrant honeycomb structure is also discussed in chapter 7. Finally, chapter 8 concludes the thesis by presenting the main conclusions of the present research and recommendations for the further work.

2

LITERATURE REVIEW

Generally, when a material is stretched, it not only gets longer in the direction of stretch, but also contracts in the lateral direction. Similarly, when a material is compressed, it expands in the lateral direction. This behavior of a material is characterized by a property, the Poisson's ratio (ν). The Poisson's ratio (ν), which was invented by a mathematician Simeon Dennis Poisson (1787-1840) is defined as the negative ratio of transverse strain to longitudinal strain. Since tensile deformation is considered positive and compressive deformation is considered negative, the negative ratio of transverse strain to longitudinal strain generally gives a positive value for the Poisson's ratio. However, auxetic materials behave opposite; auxetic materials exhibit a negative Poisson's effect i.e. these materials expand laterally when stretched, and compress laterally when compressed longitudinally. The deformation behavior of an auxetic material and conventional material subjected to uniaxial tension is shown in figure 2.1.

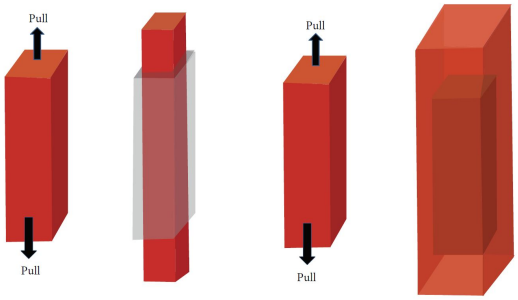

Figure 2.1: Deformation behavior of auxetic and conventional materials [14]

2.1. BACKGROUND

Although materials with a negative Poisson's ratio have been envisioned by classical elasticity theory, the first documented evidence about materials having a negative Poisson's ratio was found in a book by Love in 1944[16]. According to classical elasticity theory, an isotropic material can have a Poisson's ratio (ν) between -1 and 0.5. Similarly, studies have shown that the Poisson's ratio for anisotropic materials can be positive or negative as long as the strain energy density function is positive [16, 17]. However, the research on negative range of Poisson's ratio started only at the end of the twentieth century. It implies that the Poisson's ratio has been much less studied among other elastic constants like Young's modulus (E), shear modulus (G) and bulk modulus K [2].

After Love, Gibson realized the negative Poisson's effect in 1982 in a two-dimensional silicone rubber and aluminum honeycomb deforming by the flexure of ribs [3, 16]. The concept of fabrication of foams with negative Poisson's ratio was reported for the first time by Lakes in 1987 [16, 17]. However, the terminology "auxetics" came into use only in 1991 when Evans et al. first fabricated the microphorous polyethene with negative Poisson's ratio [16]. The word "auxetic" is derived from the Greek word "$\alpha\upsilon\chi\eta\zeta\iota\zeta$" which means "that which tends to increase".

Auxetic materials are now gaining interest from researchers and scientists due to their unique properties as compared to materials with the positive Poisson's ratio. According to classical continuum mechanics elasticity theory, various mechanical properties such as: indentation resistance, fracture toughness, shear modulus etc. are higher for auxetic materials than for conventional materials. For instance, indentation resistance and shear modulus of an isotropic linear elastic material is inversely proportional to $(1 - \nu^2)$ and $(1 + \nu)$ respectively. In a conventional material, the maximum indentation resistance is obtained with the Poisson's ratio $\nu = 0.5$, i.e. the factor is equal to $(1 - 0.5^2)^{-1} = 1.33$. Whereas for an auxetic material, even higher indentation resistance can be obtained with the Poisson's ratio $\nu < -0.5$, i.e. the factor greater than $(1 - (-0.5)^2)^{-1} = 1.33$.

The increase in indentation resistance of an auxetic material also has a physical basis. When a conventional material is subjected to impact loading, the force compresses the material, and the material below the impact load spreads in lateral direction [2]. This leads to the reduced density in the area around the impact which is characterized by a formation of large dent implying low indentation resistance. However, when an auxetic material is subjected to impact loading, the auxetic material will behave opposite. As the Poisson's ratio is negative, the material immediately below the impact contracts laterally, thus making the area around the impact point denser. This leads to the increased indentation resistance, resulting in the formation of a smaller dent as compared to nonauxetic materials. The difference in deformation behavior under impact loading in an auxetic and conventional material is illustrated in figure 2.2.

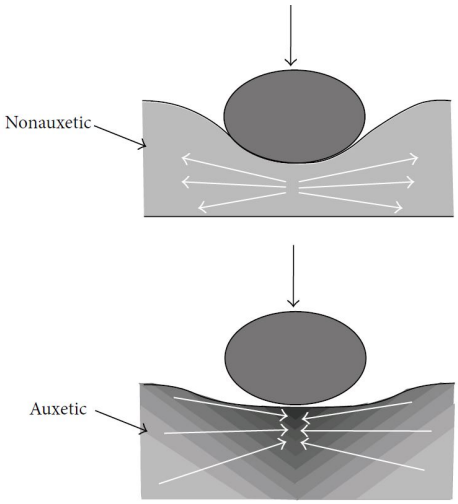

Figure 2.2: Indentation resistance of auxetic and nonauxetic materials [14]

In a linear elastic isotropic material, the material properties Young's modulus (E) and shear modulus (G) are related by: $G = \frac{E}{2(1+\nu)}$. For a conventional material, G is always smaller than or equal to $0.5E$. However, for an auxetic material, the shear modulus G is found to be higher than Young's modulus E when Poisson's ratio is less than -0.5. This makes auxetic materials more favorable in shear dominant situations.

Also, auxetic honeycomb structures tend to produce a synclastic (domed) surface when subjected to an out of plane bending moment. This behavior is observed due to the effective in-plane Poisson's ratio being negative [13]. In contrast, the conventional honeycomb structures produce a saddle shaped structure when it is bent out-of-plane which is less desirable than the dome shaped doubly curved synclastic shape. The response of the auxetic and conventional material subjected to out of plane bending moment is shown in figure 2.3. The various properties discussed above make the auxetic material a material of interest from perspective of use in military, sports, bio-medical, automobile and civil engineering applications. The applications of auxetic materials are further elaborated in Section 2.3.

2.2. TYPES OF AUXETIC MATERIALS

The existence of natural auxetic materials produced a controversial discussion among researchers in the past[16]. Experts in classical mechanics believed no natural materials could exhibit an auxetic effect by the virtue of their physical properties because of various constraints. The reasoning was based on the restriction according to thermodynamics and a dynamic approach. It was argued that the ratio of Rayleigh wave velocity

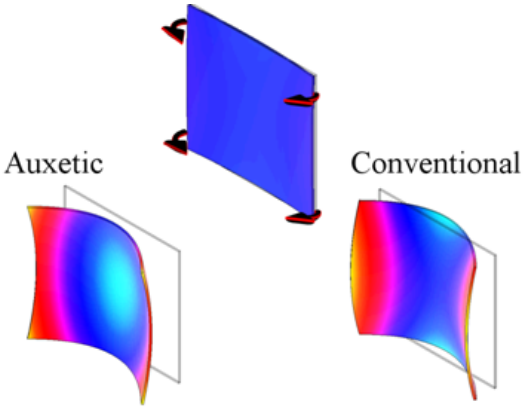

Figure 2.3: Anticlastic and Synclastic shape produced by auxetic and conventional materials subjected to out of plane bending

to shear wave velocity in a material is only dependent on the material's Poisson's ratio. The available expression of the ratio showed that the Poisson's ratio can only lie between 0 and 0.5, thus ruling out the possibility of auxetics [11, 16]. However, a group of researchers believed that natural materials such as cancellous bone, living cat skin, cow teat skin, natural minerals such as $\alpha-$Cristobalite (SiO_2), pyrolytic graphite, single crystals such as pyrite (FeS_2), and some type of zeolites such as siliceous zeolite MFI-Silicates exhibit auxetic effect [16].

Although the existence of natural auxetic materials remain controversial, man-made auxetic materials have been designed, manufactured, studied and used for quite some time now. Auxetic behavior is realized by adapting to a necessary geometrical configuration in cellular structures. Achieving auxeticity in cellular structures makes it more interesting because of the light weight of cellular structures. The cellular structures with re-entrant shape, chiral structures etc. are examples of man-made auxetic materials. These materials exhibit an auxetic effect solely due to their geometrical configuration and deformation mechanism.

The auxetic cellular structures are classified into re-entrant structures, chiral structures and rotating units based on their deformation mechanism [17]. Each group are further subdivided into various types or variants based on their geometrical configuration and shape. The deformation mechanism and geometry of Re-entrant cellular structures, Chiral structures and Rotating units are briefly described in this section.

Re-entrant Structures: Re-entrant structures are named because of their geometry. The word re-entrant in geometry means an angle greater than 180° i.e. negative angles. Thus, as the name suggests, these structures have a re-entrant configuration and are therefore pointed inwards. The initial re-entrant honeycomb structure was proposed by Gibson et al. [4]. The geometry of a two dimensional conventional and re-entrant honeycomb structures are shown in figure 2.4. Gibson et al. described the deformation mechanism in a honeycomb cellular structure, and proposed expressions for the Poisson's ratio v and effective Young's modulus E in the loading direction. According to Gibson et al. [4], the Poisson's ratio and Young's modulus in the direction of loading in a honeycomb cellular structure are given by:

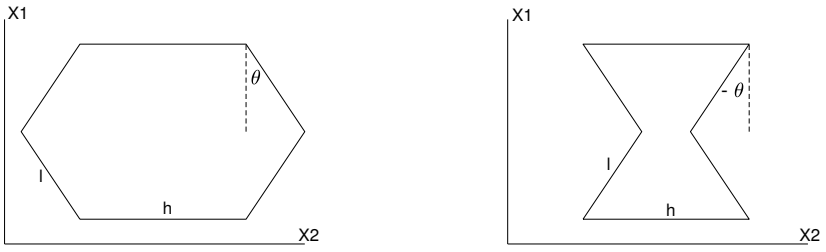

(a) Conventional honeycomb (b) Re-entrant honeycomb

Figure 2.4: Unit cell of hexagonal honeycomb

Loading in X1 direction:

$$\nu_1 = \frac{cos^2\theta}{(h/l + sin\theta)sin\theta} \tag{2.1}$$

$$E_1 = E_s\left(\frac{t}{l}\right)^3 \frac{cos\theta}{(h/l + sin\theta)sin^2\theta} \tag{2.2}$$

Loading in X2 direction:

$$\nu_2 = \frac{(h/l + sin\theta)sin\theta}{cos^2\theta} \tag{2.3}$$

$$E_2 = E_s\left(\frac{t}{l}\right)^3 \frac{(h/l + sin\theta)}{cos^3\theta} \tag{2.4}$$

where h, l, t, θ and E_s represent the length of horizontal rib, the length of inclined rib, thickness of the rib, angle between vertical and the inclined rib, and Young's modulus of the base material. Observing equation 2.2 and equation 2.3, it can be easily noticed that the auxetic effect can be realized on adopting a re-entrant honeycomb shape i.e. $\theta < 0$. On the proposed model, the auxetic effect is achieved because the inclined ribs move outward when tensile load is applied, and similarly, the inclined ribs move inward when a compressive load is applied. The deformed re-entrant honeycomb structure under compressive load in X1 direction is shown in figure 2.5.

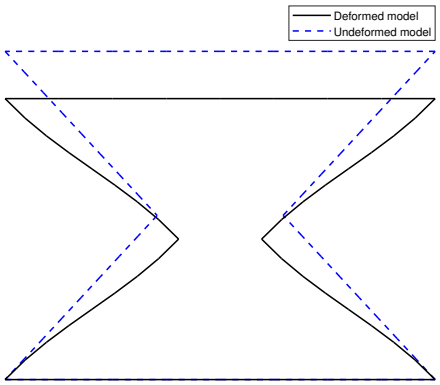

Figure 2.5: Deformation of a unit cell of re-entrant honeycomb loaded in X1 direction

Other variants of re-entrant auxetic structures are also available now. Re-entrant triangular structures and re-entrant star shaped structures are other variants of re-entrant auxetic structures. The auxetic behavior depends on the dimensions of the geometrical parameters including the re-entrant angle on these structures as well.

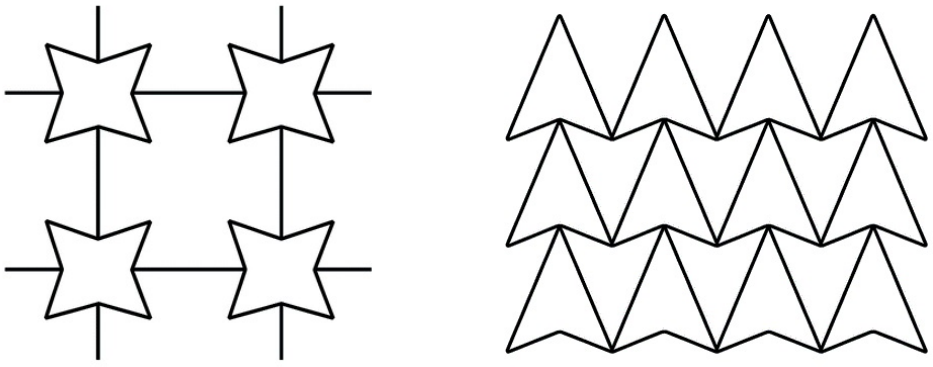

(a) Star shaped re-entrant variant

(b) Triangular re-entrant variant

Figure 2.6: Variants of re-entrant structures [9]

Chiral Structures: These structures consist of rigid rings and ligaments tangentially attached to the rings [17]. The word chiral means an object which is non-superimposable on its mirror image. The rigid rings are attached to distinct ligaments around it, therefore making the system distinguishable from its mirror image.

The auxetic effect is achieved due to the winding or un-winding of the ligaments attached to the rings when the rigid rings start to rotate [17]. Prall and Lakes performed a theoretical and experimental research on the deformation mechanism and auxetic behavior of chiral units [16, 17]. The in-plane deformations of chiral units resulted to a Poisson's ratio of about -1. A model of the chiral unit cell, and the deformation of the chiral structure are shown in figure 2.7. The chiral structures have been developed into different variants. Rotachiral type and a three dimensional chiral structures are other variants of the chiral auxetic structures. Rotachiral type is a blend of chiral type and the missing rib model. This variant of a chiral auxetic structure can exhibit a high auxetic effect in out-of-plane loading [17].

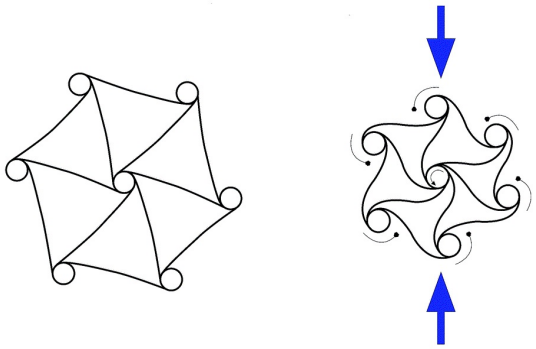

Figure 2.7: Deformation of a chiral structure [9]

Rotating Polygons: In rotating polygons auxetic structures, the auxetic effect is achieved due to the rotation of rigid polygons which are hinged with each other [17]. There are different variants of rotating polygons auxetic structures such as: rotating squares, rotating rectangles, rotating triangles, rotating rhombi etc. A rotating square is constrained not to shear and exhibit a Poisson's ratio equal to -1. Generally, rotating rectangles are anisotropic in nature, and the Poisson's ratio depends on the geometrical dimensions and the direction of loading. However, a variant of rotating rectangle which has the empty loop as a parallelogram is isotropic in nature with a Poisson's ratio equal to -1. The Poisson's ratio in this variant of a rotating rectangle is independent of dimensions and direction of loading. Figure 2.8 shows the variant of rotating rectangles which has rhombus in the empty loop. The figure shows the rotating rigid rectangular structure at rest and in deformed position. It can be observed that the application of a tensile force in longitudinal direction yields the structure to extend in the vertical direction as well.

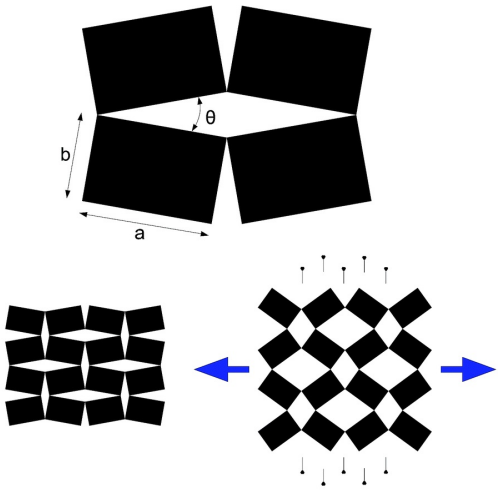

Figure 2.8: Deformation of a rotating rigid rectangules [9]

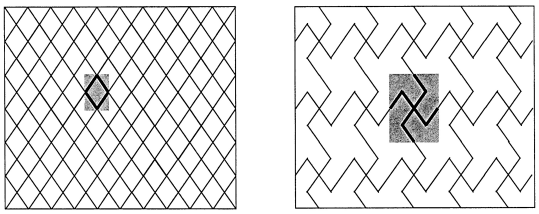

Figure 2.9: Models with the intact ribs and the missing ribs, with unit cells shaded [20]

Besides re-entrant, chiral and rotating polygons auxetic structures, other man-made auxetic structures also exist, such as: Missing rib model, Nodule fibril model etc. In a missing rib model, selected ribs are removed from a structure to have the auxetic effect. After the removal of ribs, the structure deforms in a similar way in both directions when extended or compressed. The missing rib-model is shown in figure 2.9.

A nodule-fibril model of auxetic structure is formed by the connection of nodules and fibrils. On an application of the tensile force, the fibrils cause outward motion of lateral nodule thus resulting in an auxetic effect. The mechanism of nodule-fibril model is shown in figure 2.10.

A detailed description of the geometry and deformations mechanism for each variant of auxetic structures are reviewed in [17]. The similarity among all variants is that the auxetic effect is achieved solely by the virtue of a structure's geometrical arrangement, size and the loading direction. The re-entrant honeycomb structure proposed by Gibson [4] is selected for the research in this thesis. The static and dynamic response of re-entrant honeycomb structures with varying size and re-entrant angle are examined to realize the research objectives.

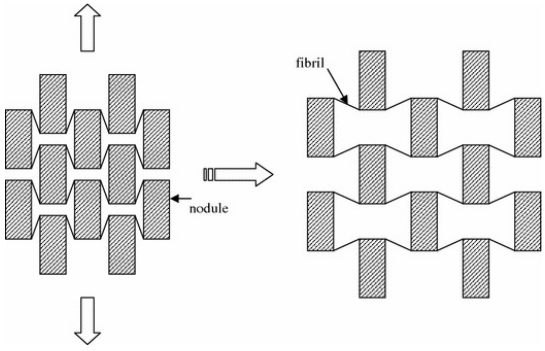

Figure 2.10: Deformation of a nodule-fibril model of auxetic structure[1]

2.3. APPLICATION OF AUXETIC MATERIALS

Enhanced mechanical properties exhibited by auxetic structures have already been briefly highlighted earlier. The increasing use of auxetic structures in various fields of application has further increased the reason to understand and research more about its mechanism and behavior. The application of auxetic structures in sports, defense, acoustic filtering, and bio-medicine is briefly highlighted in this section.

The innovative use of auxetic structures is as a smart bandage and smart filters [14]. When a filter made from auxetic foams is stretched in one direction, the pores become larger because of negative Poisson's ratio. The enlargement of the pores depends on the magnitude of the Poisson's ratio and stretching force. When the auxetic foam is absorbed with medicines, it can be used as a smart bandage. On the swelling of the wound such that the smart bandage is pushed, the medication impregnated in the bandage will be released. The amount of medication that is released depend on how much the wound swells up, thus resulting in a smart and effective way of treating the wound. The auxetic smart bandage is shown in figure 2.11(b).

Another bio-medical application of auxetic structures is in a dilator for opening the cavity during the cardiac surgery. Due to the negative Poisson's ratio, the flexible auxetic PTFE (polytetrafluroethylene) hollow rod or sheath under tension undergoes lateral expansion thus exhibiting the auxetic effect [2, 14]. The lateral expansion of the auxetic rod results in the opening of the artery for the use in surgery. The dilator using an auxetic end sheath for opening the artery in heart surgery is shown in figure 2.11(a).

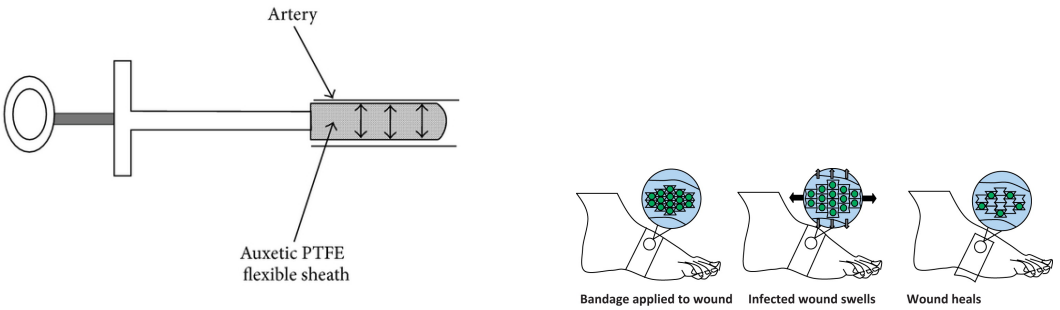

(a) Dilator using an auxetic rod for opening artery in cardiac surgery [14]

(b) Smart Bandage using auxetic structures [24]

Figure 2.11: Bio-medical application of Auxetic structures

Auxetic materials can also be useful in manufacturing safer artificial blood vessels. The wall thickness of artificial blood vessels made from conventional materials is reduced in response to the pulse of the blood flow [2]. However, in a blood vessel made from auxetic structures, the wall thickness increases with the blood flow thus reducing the chance of vessel rupture caused by the thinning of the wall.

Another widely used application of auxetic materials is to mitigate the impact. The shock absorption characteristics exhibited by auxetic structures have increased their prospect to be used in the sports and defense field. In addition to the shock absorption characteristics exhibited by them, the cellular auxetic structures are light as well. Therefore, it increases the comfort as well when used as sports protective gears, like: pads, gloves, helmets etc [17]. Synclastic curvature exhibited by auxetic structures when subjected to out of plane bending can be exploited to use them as protective wears for skull and knees. The auxetic materials used for such purposes follow the curvature of skull and knees when subjected to bending thus providing the required protection. Higher indentation resistance of auxetic structures also make them favorable to be used in batting pads, bullet proof vests, football shin pads, running shoes etc [17].

Besides, the auxetic structures can also be used as acoustic filters due to the band gaps characteristics exhibited by them. Auxetic structures are manufactured to isolate or omit the frequency in the unwanted range. Other potential application of auxetic materials are in fabrics, garments, fashion apparels, footwear, surgical implants etc. [2, 17] The use of auxetic structures have proven to be promising and advantageous from numerous prospective. These applications have increased the relevance of the research on auxetic structures. The mechanics and response of auxetic structure subjected to different loading conditions remain an unfolded topic in the field of structural mechanics.

2.4. WAVE PROPAGATION IN AUXETIC SOLIDS

In a linear elastic isotropic material, there are only two independent material constants, the Young's modulus E and the Poisson's ratio ν. For a given value of the Young's modulus E, mechanical properties only depend on the value of the Poisson's ratio ν. The effect of auxeticity on the shear modulus, indentation resistance, fracture toughness etc. have already been discussed in Section 2.1. The increased indentation resistance exhibited by an isotropic auxetic material makes it a material of interest in the field of impact dynamics. Therefore, the effect of auxeticity on dynamic wave propagation in a solid is a topic of interest. In this section, the effect of a negative Poisson's ratio on the speed of a longitudinal wave, plane wave of dilatation and plane wave of distortion in an auxetic will be discussed. Later, special features of dynamic wave propagation in a re-entrant cellular solid will also be briefly described.

Longitudinal Wave: A bar is in a one-dimensional stress state during the propagation of a longitudinal wave as the lateral stresses are insignificant compared to the longitudinal stress i.e. $\sigma_y = \sigma_z = 0$ [11]. During the propagation of the longitudinal wave in auxetic structures, the longitudinal and transverse expansion occur at the same region. Thus, it leads to a larger density variation when longitudinal wave is propagating through a material with a negative Poisson's ratio [11].

The relation between strain and stress in a linear elastic continuum is given by:

$$\boldsymbol{\varepsilon} = \mathbf{C}\boldsymbol{\sigma} \tag{2.5}$$

where $\boldsymbol{\varepsilon}$ is the strain vector, $\boldsymbol{\sigma}$ is the stress vector and $\mathbf{C}$ is the elastic compliance matrix given by:

$$\mathbf{C} = \frac{1}{E}\begin{bmatrix} 1 & -\nu & -\nu & 0 & 0 & 0 \\ -\nu & 1 & -\nu & 0 & 0 & 0 \\ -\nu & -\nu & 1 & 0 & 0 & 0 \\ 0 & 0 & 0 & 2(1+\nu) & 0 & 0 \\ 0 & 0 & 0 & 0 & 2(1+\nu) & 0 \\ 0 & 0 & 0 & 0 & 0 & 2(1+\nu) \end{bmatrix} \tag{2.6}$$

According to the compliance relation, it is known that even in a 1D stress state, $\varepsilon_x, \varepsilon_y$ and therefore u_x, u_y are not equal to 0 except when Poisson's ratio is equal to zero. It means the longitudinal wave motion in a bar is a 1D stress and 3D deformation state.

Now, in a bar with density ρ, a small element of dimension dx with the cross-sectional area A and mass $dm = \rho.A.dx$ is considered. Then, the equation of motion after time t in the longitudinal direction due to the internal axial force is given by:

$$A\left(\sigma_x + \frac{\partial \sigma_x}{\partial x}dx\right) - A\sigma_x = dm\frac{\partial^2 u_x}{\partial t^2} \tag{2.7}$$

Using the definition of strain and $\sigma_y = \sigma_z = 0$ in equation 2.5, a relation between σ_x and u_x is found to be:

$$\sigma_x = E\varepsilon_x = E\frac{\partial u_x}{\partial x} \tag{2.8}$$

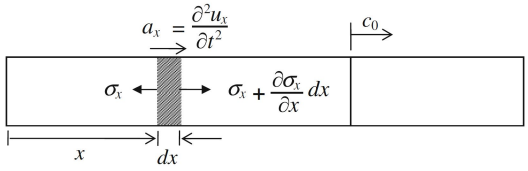

Figure 2.12: Section considered for the equation of motion [11]

Substituting equation 2.8 and the expression of dm in equation 2.7, it is obtained that:

$$\frac{\partial^2 u_x}{\partial t^2} = c_\circ^2 \frac{\partial^2 u_x}{\partial x^2} \tag{2.9}$$

where $c_\circ$ is the longitudinal wave velocity, and is equal to:

$$c_\circ = \sqrt{\frac{E}{\rho}} \tag{2.10}$$

Plane Wave of Dilatation: The plane wave of dilatation propagates within a medium without rotation, and causes a volume change. For the dilatational wave, the deformation is only allowed in the direction of wave propagation, meaning lateral strains are equal to zero whereas lateral stresses are significant when Poisson's ratio is non-zero. Therefore, the case of the plane wave of dilatation is 3D stress state and 1D deformation state [11]. The plane wave of dilatation propagates with a velocity c_1 in the medium which depends on the effective Young's modulus E'.

Since $\varepsilon_y = \varepsilon_z = 0$ for the plane wave of dilatation, the lateral stresses σ_y and σ_z are due to the Poisson's effect which is the same in all directions for an isotropic solid. Therefore, using $\sigma_y = \sigma_z$ and $\varepsilon_y = \varepsilon_z = 0$ in equation 2.5, it results to:

$$\sigma_y = \sigma_z = \frac{\nu}{1-\nu}\sigma_x \tag{2.11}$$

Using the relation obtained in equation 2.11, the relation between ε_x and σ_x from equation 2.5 is found to be:

$$\varepsilon_x = \frac{1}{E}\left(1 - 2\frac{\nu^2}{1-\nu}\right)\sigma_x \tag{2.12}$$

which can be rewritten as:

$$\varepsilon_x = \frac{(1+\nu)(1-2\nu)}{E(1-\nu)}\sigma_x \tag{2.13}$$

Therefore, the effective Young's modulus for a plane wave of dilatation can be expressed as: $E' = \frac{E(1-\nu)}{(1+\nu)(1-2\nu)}$. Using the effective Young's modulus in equation of motion for longitudinal wave, the velocity (c_1) of plane wave of dilatation is found to be:

$$c_1 = \sqrt{\frac{E'}{\rho}} = \sqrt{\frac{E(1-\nu)}{\rho(1+\nu)(1-2\nu)}} \tag{2.14}$$

Plane Wave of Distortion: The plane wave of distortion also commonly known as the Shear wave generates shear in a medium and does not contribute to a volume change. For the plane wave of distortion, the displacement is only allowed in one of the lateral directions. The deformations in the other two directions (longitudinal and other lateral direction) are constrained.

Now, considering a small element of dimension dx having a cross-sectional area A and mass $dm = \rho A dx$, the equation of motion in the transverse y-direction is [11]:

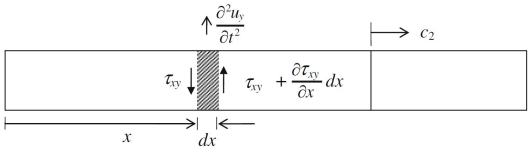

Figure 2.13: Section considered for the equation of motion [11]

$$A\left(\tau_{xy} + \frac{\partial \tau_{xy}}{\partial x} dx\right) - A\tau_{xy} = dm \frac{\partial^2 u_y}{\partial t^2} \tag{2.15}$$

Using $u_x = 0$ for the plane wave of distortion case in equation 2.5 the relation between τ_{xy} and u_y is found to be:

$$\gamma_{xy} = \frac{\partial u_x}{\partial y} + \frac{\partial u_y}{\partial x} = \frac{\partial u_y}{\partial x} \tag{2.16}$$

$$\tau_{xy} = \frac{E}{2(1+\nu)}\gamma_{xy} = \frac{E}{2(1+\nu)}\frac{\partial u_y}{\partial x} \tag{2.17}$$

Substituting the value of dm, and equation 2.16 in the equation of motion (equation 2.15) gives:

$$\frac{\partial^2 u_y}{\partial t^2} = c_2^2 \frac{\partial^2 u_y}{\partial x^2} \tag{2.18}$$

where c_2 is the velocity of a plane wave of distortion and is given by:

$$c_2 = \sqrt{\frac{E}{2\rho(1+\nu)}} \tag{2.19}$$

Now, observing the wave velocities $c_\circ, c_1, c_2$ for constant values of Young's modulus E and density ρ, the dilatation wave velocity c_1 and the distortion wave velocity c_2 are found to vary with Poisson's ratio ν. According to the classical elasticity theory, the Poisson's ratio in a linear elastic isotropic solid can vary between -1 and +0.5. The variation of wave velocities c_1 and c_2 in the allowable range of Poisson's ratio ν for E = 1 Nmm^{-2} and ρ = 1 kgm^{-3} is shown in figure 2.14. The wave velocities are obtained for a unit value of elastic modulus and density.

As it can be observed in figure 2.14, both the dilatation wave velocity c_1 and the distortion wave velocity c_2 continue to increase with an increase in the auxetic effect. The distortion wave velocity which is considerably smaller than the dilatation wave velocity for positive Poisson's ratio values, now approaches towards

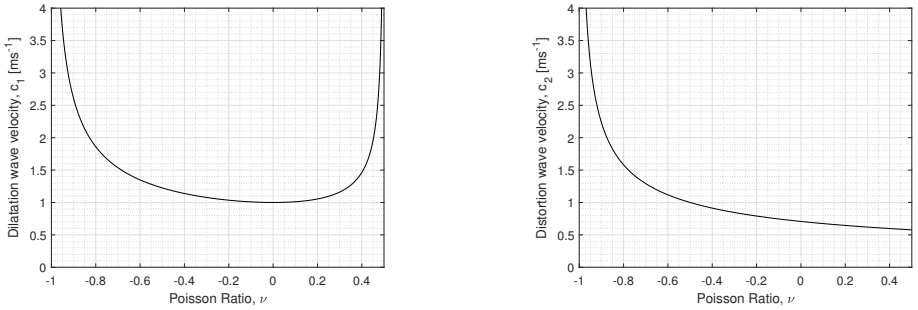

(a) Dilatation Wave Velocity (b) Distortion Wave Velocity

Figure 2.14: Variation of wave velocities with respect to Poisson's ratio

the dilatation wave velocity in the auxetic range ($\nu < 0$). From equations 2.14 and 2.19, the ratio between two wave velocities is found to be:

$$\frac{c_1}{c_2} = \sqrt{\frac{2(1-\nu)}{1-2\nu}} \tag{2.20}$$

The variation of the ratio of wave velocities with Poisson's ratio (ν) is shown in figure 2.15.

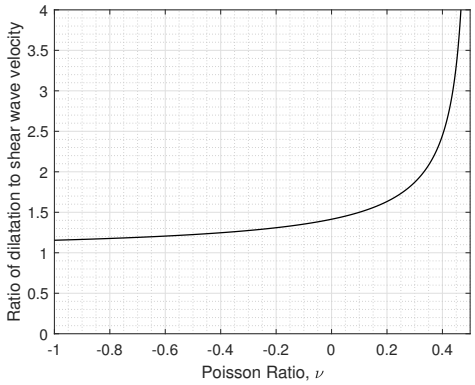

Figure 2.15: Ratio of dilatational wave velocity to distortion wave velocity

It can be observed in figure 2.15 that the ratio decreases from infinity at extreme positive Poisson's ratio ($\nu = 0.5$) to approximately 1.15 at extreme negative Poisson's ratio ($\nu = -1$). As the shear modulus G already surpasses the Young's modulus E for the values of Poisson's ratio $\nu < -0.5$, the distortion wave velocity is found to be higher than the longitudinal wave velocity for the values of the Poisson's ratio $\nu < -0.5$. However, the distortion wave velocity does not exceed the dilatation wave velocity in an isotropic solid which can also be observed in figure 2.15. The analytical ratio of dilatation and distortion wave velocities presented in figure 2.15 will be checked computationally later in Section 3.

Since the auxeticity in practice is realized through a cellular structure, wave propagation in an auxetic cellular structure is an interesting and important topic to study. In an auxetic cellular structure, the effective mechanical properties such as Young's modulus, shear modulus, effective density etc. is dependent on the size and shape of the structure. Therefore, the speed of wave propagation in an auxetic cellular structure also depends on several of the geometrical parameters, such as: length and width of the beams forming cellular structures, angle between them, density of the base material (ρ), Young's modulus and shear modulus of the base material (E, G) etc.

Besides the wave velocity, the size, geometrical arrangement and periodicity of cellular structures also significantly affect other wave propagation characteristics like wave attenuation, guidance or steering of waves within a cellular structure [17]. The periodicity of a cellular structures in fact results in a destructive wave interference process in a certain frequency range [6]. This wave motion characteristics exhibited by a cellular

structure is known as stop bands or band gaps which represents the frequency range over which the wave motion cannot occur in the structure [15]. Since the frequency range in which band gaps occur depend on the size and shape of the structure, an auxetic cellular structure can be designed to achieve band gaps in any required frequency limit.

2.5. PREVIOUS RESEARCH OVERVIEW

The realization of a material with unconventional Poisson's ratio, development of the concept and finally the fabrication of the prototype in 1980s gave a direction and inspiration to the study into auxetic materials. Many researches and studies have been carried out since then to explore the innovative application of auxetic materials due to the novel properties exhibited by them. Although numerous researches are carried out in all types of auxetic structures (re-entrant structures, chiral structures, rotating polygons etc.), this section aims to review key researches in re-entrant structures only.

Gibson [4] studied the geometry of a two-dimensional hexagonal honeycomb structure in 1981. The deformation mechanism of a honeycomb unit cell under uni-axial, bi-axial and shear loading is described in detail. Also, the expression for determining relative density of the structure, Poisson's ratio and effective Young's modulus in loading direction, effective shear modulus are derived. Gibson explained that the primary deformation in a hexagonal honeycomb structure is due to the bending of inclined beams [4]. The deformation of a honeycomb unit cell under uniaxial loading in each direction is shown in figure 2.16. Similarly, the deformation of a unit cell under shear loading is shown in figure 2.17.

The work of Gibson on studying the mechanics of the honeycomb structure can be summarized through

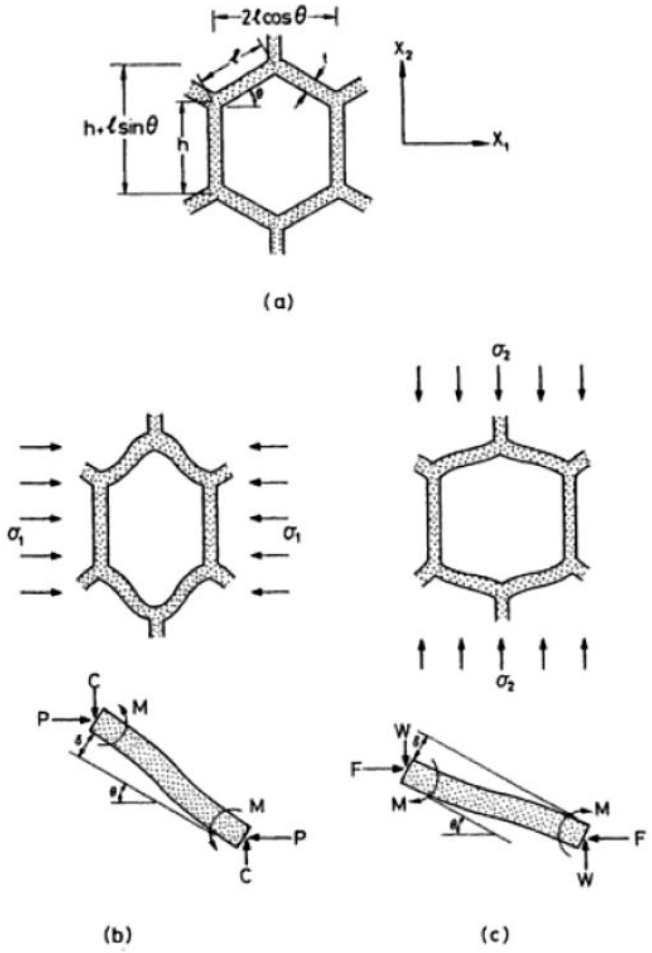

Figure 2.16: Deformation of honeycomb unit cell under uniaxial loading (a) undeformed unit cell (b) and (c) bending caused by uniaxial loads in X_1 and X_2 directions [5]

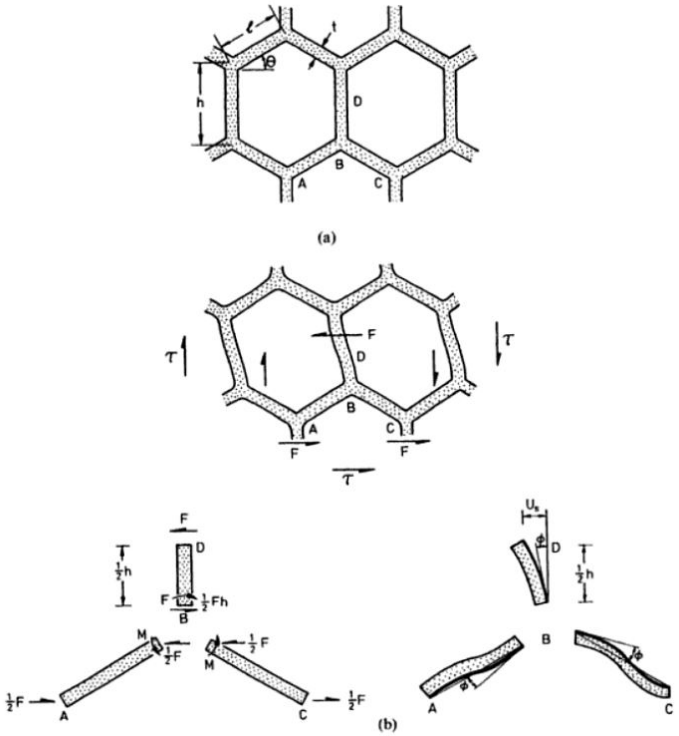

Figure 2.17: Deformation of honeycomb unit cell under shear loading (a) undeformed unit cell (b) load, moment, displacement and rotation caused by shear stress [5]

following expressions for relative density, Poisson's ratio, Young's modulus and shear modulus.

Relative Density:

$$\frac{\rho^{\star}}{\rho} = \frac{t(h/l+2)}{l(2cos\theta(h/l+sin\theta))} \tag{2.21}$$

Loading in X1 direction:

$$\nu_1 = \frac{cos^2\theta}{(h/l+sin\theta)sin\theta} \tag{2.22}$$

$$E_1 = E_s\Big(\frac{t}{l}\Big)^3 \frac{cos\theta}{(h/l+sin\theta)sin^2\theta} \tag{2.23}$$

Loading in X2 direction:

$$\nu_2 = \frac{(h/l+sin\theta)sin\theta}{cos^2\theta} \tag{2.24}$$

$$E_2 = E_s\Big(\frac{t}{l}\Big)^3 \frac{(h/l+sin\theta)}{cos^3\theta} \tag{2.25}$$

Shear Loading:

$$G_{21} = E_s\Big(\frac{t}{l}\Big)^3 \frac{(h/l+sin\theta)}{(h/l)^2(2h/l+1)cos\theta} \tag{2.26}$$

where meaning of h, l, t, θ used in above expressions are length of vertical ribs, length of inclined ribs, thickness of ribs, and angle between the inclined and horizontal ribs respectively. These symbols are also clearly indicated in figure 2.16. Similarly, E_s and ρ are Young's modulus, and density of the cell wall material. While deriving the above relations, assumptions were made regarding small strains, constant strain rate, and negligible shear and axial deformation of the members [4]. Relations including axial and shear deformations were also given which will be used later on during the computational analysis of honeycomb micro structure in Section 5.

Observing the expressions in equation 2.21 - 2.26, a two-dimensional cellular structure is anisotropic in nature. Four constants (E_1, E_2, G and one Poisson's ratio) are to be determined because E_1, E_2, ν_1, ν_2 are

related to each other by: $E_1\nu_2 = E_2\nu_1$. Looking at the expressions for Poisson's ratios ν_1 and ν_2, it can be easily noticed that the auxetic effect can be achieved in a hexagonal honeycomb structure by having a negative angle ($\theta < 0$) between vertical and inclined ribs. Also, since the mechanical properties are dependent on base material properties, the cell shape and thickness, a structure of desired Young's modulus, shear modulus and Poisson's ratio can be easily designed by modifying the dependent parameters.

Since the realization of the possibility of attaining a negative Poisson's ratio in a honeycomb structure, various studies have been performed to understand and improve their analytical formulas. Masters et al. [13] modified the analytical formula proposed by Gibson to combine stretching, shearing and hinging deformation in addition to the flexure of ribs. According to Master et al.'s model, the bond angle between the ribs could change under the application of external load. This study led to the possibility of having an auxetic honeycomb structure which is nearly isotropic in contrast to the highly anisotropic characteristics exhibited by the auxetic honeycomb deforming only by the bending of beams [13].

Lu et al. [12] modified the hexagonal re-entrant honeycomb structures with the addition of a narrow rib in the existing model. An analytical formula was proposed, and it was verified computationally with finite element simulations. The results showed that the addition of the narrow rib leads to the increase in the in-plane Young's modulus of the re-entrant auxetic structure compared to the one without the narrow rib.

Rad et al. [19] adapted a two-dimensional re-entrant structure to a three-dimensional re-entrant structure. An analytical solution was proposed to the three-dimensional structure based on the energy method of solid mechanics. Rad et al. also presented a finite element model approach to the modeling of 3D structure, and verified the analytical approach to the model. Huang et al. [8] presented a new design of the re-entrant honeycomb structure with two parts (a re-entrant honeycomb part and a thin plate part). The effect of the addition of a thin plate part was observed in the out-of-plane flexibility.

Phani et al. [15] studied the in-plane wave propagation in a two-dimensional periodic lattice. Four different lattice structures: hexagonal honeycomb, triangular honeycomb, square honeycomb and Kagomé lattice were considered during the study. The effect of relative density of the structure on the band gap exhibited by the structure was highlighted. The band gaps exhibited by the structure was investigated using the Floquet-Bloch theorem employed in a finite element model. Gonella et al. [6] also examined the plane wave propagation in conventional and re-entrant honeycombs using Bloch's theorem. Gonella et al.'s research was mainly focused in the determination of phase and group velocities using the dispersion relations. Hönig and Stornge analyzed the in-plane dynamic crushing of honeycomb in uniaxial stress and uniaxial strain boundary conditions [7]. The elastic wave speed in uniaxial stress boundary condition was found to agree with the continuum approach of predicting the wave speed using $\sqrt{E^\star/\rho^\star}$, where $E^\star$ and $\rho^\star$ are the effective elastic modulus and effective density of the honeycomb structure [7, 18].

Yang et al. [26] investigated the effectiveness of auxetic structures when subjected to impact loading. Experimental results of the prototypes of auxetic structure built using 3D printing technique were compared with the computational analysis results. The results highlighted the potential of auxetic structures in dissipating the shock energy away from the point of impact, making them preferable to use in protective devices [26]. Qi et al. [27] examined the deformation modes and shock energy mitigation feature of a re-entrant auxetic structure in LS-DYNA. The results indicated the good shock energy absorption capability of auxetic structures.

2.6. COMPUTATIONAL MODELLING OF AUXETIC STRUCTURES

The computational modelling of auxetic structures is a novel topic in the field of computational mechanics. It is still not possible to input a negative value of Poisson's ratio in many commercial finite element software packages when analyzing a linear elastic isotropic continuum. Therefore, the investigation of auxeticity in a continuum is carried out by either modifying the existing library and functions of the commercial finite element software packages or by using a self programmed finite element packages. Studies to investigate the effect of auxeticity in dynamic analysis of a continuum are even more limited. The computational estimation of different wave velocities in auxetic continuum solids was found to be missing during literature studies.

The computational approach for examining auxetic structures such as re-entrant structures, chiral structures etc. is mainly dominated by the unit cell analysis and homogenization techniques. The unit cell method is the most used computational approach to study the mechanics of auxetic structures [16]. The trend of the research in auxetic structures is: first the analytical formulas are proposed based on a unit cell to understand the mechanics and behavior of auxetic structures. Then, the unit cell is modelled computationally, and the numerical and analytical results are compared with each other. The results of the unit cell method are then

used as a basis to model and predict the behavior of the larger scale auxetic structures with the periodic boundary conditions.

The research on dynamic analysis of auxetic structures was also found to be very limited. Although a lot of studies are focused on investigating the dispersion relation and constant phase surface of auxetic structures, the studies were found to be less focused on the determination of wave velocities in auxetic structures.

This thesis aims to give a detailed overview of the computational modelling of auxetic structures. The procedure of the simplification of the physical model to a mechanical model, the description of the finite element type, selection of mesh size, enforcement of the boundary and loading conditions etc. are covered in detail. Different loading conditions (uniaxial, shear and bending) are considered in static and dynamic analyses of both continuum and re-entrant honeycomb structure. It has been aimed to relate the responses of the continuum and cellular structure model with each other. The behavior of these two different models in various loading conditions are compared with each other. This type of direct comparison was found to be missing in previous studies.

It has already been evident from expressions presented in Section 2.5 that the response of re-entrant honeycomb structures is significantly affected by specially two geometrical parameters: re-entrant angle θ and the aspect ratio h/l. The effect of these parameters on the response of a unit cell and the assembly of unit cells is investigated through numerical analyses. A self-programmed meshing technique was adopted to vary these parameters and reduce the time for modelling different structures.

In addition, the effect of the geometrical parameters of the honeycomb structure on the estimation of the wave speed in auxetic structure is also treated in detail in the thesis. The variation of wave speed with the geometrical parameters in honeycomb is predicted using both numerical analyses and the continuum approach. Along with that, the most highlighted topic in the dynamic study of honeycomb structure: identification of frequency bands, dispersion relation and constant phase surface of honeycomb lattice structure is also covered in the thesis. The results obtained from the dispersion relation study are related to the prediction of the wave velocities using the numerical and continuum approach. Thus, it helps to connect all different approaches available in the previous studies and provide comprehensive comparative study results.

In the previous studies [6, 10, 15], the examination of the frequency band exhibited by the honeycomb lattice was found to be limited only to the irreducible edge of the first Brillouin zone. This method of identifying the band gaps significantly reduces the computation effort. However, the expressions and relations defining the position of the irreducible edge was only available for the regular honeycomb unit cell. In this thesis, the expressions are derived for representing the position of the irreducible first Brillouin zone corners of any arbitrary honeycomb unit cell.

To summarize, the thesis aims to provide a detailed overview in the computational modelling of auxetic structure to study the response under different loading scenarios. The thesis can be referred as a starting point for modelling and computational tool building purpose to understand the mechanics and behavior of auxetic structures. Throughout the entire process, the concept of the unit cell method and homogenization are used directly or indirectly.

3

AUXETIC BEHAVIOR IN A CONTINUUM - STATIC ANALYSIS

The possibility of having a material with a negative Poisson's ratio was already evident from the classical continuum mechanics point of view since the 1800s. In a homogeneous isotropic linear elastic material, where all elastic properties are determined by two moduli, the Poisson's ratio can be in the range between -1 to 0.5. Similarly, in an anisotropic material, the Poisson's ratio can be negative if the total strain energy is positive [16]. However, the possibility of having a negative Poisson's ratio was not investigated for quite a long time. An example of this shortcoming is that still many commercial Finite Element Analysis software do not allow the inclusion of a negative Poisson's ratio for the modelling of a linear elastic isotropic material.

The behavior of an auxetic material from a continuum mechanics perspective is investigated in this chapter. The computational simulation was performed using the Finite Element code programmed in MATLAB. The finite element code programmed by Wells [25] was modified during the thesis. The effect of having a negative Poisson's ratio in a linear elastic isotropic continuum under different loading and boundary conditions is investigated. The behavior of an auxetic bar subjected to uniaxial loading and shear loading is studied computationally. Next, the response of an auxetic beam under three-point bending loading condition is examined.

3.1. UNIAXIAL LOADING

In a linear elastic isotropic material, strain $\boldsymbol{\varepsilon}$ and stress $\boldsymbol{\sigma}$ are related to each other through the elastic stiffness relation:

$$\boldsymbol{\sigma} = \mathbf{D}\boldsymbol{\varepsilon} \tag{3.1}$$

where $\mathbf{D}$ is the elastic stiffness matrix and is given by:

$$\mathbf{D} = \frac{E}{(1+\nu)(1-2\nu)} \begin{bmatrix} 1-\nu & \nu & \nu & 0 & 0 & 0 \\ \nu & 1-\nu & \nu & 0 & 0 & 0 \\ \nu & \nu & 1-\nu & 0 & 0 & 0 \\ 0 & 0 & 0 & \frac{(1-2\nu)}{2} & 0 & 0 \\ 0 & 0 & 0 & 0 & \frac{(1-2\nu)}{2} & 0 \\ 0 & 0 & 0 & 0 & 0 & \frac{(1-2\nu)}{2} \end{bmatrix} \tag{3.2}$$

The elastic stiffness matrix depends on the Young's modulus E and the Poisson's ratio ν. For a given fixed value of Young's modulus E, the relation between stress $\boldsymbol{\sigma}$ and strain $\boldsymbol{\varepsilon}$ is now only affected by the Poisson's ratio ν. It can be observed in equation 3.2 that, if the Poisson's ratio ν lies between -1 and 0.5, the diagonal elements of the stiffness matrix remain positive. Thus the effect of auxeticity can be studied by simply substituting the negative value of Poisson's ratio in the stiffness matrix.

The stiffness matrix $\mathbf{D}$ is obtained by the inversion of elastic compliance matrix, $\mathbf{C}$ which relates strain $\boldsymbol{\varepsilon}$ and stress $\boldsymbol{\sigma}$ by:

$$\boldsymbol{\varepsilon} = \mathbf{C}\boldsymbol{\sigma} \tag{3.3}$$

For a linear elastic isotropic material, the compliance matrix **C** is given by:

$$\mathbf{C} = \frac{1}{E}\begin{bmatrix} 1 & -\nu & -\nu & 0 & 0 & 0 \\ -\nu & 1 & -\nu & 0 & 0 & 0 \\ -\nu & -\nu & 1 & 0 & 0 & 0 \\ 0 & 0 & 0 & 2(1+\nu) & 0 & 0 \\ 0 & 0 & 0 & 0 & 2(1+\nu) & 0 \\ 0 & 0 & 0 & 0 & 0 & 2(1+\nu) \end{bmatrix} \tag{3.4}$$

In an auxetic material, the Poisson's ratio ν is less than 0, meaning the non-zero off diagonal terms in the first three rows are positive. These off diagonal terms in the compliance matrix relates strain in a longitudinal direction to the stresses in lateral directions. Therefore, having positive values for the off-diagonal terms means that the stress in a longitudinal direction produces a similar effect in lateral directions as in the direction of application, thus giving the desired auxetic effect.

The effect of auxeticity is observed in a two-dimensional bar subjected to uniaxial loading in x-direction. The plane stress condition is used to imitate the uniaxial stress situation in a two-dimensional problem. This leads to the modification of the compliance matrix to:

$$\mathbf{C} = \frac{1}{E}\begin{bmatrix} 1 & -\nu & 0 \\ -\nu & 1 & 0 \\ 0 & 0 & 2(1+\nu) \end{bmatrix} \tag{3.5}$$

The stiffness matrix **D** for the plane stress situation given by the inversion of the compliance matrix **C**.

$$\mathbf{D} = \frac{E}{1-\nu^2}\begin{bmatrix} 1 & \nu & 0 \\ \nu & 1 & 0 \\ 0 & 0 & 1-\nu \end{bmatrix} \tag{3.6}$$

Box 3.1.1: Uniaxial Stress

A bar 1 m long, 0.1 m high and 0.05 m thick is pulled by 1 N force at one end and restrained at the other. The Young's modulus E is taken as 2000 Nm^{-2}, and Poisson's ratio ν is varied between -0.90, -0.45, 0 and 0.45.
The problem is modelled using four noded quadrilateral elements with four integration points. A mesh of size 0.0125 m x 0.0125 m is used for the analysis. The right edge of the bar is loaded in x-direction with a uniformly distributed load equal to 1 N / 0.1 m = 10 Nm^{-1}. The displacement in x-direction is restrained at all nodes in the left edge, and the displacement in y-direction is restrained at the midpoint of the left edge to avoid rigid body translation.
As the bar is subjected to uniaxial tensile load, stress in the lateral direction is equal to zero. However, for the non-zero value of the Poisson's ratio, the deformation is obtained in the lateral direction as well. In the prescribed loading condition, the bar is at a constant strain, constant stress state. The stress at any point in the bar is equal to 'P/A' where P is the applied load i.e. 1 N and A is the cross-sectional area equal to 0.1 m x 0.05 m = 0.005 m^2. According to equation 3.3 and equation 3.5, strain in the direction of loading is equal to 1/E times the stress, which is also constant for all cases in the given situation. However, strain in the lateral direction is equal to -ν times the strain in the longitudinal direction, implying its absolute value is proportional to the absolute value of Poisson's ratio.
The analysis is performed for four different values of Poisson's ratio [0.45, 0, -0.45, -0.90]. Displacement, strain and stress are obtained as the output of the analysis and are compared with the theoretical predictions to observe the effect of varying Poisson's ratio in auxetic and non-auxetic range.

Case I ($\nu = 0.45$):
The *case I* corresponds to a conventional material with a positive Poisson's ratio. The bar is supposed to be longer in the direction of tensile loading and shorten in the lateral direction. The deformed model of the bar is shown in figure 3.1(a). The deformed model is represented by solid blue line whereas, the black dashed line represents the undeformed model. The bar is at a constant stress state of 200 Nm^{-2} in the longitudinal

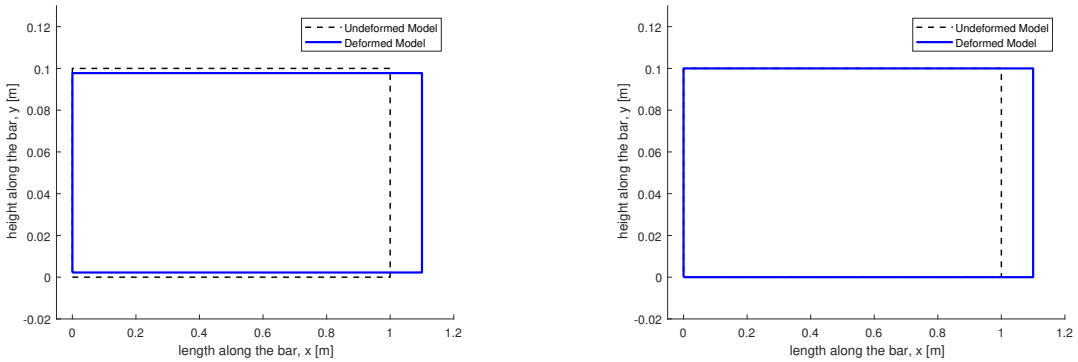

(a) Poisson's ratio $\nu = 0.45$

(b) Poisson's ratio $\nu = 0$

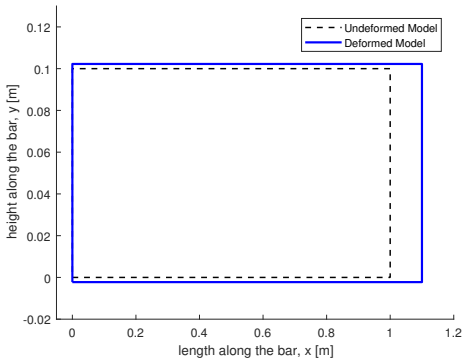

(c) Poisson's ratio $\nu = -0.45$

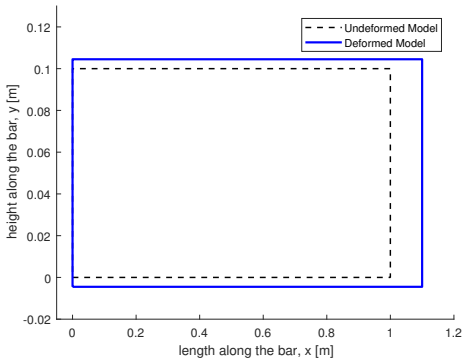

(d) Poisson's ratio $\nu = -0.90$

Figure 3.1: Deformed model at different values of Poisson's ratio

direction. Similarly, constant strain in the longitudinal and lateral directions are equal to 0.1 and -0.045 respectively.

Case II ($\nu = 0$):
The *case II* corresponds to a material with zero Poisson's ratio. Since the material has a zero Poisson's ratio, the bar should only deform in the direction of loading and cause no deformation in the lateral direction. The deformed model of the bar is shown in figure 3.1(b). Stress and strain in the longitudinal direction are similar to case I, but the strain in lateral direction is equal to 0 implying the deformation is only in the direction of the loading.

Case III ($\nu = -0.45$):
The *case III* corresponds to an auxetic material with negative Poisson's ratio ($\nu = -0.45$). Unlike case I, now the bar not only elongates in the direction of loading but also in lateral direction. Also, the constant strain in lateral direction is now of similar sign as the constant strain in longitudinal direction. The strain in the lateral direction in Case III is equal to 0.045. The deformation in the lateral direction is equal in magnitude in Case I and Case III but opposite in sign. The deformed model of the bar is shown in figure 3.1(c).

Case IV ($\nu = -0.90$):
The *case IV* also corresponds to an auxetic material with negative Poisson's ratio ($\nu = -0.90$). Like case III, the bar is stretched in the lateral direction as well. As the Poisson's ratio is the largest in case IV compared to all other cases, the deformation in lateral direction is also found to be the largest in Case IV. The constant strain in the lateral direction in present case is equal to 0.090 which means it approaches towards the constant strain in longitudinal direction as Poisson's ratio ν is equal to -0.90. The deformed model of bar is shown in figure 3.1(d).

The results presented in all four cases discussed above indicated that the deformation in a lateral direc-

tion is affected by the Poisson's ratio. Changing the sign of the Poisson's ratio also changes the direction of deformation in lateral direction. This computational study highlights the possibility of achieving an auxetic effect in a linear elastic isotropic material simply by using a negative value of the Poisson's ratio in the material stiffness matrix.

3.2. SHEAR LOADING

The shear modulus G in an isotropic linear elastic material is related to Young's modulus E and Poisson's ratio ν through $G = \frac{E}{2(1+\nu)}$. It means that for a given value of Young's modulus E, the shear modulus of the material is inversely proportional to the Poisson's ratio ν. The ratio of shear modulus (G) and Young's modulus (E) is given by: $\frac{1}{2(1+\nu)}$. The variation of this ratio in the range of valid Poisson's ratios in an isotropic material [-1, 0.5] is shown in figure 3.2.

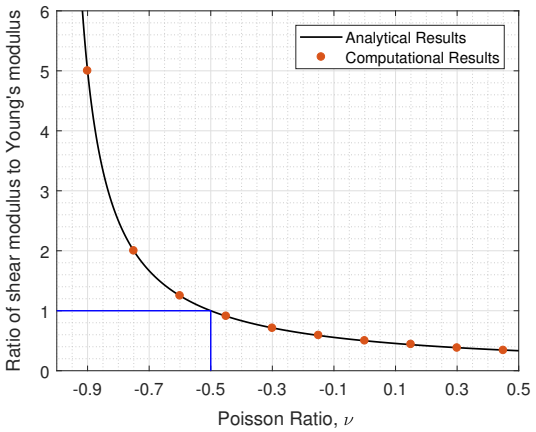

Figure 3.2: Ratio of Shear modulus to Young's Modulus in an isotropic material

It can be observed in figure 3.2 that the shear modulus in a material increases with the decrease in Poisson's ratio. The shear modulus which is one-third of the Young's modulus when the Poisson's ratio is equal to 0.5 approaches to infinity at the other extreme value of Poisson's ratio (ν = -0.90). The shear modulus already surpasses the value of Young's modulus when Poisson's ratio is equal to -0.5. The ratio indicates that the material is more resistant to shearing with the increase in auxeticity. The analytical ratio presented in figure 3.2 is checked computationally by modelling a shear problem.

Box 3.2.1: Shear Loading

The bar described in Box 3.1.1 is used for the shear loading problem as well. The dimensions and Young's modulus are kept constant, whereas the Poisson's ratio is varied between -0.90, -0.75, -0.60, -0.45, -0.30, -0.15, 0, 0.15, 0.30 and 0.45.
Same element type, integration points and mesh size as described in Box 3.1.1 are used. As shearing of the bar is modelled, all nodes are restrained in the x-direction. All nodes in the left edge of the bar are also restrained in the y-direction. The right edge of the bar is loaded in y direction. 0.02 m displacement is applied to all nodes in the right edge in y-direction. The figure of the deformed model is shown in figure 3.3.
The analysis is performed for different values of Poisson's ratio listed above. As an output, the shear stress (τ_{xy}) in the loaded nodes are obtained and divided by the imposed shear strain (γ_{xy} =u_y/l_x) to calculate the computational result of shear modulus of the material. Finally, the ratio of the computational result of shear modulus to input Young's modulus is plotted against the respective values of Poisson's ratio, and results are compared with the analytical prediction.

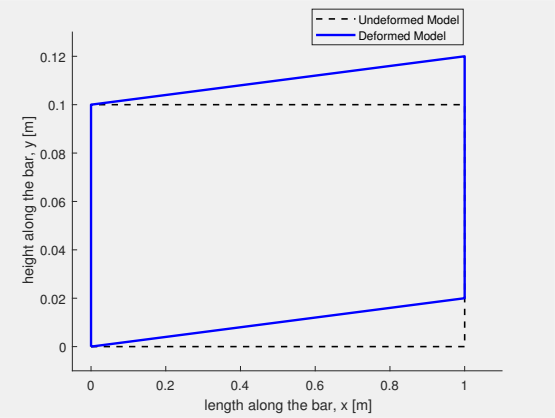

Figure 3.3: Deformed model under shear loading

The ratio of shear modulus to Young's modulus for the Poisson's ratio varying between [-0.90, -0.75, -0.60, -0.45, -0.30, -0.15, 0, 0.15, 0.30, 0.45] was found to be [5.00, 2.00, 1.25, 0.91, 0.71, 0.59, 0.50, 0.44, 0.38, 0.34] respectively. The computational results are exactly as predicted by the analytical formula:

$$G = \frac{E}{2(1+\nu)} \tag{3.7}$$

The same shear strain was imposed in all analyses for a varying Poisson's ratio. The increase in shear modulus with a decreasing value of Poisson's ratio indicates that more shear stress is required to obtain the same shear strain in an auxetic material as compared to the conventional material. The material becomes more shear resistant and therefore, tends to resist the change in its shape.

3.3. THREE POINT BENDING

The Poisson's ratio not only affects the uniaxial and shear loading, but also the behavior in other loading conditions. The effect of auxeticity in the bending of a beam is investigated next. The effect of auxeticity in the bending problem is not as straight forward as in the uniaxial and shear loading.

A beam of length $l_\circ$, height h and out of plane thickness t is considered. The beam is supported at equal distance from the left and right edges such that the span between the supports is equal to l. Then, the beam is loaded by force P at the mid-span of the beam thus representing the three-point bending problem. The deflection of the mid-span is known to consist of a combination of bending deflection (w_b) and shear deflection (w_s). The deflection of mid-span of the beam (w) is given by:

$$w = w_b + w_s \tag{3.8a}$$

$$w = \frac{Pl^3}{48EI} + \frac{Pl}{4GA_s} \tag{3.8b}$$

$$w = \frac{P}{4Et\left(\frac{h}{l}\right)^3} + \frac{0.3P}{Gt\frac{h}{l}} \tag{3.8c}$$

It can be noticed in equation 3.8 that for a beam with given geometrical dimensions and Young's modulus E, the deflection depends only on shear modulus G which depends on the value of the Poisson's ratio as already discussed in the previous section. This means that with the increase in auxeticity, the shear modulus G increases and thus leads to lesser deflection. However, the effect of Shear modulus is only present in the contribution of shear deflection (w_s), thus the effect of auxeticity is dependent on the proportion of shear deflection contribution to the total deflection of the beam.

The deflection of the beam is also very much dependent on the slenderness ratio (l/h). When the slenderness is decreased (i.e. height of beam is increased for constant span l), the total deflection of the beam decreases as well. A point to note in this observation is the change in the proportion of shear and bending deflection contribution. With the decrease in slenderness, the deflection due to bending decreases more as it is inversely proportional to $\left(\frac{h}{l}\right)^3$ in comparison to the deflection due to shear which is inversely proportional

to $\frac{h}{l}$. Thus, the proportion of the deflection due to shear in total deflection of the beam increases with the decrease in the slenderness.

Now, combining the effect of auxeticity and slenderness, it can be predicted that the effect of auxeticity is more pronounced in high beams as compared to slender beams. This prediction is examined computationally by observing the effect of varying the slenderness ratio and Poisson's ratio in the deflection of the mid-span of the beam.

Box 3.3.1: Three Point Bending

A beam with following geometrical dimension is taken into account:

$$\text{length}, l_{\circ} = 1.2 \text{ m}$$
$$\text{span}, l = 1.0 \text{ m}$$
$$\text{height}, h = variable$$
$$\text{thickness}, t = 0.05 \text{ m}$$

The height is varied between [0.2, 0.3, 0.5, 1]. The Young's modulus E is taken to be 200000 Nm^{-2}, and the Poisson's ratio is varied between -0.95 to 0.45. The beam is loaded at the mid-span on the top edge with 1 N concentrated force. The vertical displacement is restrained at two points on the bottom edge, 0.1 m from both right and left edges. In addition, the horizontal displacement is also restrained at 0.1 m from the left edge to avoid rigid body translation in x direction.
The beam is modelled using six noded triangular element with six integration points and a mesh size of 0.1 m x 0.1 m. Since the plane stress situation is used, the material stiffness matrix given in equation 3.6 is used in this problem as well. The figure of the deformed model for a beam with height $h = 0.5$ m and Poisson's ratio $\nu = -0.90$ is shown in figure 3.4.

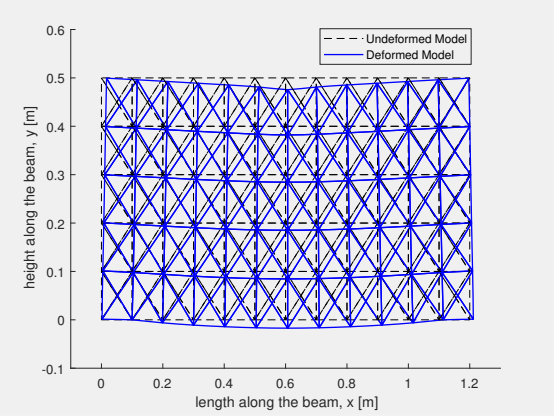

Figure 3.4: Deformed model in three point bending when Poisson's ratio $\nu = -0.90$ and slenderness $l/h = 2$, scale: 50

The deflection at the point of application of point load is subjected to local effects in addition to the beam deflection. Therefore, the deflection at mid-span on the bottom edge is considered to investigate the effect of auxeticity and slenderness. The deflection at mid-span on the bottom edge for each analysis is collected. Then, the deflection for each beam height is plotted separately against the Poisson's ratio.

The results of the analysis for different beam heights are presented in figure 3.5. As already discussed before, it can be observed that in each beam, the deflection of the beam decreases with the increase in auxetic effect. Also, for a given value of Poisson's ratio, the deflection of beam decreases with the decrease in slenderness. Making a closer observation on the proportion of decrease in deflection at varying slenderness and Poisson's ratio, the computational results were found to agree with the theoretical predictions. At the slenderness $l/h = 5.0$, the deflection of beam decreases by only 2.8852% when the Poisson's ratio was changed from 0.45 to -0.95. This difference in the deflection increases with the decrease in the slenderness. For the slenderness $l/h = 3.33, 2.0, 1.0$, the difference in the deflection was found to be 5.3542%, 14.0960% and 27.9598%

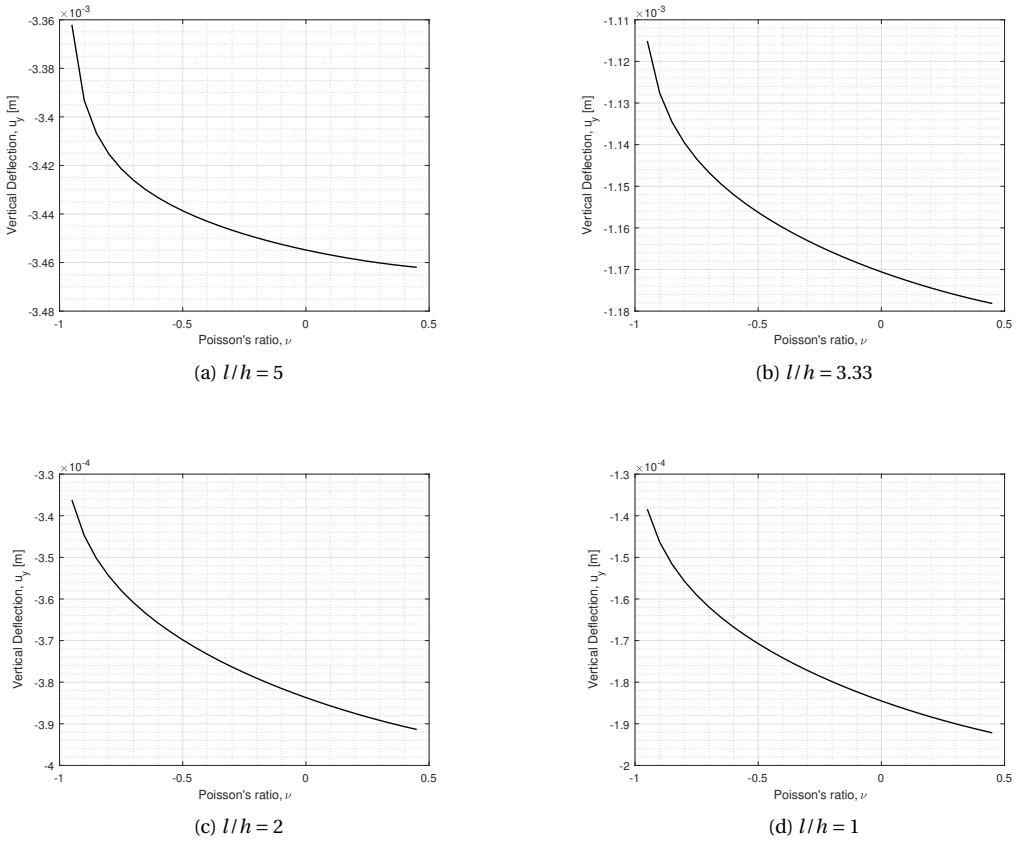

(a) $l/h = 5$ (b) $l/h = 3.33$

(c) $l/h = 2$ (d) $l/h = 1$

Figure 3.5: Variation of deflection of beam mid-span with Poisson's ratio at different values of slenderness

respectively for the same variation in the Poisson's ratio. The results show that auxetic beams deform to a smaller extent than the conventional beams, and the effect is more pronounced when the slenderness is low.

3.4. SUMMARY OF STATIC BEHAVIOR IN AN AUXETIC CONTINUUM

The aim of this chapter was to investigate the effect of auxeticity in a continuum subjected to various static loading conditions. The effect of uniaxial loading, shear loading and three point bending on an auxetic continuum was examined through computational analysis. The computational results were compared with the theoretical predictions. The results of the uni-axial loading showed that the material with negative Poisson's ratio deforms in a similar manner in both the loading and lateral directions. An auxetic material subjected to tensile load elongates in both lateral and longitudinal directions. Similarly, the auxetic materials contract laterally and longitudinally when compressed. In a linear elastic isotropic material with constant Young's modulus, the shear modulus increases with the decrease in the value of Poisson's ratio. It means that an auxetic material is more resistant to shear compared to a conventional material. The shear modulus is between one-half and one-third of the elastic modulus in a conventional material. Whereas, in an auxetic material the shear modulus is always found to be higher than one-half of the elastic modulus. In fact, for a Poisson's ratio smaller than -0.5, the shear modulus is computed to be larger than the elastic modulus.

An auxetic beam subjected to bending deflects less compared to a conventional beam. The effect of auxeticity is more pronounced in a high beam. When the slenderness of the beam decreases, the significance of auxeticity is found to increase. The reason for this effect is due to the combined effect of higher shear resistance at negative Poisson's ratio and increase in the proportion of shear deflection contribution to the total beam deflection for low slenderness. The close comparison of the computational results and the theoretical predictions obtained in the static analyses of auxetic continuum has provided a basis for the use of the finite element code written for this thesis to analyze more complicated loading conditions in auxetic continuum.

4

AUXETIC BEHAVIOR IN A CONTINUUM - DYNAMIC ANALYSIS

The effect of having a negative Poisson's ratio on wave propagation was discussed in Section 2.4. The theory clearly shows that the speed of dilatation and shear wave is significantly affected by the negative Poisson's ratio. The theoretical predictions are checked computationally in this chapter. First, a bar is loaded uniaxially and then in shear to compute the dilatation and shear wave velocities. The results are compared with the theoretical predictions. Next, the beam impact problem is also investigated. The possible use of an auxetic structure in impact mitigation application makes it an interesting case to examine the beam's response to impact loading. An overview of the response of auxetic orthotropic materials under static and dynamic loading conditions is presented in Section 4.3, and at the end, results are summarized, discussed and concluded in Section 4.4.

The analysis is carried out using the Finite Element Code programmed in MATLAB. The FEM code programmed by Wells [25] for static analysis was modified for the dynamic analysis. Both explicit and Newmark implicit time scheme methods were programmed. The accuracy of the programmed section was verified by different numerical approaches, such as: stability issues in explicit method, time step sensitivity etc., and by comparing few cases with existing commercial Finite Element Software such as DIANA and STRAND7. Results of these verification and comparison are presented in Appendix A.

4.1. ONE DIMENSIONAL MOTION

The propagation of a plane wave of dilatation and a plane wave of distortion represents a one-dimensional motion in a two-dimensional bar. The effect of auxeticity on the speed of a dilatational wave and a distortion wave is examined computationally in this section.

4.1.1. DILATATION WAVE PROBLEM

First, the influence of auxeticity on the speed of a plane wave of dilatation in a two-dimensional bar was studied. During the propagation of a plane wave of dilatation, the structure is in a uniaxial strain condition, i.e. strains in two lateral directions are equal to zero. To model the necessary condition for plane wave of dilatation in a two-dimensional structure, the material stiffness matrix for the plane-strain situation was implemented, which is given by:

$$\mathbf{D} = \frac{E}{(1+\nu)(1-2\nu)} \begin{bmatrix} 1-\nu & \nu & 0 \\ \nu & 1-\nu & 0 \\ 0 & 0 & \frac{(1-2\nu)}{2} \end{bmatrix} \tag{4.1}$$

Box 4.1.1: Plane Wave of Dilatation

A bar 1 m long, 0.1 m high and unit thickness is subjected to a dynamic load on one end and restrained at the other end. The Young's modulus and density of the material is taken to be 2000 Nm^{-2} and 1 kgm^{-3} respectively. The Poisson's ratio ν is varied between [-0.90, -0.75, -0.60, -0.45, -0.30, -0.15, 0,

0.15, 0.30, 0.45]. The effect of varying Poisson's ratio and specially the effect in auxetic range can then be investigated.
The bar is modelled using four noded quadrilateral elements with four integration points. A consistent mass matrix is used in the finite element analysis. To represent a uniaxial strain situation, all nodes/points in the bar are restrained in the y-direction. A pulse force is applied at the loaded edge of the bar. The characteristics of the loading pulse force is shown in figure 4.1

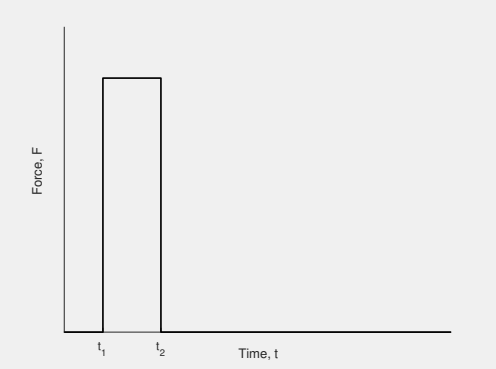

Figure 4.1: Time dependency of the input loading force

The applied force causes deformation in the direction of loading which propagates towards the other end of the bar. The reflection process at the fixed end and the loaded end, and the speed of the propagating wave are examined. The mesh and the time step size are selected after a mesh and time step sensitivity analysis. Since the displacement in lateral direction is restrained and wave is only propagating along the length, mesh size in lateral direction is taken to be 0.1 m i.e. one element along the height. Analyses are performed for 8 different mesh sizes. The bar is divided into 20, 40, 80, 160, 320, 640, 1280 and 2560 elements along the length of the bar to select an appropriate mesh size. The mesh sensitivity analyses are performed using the time step size $\Delta t = 5.e-5$ s. After selecting the suitable mesh size, the time step sensitivity analyses are performed using eight different time step sizes.

MESH SENSITIVITY

The bar described in Box 4.1.1 is subjected to a load varying with respect to time. Directly applying the rectangular load pulse as shown in figure 4.1 was found to give highly mesh dependent results. Therefore, the bar was subjected to a load which has a rise time of 10 Δt to reach the value 1 N, then constant load of 1 N until 20 Δt and finally decreasing to 0 N with a fall time of 10 Δt, where $\Delta t = 5.e-5$ s. The Poisson's ratio is taken as 0.15 for the mesh and time step sensitivity analyses. The analyses are performed for 50 time steps, and the displacement of the right end of the bottom edge is observed at the final time step for each mesh size. The result of the mesh sensitivity analysis is shown in figure 4.2(a). It can be observed in figure 4.2(a) that results are not very accurate when using a mesh size of 0.05 m (i.e. 20 elements along the length of the bar), whereas results converge for a mesh size smaller than 0.0125 m (80 elements along the bar length). Thus 0.0125 m mesh size is adopted for the analysis.

TIME STEP SENSITIVITY

After the mesh size sensitivity analysis, the time step sensitivity analysis is also performed. The bar modelled for the mesh sensitivity study was used again. The mesh size used for the analysis was 0.0125 m. The analyses are performed for 8 different time step sizes. The bar was subjected to similar loading situation as described in mesh sensitivity analysis. The loading steps were adjusted accordingly to have same total load and loading behavior. The result of the time step sensitivity study is shown in figure 4.2(b). The result presented in figure 4.2(b) indicates that the difference using time step size of 2.5 x 10^{-5} s and 1.25 x 10^{-5} s was found to be only 0.06 %, but the computation time increases by 100 %. Therefore, considering the magnitude of relative difference and computational effort, 2.5 x 10^{-5} s was chosen as the time step size for dynamic analysis.

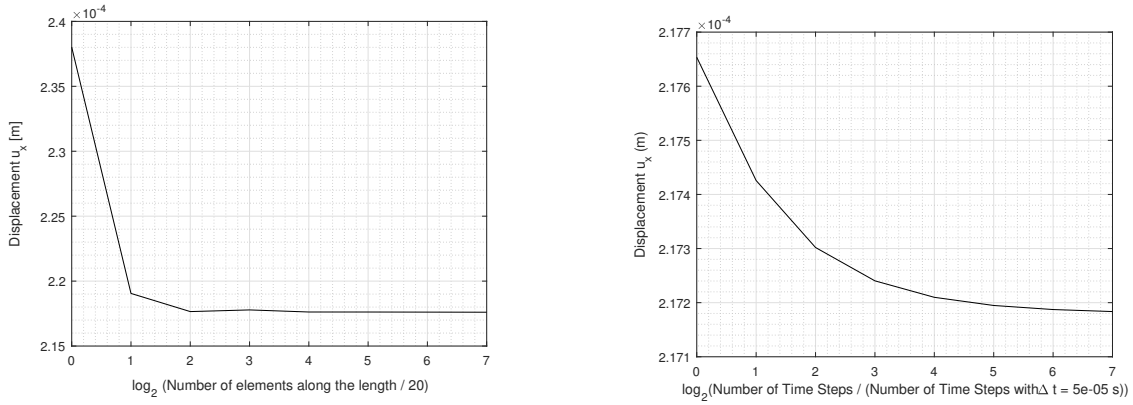

(a) Mesh size convergence study

(b) Time Step convergence study

Figure 4.2: Mesh size and Time step sensitivity results

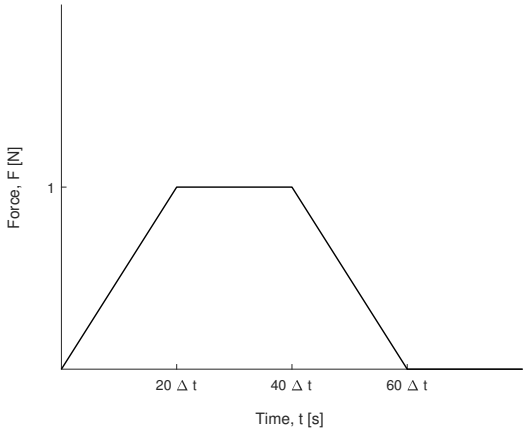

Figure 4.3: Force - time profile

DILATATION WAVE VELOCITY

The bar described in box 4.1.1 is then used to study the plane wave dilatation problem after selecting the appropriate mesh size and time step size. The bar is loaded with the load-time profile shown in figure 4.3. Ten different analyses are performed to calculate the wave velocity at different Poisson's ratios listed in box 4.1.1. The stages of wave propagating through the length of the bar for the Poisson's ratio $\nu = -0.90$ are shown in figure 4.4. The plane wave of dilatation generated by the application of load in the beginning of an analysis propagates along the length of the beam until it reaches the fixed end. At fixed end, the wave reflects and start propagating towards the free end. After reaching the free end, the wave flips and again start propagating towards the fixed end. The process is repeated continuously. This process of wave propagation can be easily understood and explained from the theory and by using the wave image technique as well.

The velocity of the wave is measured by dividing two times the length of the bar with the time taken for the wave to return to the free/loading end. The results of wave speed measured for various Poisson's ratio is plotted in figure 4.5 together with the analytical results. It can be observed in figure 4.5 that the wave velocity increases with the increase in the absolute value of the Poisson's ratio. The relative difference between computational and analytical results in the estimation of dilatation wave velocity was found to be 1.5 %.

The dilation wave velocity decreases with the decrease in Poisson's ratio in the positive range. The minimum wave velocity is obtained when the Poisson's ratio is equal to 0, and then the wave velocity increases again in the negative range of Poisson's ratio. The dilatation wave velocity continues to increase in the negative range, and it even exceeds the wave velocity obtained using the positive value of the Poisson's ratio. The dilatation wave velocity at zero Poisson's ratio is equal to the longitudinal wave velocity. At zero Poisson's ratio, the uniaxial stress situation and uniaxial strain situation are similar since the lateral direction effect of the deformation/loading is not present.

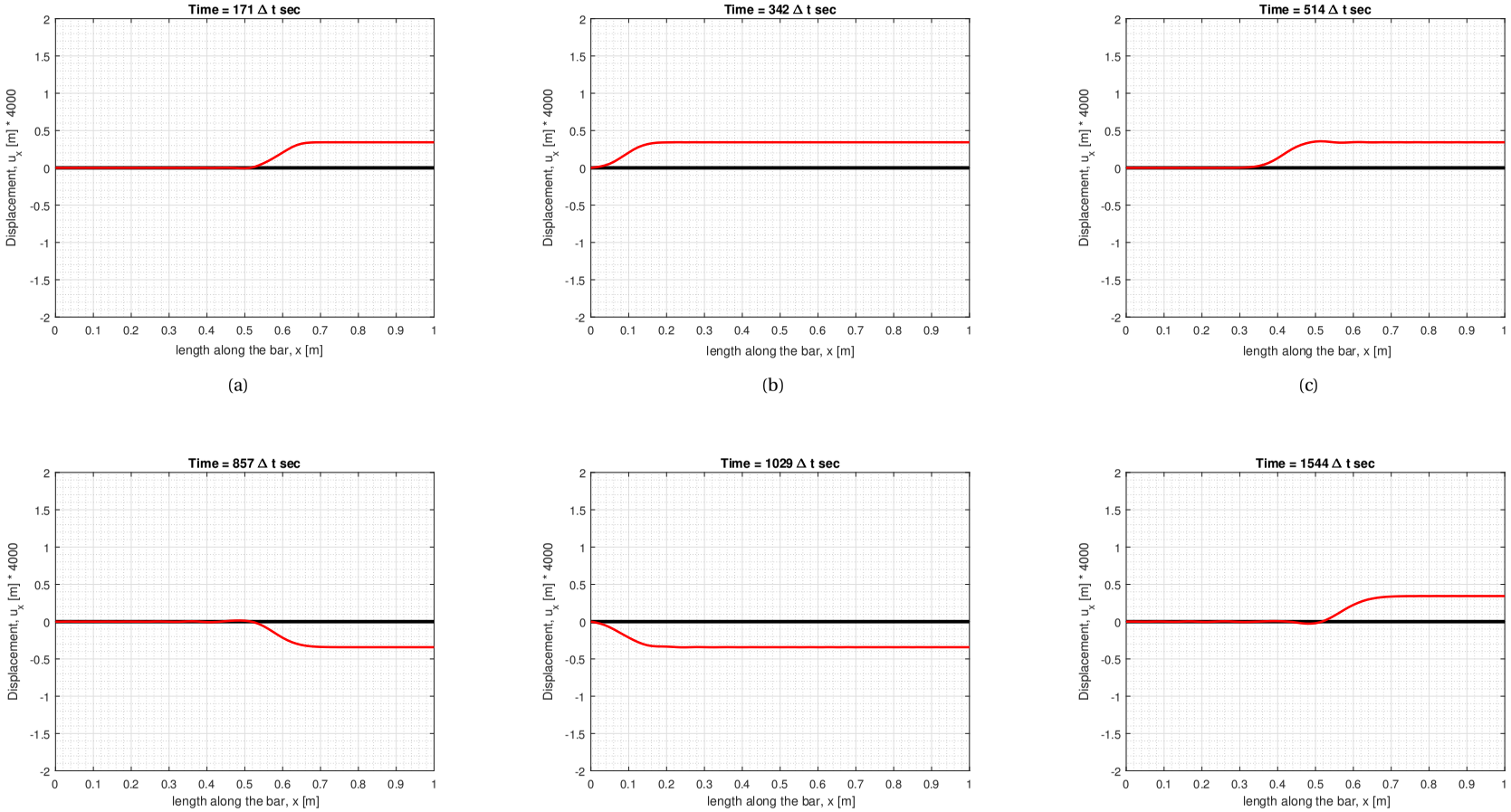

(a) (b) (c)

(d) (e) (f)

Figure 4.4: Dilatation wave propagating through the length of the bar at various time steps

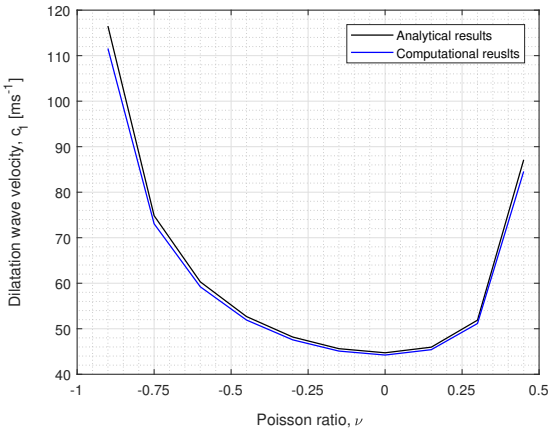

Figure 4.5: Variation of dilation wave velocity with respect to Poisson's ratio

4.1.2. SHEAR WAVE PROBLEM

After observing the effect of negative Poisson's ratio in dilatation wave velocity, shear wave velocity in an auxetic material is examined next. The shear wave velocity is dependent on the shear modulus of a material which varies with the Poisson's ratio for a given value of Young's modulus as shown in figure 3.2.

Box 4.1.2: Shear Wave

The bar described in box 4.1.1 is used for the shear wave problem as well. The mesh size and time step size selected after performing sensitivity analyses are used for the shear wave problem as well.

$$\Delta x = 0.0125 \text{ m}$$
$$\Delta t = 2.5e-5 \text{ s}$$

The right end of the bar is subjected to the vertical load, whereas the left edge is restrained in both x and y directions. In addition, all nodes in the bar are restrained in the horizontal direction. The motion is allowed only in the vertical direction to imitate the shear behavior. The bar is subjected to a similar load profile as shown in figure 4.3. The analyses are performed for different values of Poisson's ratio varying between [-0.90 -0.75 -0.60 -0.45 -0.30 -0.15 0 0.15 0.30 0.45]. The deformed model during the propagation of the shear wave along the length of the bar with Poisson's ratio $\nu = -0.90$ is shown in figure 4.6

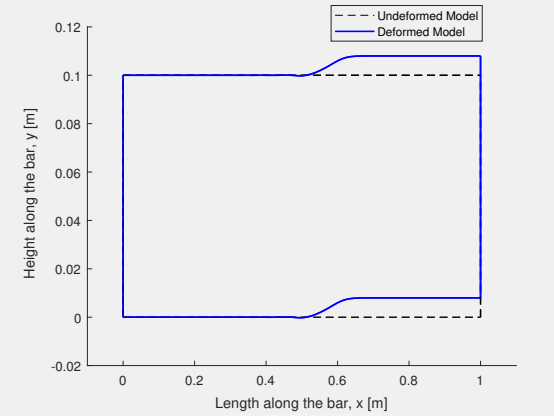

Figure 4.6: Deformed model during the shear wave propagation, Scale: 800

The shear wave propagating along the length of the bar was examined for different values of Poisson's ratio listed in box 4.1.2. The reflection phenomenon at the fixed and free end were observed and verified as done for the dilatation wave. The wave velocity was obtained by dividing two times the length of the bar with

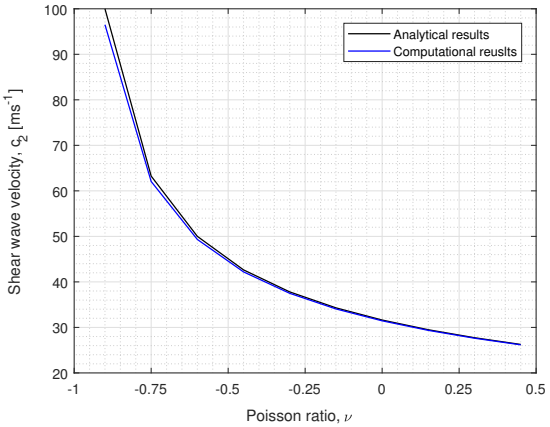

Figure 4.7: Variation of shear wave velocity with respect to Poisson's ratio

the time taken for the shear wave to return to the free/loading end. The computational results of the shear wave velocity are shown in figure 4.7 together with the analytical results. The relative difference between computational and analytical results was found to be less than 1%.

The shear wave velocity continues to increase with the decrease in the Poisson's ratio. The shear wave velocity at -0.90 Poisson's ratio is more than 3 times the shear wave velocity at minimum Poisson's ratio in a non-auxetic range i.e. $\nu = 0$. The shear wave velocity which is smaller than the longitudinal wave velocity $\left(\sqrt{\frac{E}{\rho}}\right)$ in a material with the conventional values of Poisson's ratio is found to be larger than the longitudinal wave velocity when the Poisson's ratio is less than -0.5. The shear wave velocity at -0.5 Poisson's ratio is equal to the longitudinal wave velocity and the dilatation wave velocity at 0 Poisson's ratio.

Although the shear wave velocity is larger than the longitudinal wave velocity at Poisson's ratio less than -0.5, it never exceeds the dilatation wave velocity. As seen in figure 4.7, the shear wave velocity increases rapidly with the decrease in Poisson's ratio from positive extreme limit i.e. $\nu < 0.5$. Therefore, the ratio of the dilatation wave velocity to shear wave velocity continues to decrease too. The ratio decreases rapidly until the lower limit of the non-auxetic range i.e $0 < \nu < 0.5$. However, the rate of decrease in the ratio in the auxetic range diminishes, because, in the auxetic range, not only the shear wave velocity increases, but also the dilatation wave velocity increases. The ratio of dilatation wave velocity to shear wave velocity for varying Poisson's ratio is shown in figure 4.8. Both the computational and analytical results are presented, and the relative difference between them is found to be always smaller than 0.79%. This shows the consistency between the computational results and the theoretical predictions of one-dimensional wave motion in an auxetic continuum.

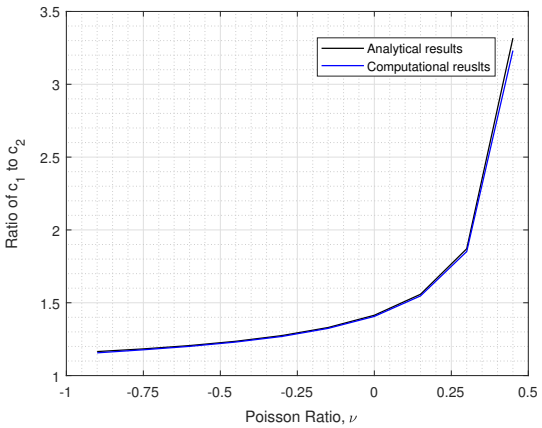

Figure 4.8: Variation of wave velocities ratio with respect to Poisson's ratio

4.2. TWO DIMENSIONAL MOTION

The computational results from the static analyses and a dynamic analysis of a one-dimensional motion in auxetic structures are in correspondence with the theory. This comparison has helped to validate the finite element code which will now be used to examine the effect of comparatively complicated loading condition in an auxetic structure. The effect of auxeticity on a two-dimensional wave propagation is studied through the computational analysis of a beam impact problem. A simply supported beam is subjected to an impact load at the beam mid-span. The characteristics of wave propagation, deformation behavior and their variation with respect to the auxetic effect is examined in this section.

4.2.1. COMPUTATIONAL CHALLENGES

Box 4.2.1: Beam Impact

A beam 1.2 m long, 0.5 m high and 0.05 m thick is subjected to a dynamic load at the beam mid-span. The load is spread over a length of 0.1 m on the mid-span i.e. the top edge of the beam is subjected to a dynamic load at 0.5 m to 0.7 m from the left end of the beam. At the bottom edge, the vertical displacements are restrained at 0.10 m to 0.15 m distance from each ends of the beam. In addition, a node at 0.10 m from the left end is also restrained in the horizontal direction to avoid the rigid body motion.
The Young's modulus E and a Poisson's ratio ν of the beam is taken to be 200000 Nm^{-2} and -0.45 respectively. The beam is modelled using six-noded triangular elements with six integration points and a mesh size of 0.0125 m x 0.0125 m. Since the plane stress situation is used, the material stiffness matrix given in equation 3.6 is used in this problem as well. The time step size used in the dynamic analysis is Δt = 5e-7 s. The beam is subjected to an external load between the 11th and the 30th time steps. The load has a rise time of ten time steps to 10 Nm^{-1}, stays constant for the next ten time steps and falls to 0 Nm^{-1} again in ten time steps.

The result of the computational analysis at the end of the 100th time step is shown in figure 4.9. The displacement shown in the figure are scaled with a factor equal to 1000. The figure only shows the deformation behavior at the top part of the beam around beam mid-span as it highlights the computational challenges faced during the dynamic analysis. The middle 0.1 m part of the top edge of the beam was subjected to uniform dynamic load. However, it can be observed in the figure that the loaded part of the beam is not displaced uniformly. The middle node of each loaded element was found to be displaced less compared to the end nodes.

It is preferable to use six noded triangular elements in a bending problem compared to four noded quadrilateral elements and eight noded quadrilateral elements due to the problem of shear locking and/or spurious modes which trigger due to the reduced integration. However, the spurious modes were found to appear in the dynamic analysis using six noded triangular elements as well. These spurious modes become more dominant with the increase in auxeticity. Besides, the results are also strongly dependent on the mesh size. This has shown that the results from the dynamic analysis of an unconstrained problem like the beam

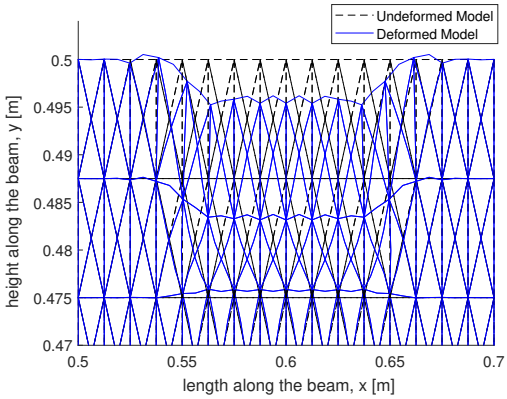

Figure 4.9: Deformation of the top part of the beam (Scale Factor : 1000)

impact discussed above suffer from problems of spurious modes and mesh dependency unlike the static analyses and dynamic analysis of a one-dimensional wave motion. Two different computational techniques, namely: Modal Analysis and the B-bar method were adopted to solve the encountered computational difficulties which are discussed in detail in next section.

4.2.2. ALTERNATIVE COMPUTATIONAL TECHNIQUES

MODAL ANALYSIS

In a dynamic analysis, the response of a structure can be decomposed into a number of deformation modes. The combination of all these modes represents the final deformation of the structure. Modal analysis involves decomposing the dynamic analysis to the computation of different deformation modes and finding a linear combination of them to obtain the resulting deformation. For an equation,

$$(\mathbf{K} - \omega_i^2 \mathbf{M})\Psi_i = \mathbf{0} \tag{4.2}$$

the eigenvectors $\Psi_\mathbf{i}$ and the positive square root of the eigenvalues ω_i are considered as the vibration modes and the natural frequencies respectively. The deformation vector $\mathbf{u}$ is then represented as a linear combination of the vibration modes.

$$\mathbf{u}(t) = \sum_i \alpha_i(t)\Psi_i \tag{4.3}$$

where, $\alpha_i(t)$ is an amplitude of the ith vibration mode. Using this relation and the orthogonal property of eigenmodes for linear problems Ψ_i, the equation of motion can be modified to:

$$m_i\ddot{\alpha}_i + k_i\dot{\alpha}_i = \Psi_i^T\mathbf{f} \tag{4.4}$$

where, m_i and k_i are the components of a modal mass matrix and a modal stiffness matrix respectively. The eigenvalue analysis of the stiffness matrix $\mathbf{K}$ revealed that there is no sufficient evidence to omit any modes in specific as all eigenvalues were greater than zero. As only the lower frequency modes are significant to the final deformation, few lower modes of the system are considered in the modal analysis. The problem described in box 4.2.1 was analyzed using modal analysis with first 200, 400, 800 and 1600 modes. The results of the sensitivity analyses indicated that the first 800 modes were sufficient to predict the response of the beam. The result of the modal analysis at the end of the 100th time step for the beam impact problem described before is shown in figure 4.10. It can be observed in the figure that the spurious deformation observed in figure 4.9 is suppressed to some extent after using the modal analysis. Next, the results obtained from the modal analysis is compared with the B-bar method.

B-BAR METHOD

The concept of the B-bar method is that the stiffness matrix is split into the volumetric and deviatoric parts. Instead of splitting the volume integral, first, the strain in an element is split into dilatational and deviatoric

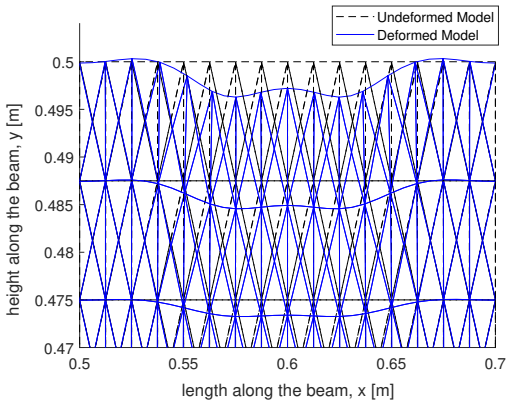

Figure 4.10: Deformation of the top part of the beam using the Modal Analysis (Scale Factor : 1000)

parts, and a new definition of strain is used in an element. Let $\mathbf{B}_{dil}$ and $\mathbf{B}_{dev}$ represent the dilatational and deviatoric parts of a $\mathbf{B}$ matrix i.e.

$$\mathbf{B} = \begin{bmatrix} B_1 & 0 & 0 \\ 0 & B_2 & 0 \\ 0 & 0 & B_3 \\ B_2 & B_1 & 0 \\ 0 & B_3 & B_2 \\ B_3 & 0 & B_1 \end{bmatrix}, \qquad \mathbf{B}_{dil} = \frac{1}{3}\begin{bmatrix} B_1 & B_2 & B_3 \\ B_1 & B_2 & B_3 \\ B_1 & B_2 & B_3 \\ 0 & 0 & 0 \\ 0 & 0 & 0 \\ 0 & 0 & 0 \end{bmatrix} \tag{4.5a}$$

$$\mathbf{B}_{dev} = \mathbf{B} - \mathbf{B}_{dil} \tag{4.5b}$$

Next, $\bar{\mathbf{B}}_{dil}$ is defined as:

$$\bar{\mathbf{B}}_{dil} = \frac{1}{3}\begin{bmatrix} \bar{B}_1 & \bar{B}_2 & \bar{B}_3 \\ \bar{B}_1 & \bar{B}_2 & \bar{B}_3 \\ \bar{B}_1 & \bar{B}_2 & \bar{B}_3 \\ 0 & 0 & 0 \\ 0 & 0 & 0 \\ 0 & 0 & 0 \end{bmatrix} \tag{4.6}$$

where, $\bar{B}_i$ is evaluated using:

$$\bar{B}_i = \frac{\int_{\Omega_e} B_i dV}{\int_{\Omega_e} dV} \tag{4.7}$$

Finally, a new definition of strain used in the B-bar method is given by $\bar{\mathbf{B}}$ such that $\bar{\mathbf{B}} = \mathbf{B}_{dev} + \bar{\mathbf{B}}_{dil} = \mathbf{B} - \mathbf{B}_{dil} + \bar{\mathbf{B}}_{dil}$. In a matrix representation, it is represented as:

$$\bar{\mathbf{B}} = \begin{bmatrix} \frac{\bar{B}_1+2B_1}{3} & \frac{\bar{B}_2-B_2}{3} & \frac{\bar{B}_3-B_3}{3} \\ \frac{\bar{B}_1-B_1}{3} & \frac{\bar{B}_2+2B_2}{3} & \frac{\bar{B}_3-B_3}{3} \\ \frac{\bar{B}_1-B_1}{3} & \frac{\bar{B}_2-B_2}{3} & \frac{\bar{B}_3+2B_3}{3} \\ B_2 & B_1 & 0 \\ 0 & B_3 & B_2 \\ B_3 & 0 & B_1 \end{bmatrix} \tag{4.8}$$

The B-bar method was implemented in the finite element code to analyze the beam impact problem described previously. As the problem of shear locking and the spurious kinematic modes resulting from the reduced integration is eliminated while using four noded quadrilateral elements with the B-bar method, four noded quadrilateral elements were adopted in the finite element analysis. The result of the dynamic analysis of the beam described earlier at the end of the 100th time step is shown in figure 4.11.

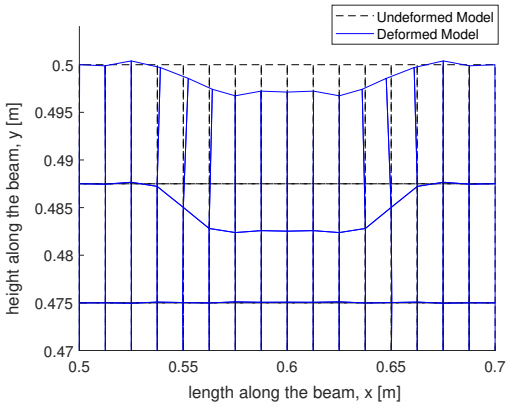

Figure 4.11: Deformation of the loaded part of the top edge of the beam using the B-bar method (Scale Factor : 1000)

4.2.3. RESULTS AND COMPARISON

The beam impact problem was analyzed using Modal Analysis and the B-bar method. The results of both the analyses are presented in this section. The effect of a mesh size and the variation of a Poisson's ratio on the horizontal and vertical deflections at three different sections are studied. Three different sections considered in the analyses are the top edge, a vertical cross-section at the mid-span and a cross-section inclined at 45° from the mid-span. The geometrical dimensions, density, elastic modulus, time step, loading parameters and boundary conditions described in box 4.2.1 are kept constant during the analyses. However, the Poisson's ratio and the mesh size are varied between a set of values. All results presented in this section are scaled by a factor equal to 40000. Also, it is to be noted that the horizontal deformation towards the right and the vertical deflection upward are considered positive in all the presented results.

MODAL ANALYSIS: MESH SENSITIVITY

The results of the top edge (both the horizontal and vertical deflections) were found to be dependent on the mesh size. The magnitude of deflections increased with the decrease in a mesh size. Not only the magnitude, but also the velocity of a wave propagation in the top edge was found to be dependent on the mesh size. It is to be noted that all results presented in the mesh sensitivity analyses are based on a beam with a Poisson's ratio equal to -0.90 and mesh size equal to [0.05 m 0.025 m 0.0125 m]. The horizontal and vertical deflections at the top edge after 640th time step is shown in figure 4.12. It can be observed in the figure that the speed of a wave propagation and the magnitude of the deflection is dependent on the mesh size. The velocity of a wave propagation decreases with the decrease in the mesh size, whereas the magnitude of deflection increases with the decrease in the mesh size.

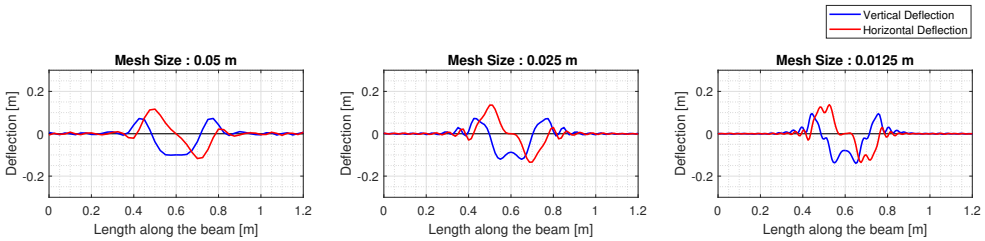

Figure 4.12: Horizontal and vertical deflection at the top edge of the beam (Scale Factor : 40000)

The effect of the mesh size on the horizontal and vertical deflections at a node on the top edge is shown in figure 4.13. The presented results were observed at the end of the 640th time step, and the considered node on the top edge is located at 0.55 m from the left edge. When the mesh size was halved, the vertical and horizontal deflections increased by approximately 20% and 5% respectively. The vertical deflection was found to be more mesh dependent because the loading was applied on the vertical direction as well.

Although the results on the top edge were strongly dependent on the adopted mesh size, the results on the other sections were observed to be less dependent on the mesh size. The effect of the mesh size on the deflection at a node on the inclined and vertical sections is shown in figure 4.14. The presented results were

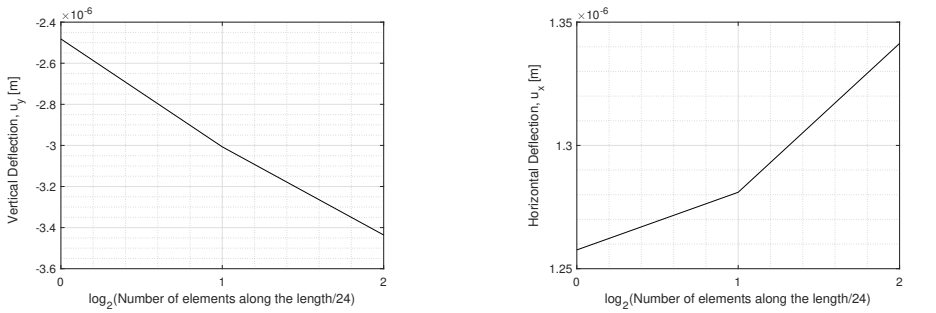

(a) Effect of mesh size on vertical deflection

(b) Effect of mesh size on horizontal deflection

Figure 4.13: Effect of mesh size on horizontal and vertical deflections at the top edge

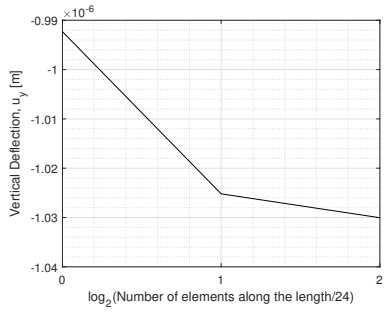

(a) Vertical deflection at vertical section

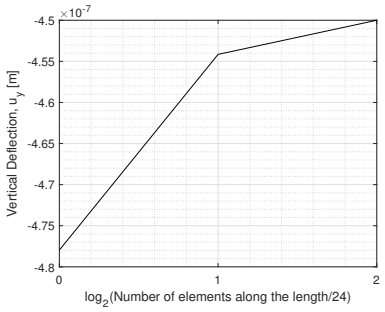

(b) Vertical deflection at inclined section

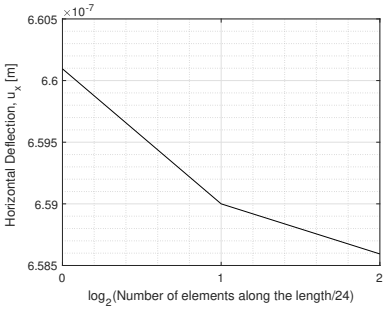

(c) Horizontal deflection at inclined section

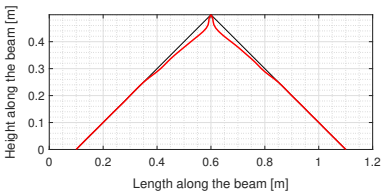

(d) Horizontal deformation along inclined section (Scale Factor : 40000)

Figure 4.14: Effect of mesh size on the horizontal and vertical deflections at the inclined and vertical sections

observed at the end of the 640th time step, and the considered node on the inclined section is located at 0.5 m from the left edge and 0.1 m from the top edge. Similarly, the node on the vertical section is located at 0.6 m from the left edge and 0.1 m from the top edge. When the mess size is reduced to one-fourth, the vertical deflection at a node in the vertical section, the vertical deflection at a node in the inclined section and the horizontal deflection at a node in the inclined section changes by approximately 3.5 %, 5.5 % and 0.2 % respectively. Observing the trend of graphs in figures 4.14(a) - 4.14(c), it can be predicted that the results approach a constant value with the further decrease in the mesh size.

It can be inferred from the results presented in figures 4.13 and 4.14 that the results on the top edge are mesh dependent. However, the results below the top edge are not very sensitive to the choice of a mesh size and therefore, the results can be interpreted from the physical sense as well. The unique characteristic observed in the beam impact analysis with a Poisson's ratio equal to -0.90 is the flow of materials towards the point of impact. The horizontal deformation of the inclined section at the end of the 640th time step is shown in figure 4.14(d). It can be observed that the material from the inclined sections at either side of the mid-span displaces towards the mid-span. This densifies the material below the impact and thus is useful in mitigating the impact load. It can also be observed in figure 4.12 that the horizontal deflection at the top edge on either side of the mid-span is also displaced towards the mid-span. However, this is not solely due to the effect of auxeticity. This behavior can be observed with the conventional values of the Poisson's ratio as well which will be discussed in the next section.

MODAL ANALYSIS: POISSON'S RATIO VARIATION

This section presents the results of the effect of a Poisson's ratio on the horizontal and vertical deflections at three different sections discussed previously. The results presented in this section are based on a mesh size of 0.025 m and a Poisson's ratio varied between [0.45 0 -0.45 -0.60 -0.75 -0.90]. The results at the end of the 640th time step observed at three different sections are presented in figures 4.15, 4.16, 4.17 and 4.18.

The horizontal and vertical deflections at the top edge for different values of a Poisson's ratio is shown in figure 4.15. The magnitude of the horizontal deflection at the top edge is found to be increasing with the increase in auxeticity. It can be observed in the figure that the nodes on the either side of the mid-span is displaced longitudinally towards the mid-span for any value of Poisson's ratio. The horizontal flow towards

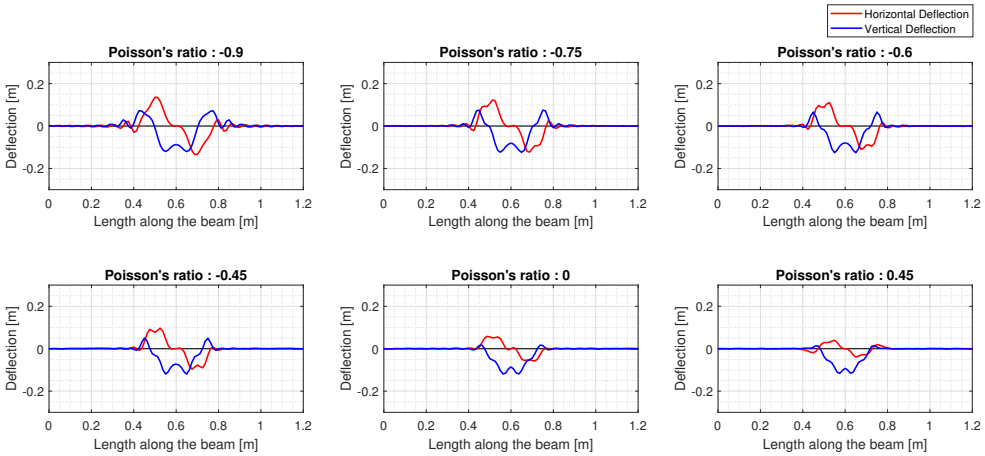

Figure 4.15: Effect of the Poisson's ratio on the deformation along the top edge (Scale Factor : 40000)

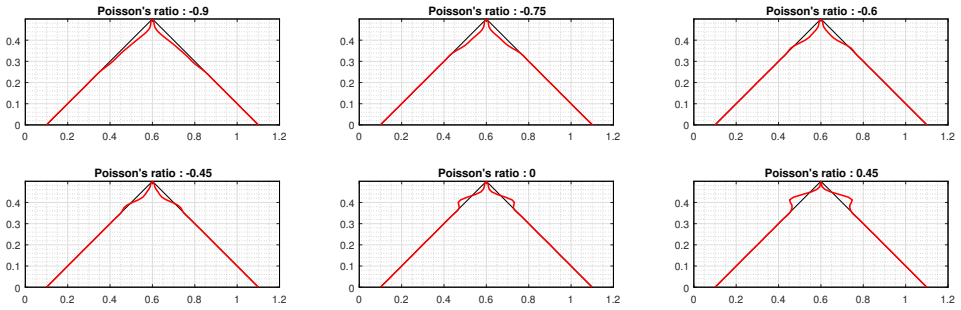

Figure 4.16: Effect of the Poisson's ratio on the horizontal deflection along the inclined section (Scale Factor : 40000)

the mid-span for conventional value of a Poisson's ratio is due to the pulling force exerted by the nodes that are vertically displaced downwards. However, for the auxetic range of a Poisson's ratio, the flow towards the mid-span is the combined effect of the pulling forced exerted by nodes and the effect of auxeticity. Besides the magnitude of the horizontal deflection, the speed of a wave propagation along the horizontal direction also increases with the increase in auxeticity. The velocity of a longitudinal wave propagating along the horizontal direction at the top edge is 330 ms^{-1}, 320 ms^{-1} and 260 ms^{-1} for the value of a Poisson's ratio equal to -0.90, -0.45 and 0.45 respectively. Similarly, the vertical deflection and the speed of wave carrying the vertical deflection along the top edge also increase with the increase in auxeticity.

The effect of the value of a Poisson's ratio on the horizontal deformation of the inclined sections is shown in figure 4.16. It can be observed in the figure that the nodes along the inclined sections on either side of the mid-span are longitudinally displaced towards the mid-span section for an auxetic range of the Poisson's ratio. This effect is solely due to the unconventional value of the Poisson's ratio as it can be noticed that the material flows away from the vicinity of impact for a Poisson's ratio equal to 0.45. The velocity of a wave propagating the horizontal deformation along the inclined section increases with the increase in the auxetic effect. The velocity of a wave propagating horizontal deformation was measured to be approximately equal to 1050 ms^{-1}, 530 ms^{-1} and 550 ms^{-1} for a Poisson's ratio equal to -0.90, -0.45 and 0.45 respectively. Although the velocity of a wave propagation increases, the magnitude of the horizontal deflection propagated along the section was found to be decreasing with the increase in the auxeticity.

Similarly, the effect of the variation of a Poisson's ratio on the vertical deformation along the inclined and vertical sections are shown in figures 4.17 and 4.18. Figure 4.17 shows the vertical deformation of the inclined sections at the end of the 640th time step, whereas figure 4.18 shows the magnitude of the vertical deflection along the vertical section at the beam mid-span after the 640th time step. The velocity of a wave propagating the vertical deformation along the inclined section was measured to be approximately 1050 ms^{-1}, 530 ms^{-1} and 550 ms^{-1} for a Poisson's ratio equal to -0.90, -0.45 and 0.45 respectively. Similarly, the wave propagating vertical deformation along the vertical section at mid-span was found to be traveling at the speed of approx-

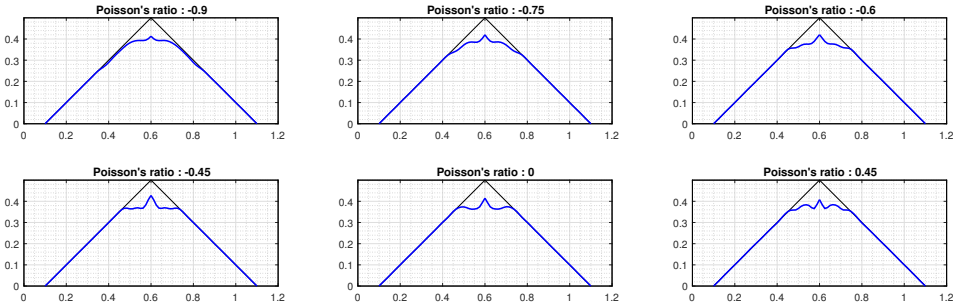

Figure 4.17: Effect of the Poisson's ratio on the vertical deflection along the inclined section (Scale Factor : 40000)

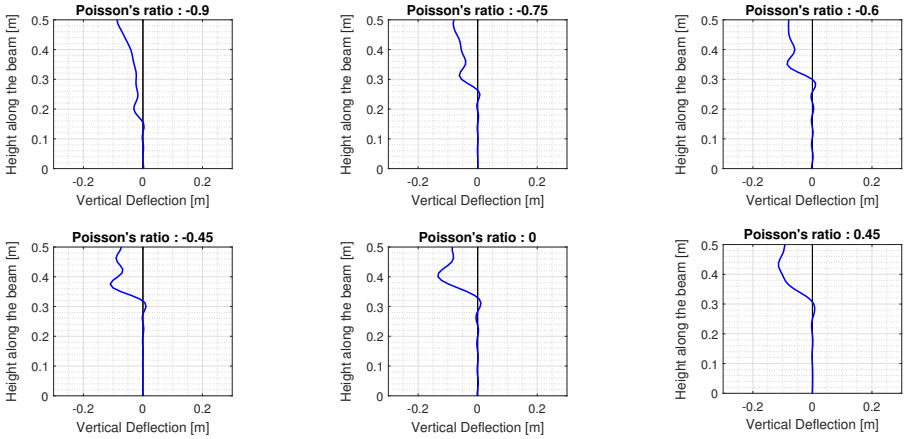

Figure 4.18: Effect of the Poisson's ratio on the vertical deflection along the vertical section (Scale Factor : 40000)

imately 1060 ms^{-1}, 540 ms^{-1} and 560 ms^{-1} for a Poisson's ratio equal to -0.90, -0.45 and 0.45 respectively. Therefore, it can be noted that the speed of a wave propagation increases with the increase in the auxeticity. However, the magnitude of the deformation the wave carries with it decreases with the increase in the auxeticity. Therefore, based on the observations of the propagation of the horizontal and vertical deflections along the inclined and vertical sections, it can be inferred that the effect of the impact load in highly auxetic beam is transferred earlier but with the reduced effect. This observation can be explained on the basis of the conservation of energy as well. The increase in the kinetic energy with the increase in auxeticity is compensated by the decrease in the potential(deformation) energy. This finding also shows the possible use of auxetics as a mechanical transformer.

RESULTS FROM THE B-BAR METHOD

The results obtained from the Modal analysis of the beam impact problem using six noded triangular elements and the B-bar method using four noded quadrilateral elements were found to be comparable with each other in many aspects. The magnitude of deflections and the speed of wave propagation at the inclined and vertical sections were always found to be within relative difference of 5 %. However, the results of the top edge were relatively different with each other. In general, the magnitude of the horizontal and vertical deflections were observed to be higher in Modal Analysis than the B-bar method. And, the speed of a wave was higher in the B-bar method compared to the results from Modal Analysis.

The results of the horizontal and vertical deflections at the top edge obtained after the 640th time step from the Modal Analysis and the B-bar method are shown in figure 4.19. The results are based on a mesh size of 0.025 m and a Poisson's ratio equal to -0.90. It can be observed in the figure that the results from the Modal Analysis have higher magnitude compared to the results from the B-bar method. However, the deformation wave front in the B-bar method is ahead of the wave front in the modal analysis. This observation can be related to the results obtained from the mesh sensitivity analyses. During the mesh sensitivity analyses, the magnitude of deflections was observed to be increasing with the decrease in the mesh size, whereas the speed of a wave decreased with the decrease in the mesh size. Although the adopted mesh size in the B-bar method

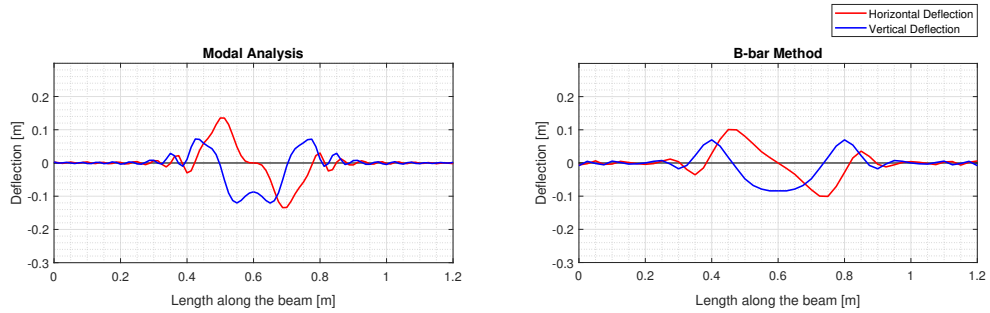

Figure 4.19: Comparison of results at the top edge from the B-bar method and Modal Analysis (Scale Factor : 40000)

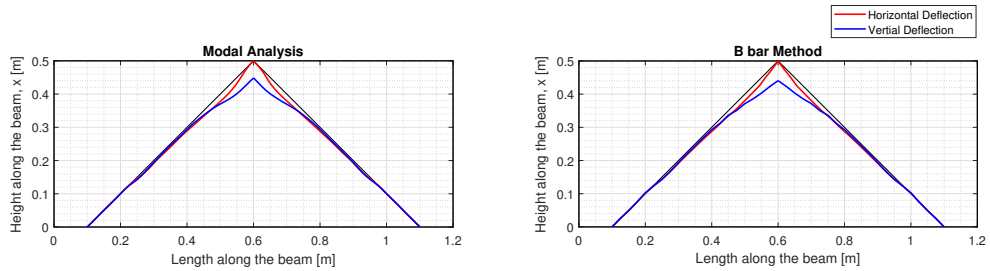

Figure 4.20: Comparison of results along the inclined section from the B-bar method and Modal Analysis (Scale Factor : 40000)

and the modal analysis is same, the element types used in both methods are different. The adjacent nodes in the Modal analysis and the B-bar method are at a distance of 0.0125 m and 0.025 m respectively. Hence, the effective discretization of the top edge is finer with the modal analysis than the B-bar method. This explains the difference in the magnitude of deflections and the speed of a wave propagation at the top edge using the modal analysis and the B-bar method.

The results of the horizontal and vertical deflection at the inclined sections obtained at the end of the 1000th time step from the Modal analysis and the B-bar method are shown in figure 4.20. The magnitude of deflection and the speed of a wave propagation obtained from both methods were found to be close to each other.

The results obtained from the dynamic analyses of the beam impact problem using Modal Analysis and the B-bar method have highlighted the effect of auxeticity in alleviating the effect of an impact force on a beam. The increase in the auxeticity leads to an increase in the speed of a wave propagation but with the reduction in the intensity of the deformation that it propagates in the beam. The flow of materials towards the point of impact increases with the increase in auxeticity. This results in the densification of the area under the impact, thus reducing the effect of impact. The results portrayed the prospective use of the auxetic structures in mediating the impact loads. Although the results obtained in the sections away from the top edge of the beam were reasonable from the physical point of view, the results on the top edge were still found to suffer from spurious modes and mesh dependency.

4.3. ORTHOTROPIC MATERIALS

The studies so far investigated the effect of auxeticity in linear elastic isotropic continuum loaded in various conditions. However, in practice, the auxeticity is achieved through cellular structures such as re-entrant honeycomb structures. The re-entrant honeycomb structure is highly orthotropic in nature. Therefore, it would be interesting to observe the effect of auxeticity in a linear elastic orthotropic continua. The examination of the effect of auxeticity in orthotropic materials would provide link between computational analyses of the continuum model and the cellular structure model in sections 5 and 6.

The relation between strain and stress in a linear elastic material is given by the elastic compliance relation shown in equation 3.3. The elastic compliance relation in index notation can be written as:

$$\varepsilon_{ij} = c_{ijkl}\sigma_{kl} \tag{4.9}$$

Since the strain and stress tensors are symmetric (i.e. $\varepsilon_{ij} = \varepsilon_{ji}, \sigma_{ij} = \sigma_{ji}$) the elastic compliance matrix given by **C** is also symmetric for a linear elastic material. This means, out of 36 components of the compliance matrix, only 21 components need to be defined due to the symmetry. The elastic compliance matrix is defined by the material properties (elastic constants). The number of elastic constants required to define **C** completely depends on the number of planes of symmetry it possesses.

A fully anisotropic material does not have any planes of symmetry, and therefore requires 21 independent elastic constants to define the compliance matrix **C**. Whereas, an orthotropic material has three mutually orthogonal planes of symmetry. The material properties and behavior are independent of the direction within each orthogonal planes. These material properties require 9 elastic constants to define the compliance matrix. The material which is homogeneous i.e. material properties and behavior are independent of any directions and planes is called isotropic material. Only 2 independent elastic constants are required to define the compliance matrix for an isotropic material.

The behavior of an isotropic material, and the effect of having negative Poisson's ratio in such materials are already discussed in previous sections. Now, the consequences of having a negative Poisson's ratio in an orthotropic material will be discussed. The compliance matrix for an orthotropic material is given by:

$$\mathbf{C} = \begin{bmatrix} \frac{1}{E_1} & -\frac{\nu_{21}}{E_2} & -\frac{\nu_{31}}{E_3} & 0 & 0 & 0 \\ -\frac{\nu_{12}}{E_1} & \frac{1}{E_2} & -\frac{\nu_{32}}{E_3} & 0 & 0 & 0 \\ -\frac{\nu_{13}}{E_1} & -\frac{\nu_{23}}{E_2} & \frac{1}{E_3} & 0 & 0 & 0 \\ 0 & 0 & 0 & \frac{1}{G_{23}} & 0 & 0 \\ 0 & 0 & 0 & 0 & \frac{1}{G_{31}} & 0 \\ 0 & 0 & 0 & 0 & 0 & \frac{1}{G_{12}} \end{bmatrix} \tag{4.10}$$

where E_i is the Young's modulus in direction i, G_{ij} is the shear modulus in the direction i on the plane whose normal is in the direction j, and ν_{ij} is the Poisson's ratio defining deformation in the direction j when load is applied in i-direction. Due to the symmetry of the compliance matrix, $\frac{\nu_{21}}{E_2} = \frac{\nu_{12}}{E_1}$, $\frac{\nu_{31}}{E_3} = \frac{\nu_{13}}{E_1}$ and $\frac{\nu_{23}}{E_2} = \frac{\nu_{32}}{E_3}$. Therefore, only 9 elastic constants need to be defined in the compliance matrix, **C**.

The components of the compliance matrix indicate that the strain produced in lateral direction due to the longitudinal stress is proportional to $-\frac{\nu_{ji}}{E_j}$ where j is the lateral direction and i is the loading direction. Therefore, the deformation behavior is still similar to the one observed and discussed in an isotropic material. In the auxetic range of Poisson's ratios, the material will continue to expand laterally when stretched, and contract laterally when compressed. The only difference is that the Poisson's effect is not the same in both lateral directions, and depends on the direction of loading.

However, the response of an orthotropic material when loaded in shear is different when compared with an isotropic material. It can be seen in equation 4.10 that the shear modulus G is no longer dependent on the Young's modulus E and the Poisson's ratio ν. It is instead an independent elastic constant. Therefore, the behavior of an orthotropic material does not change with the change in the Poisson's ratio under shear loading.

Since the shear modulus is an independent elastic constant, the shear wave velocity in an orthotropic material with a given value of the shear modulus G_{ij} stays constant too. The longitudinal and shear wave velocities which only depend on the specified value of Young's modulus E_{ij} and shear modulus G_{ij} respectively do not vary with the Poisson's ratio. However, the dilatation wave velocity continues to depend on a Poisson's ratio and is therefore affected by the variation of the Poisson's ratio.

The stiffness matrix for an orthotropic material is given by the inverse of an elastic compliance matrix shown in equation 4.10. The stiffness matrix is obtained as:

$$\mathbf{D} = \begin{bmatrix} \frac{1-\nu_{23}\nu_{32}}{E_2E_3\Delta} & \frac{\nu_{21}+\nu_{31}\nu_{23}}{E_2E_3\Delta} & \frac{\nu_{31}+\nu_{21}\nu_{32}}{E_2E_3\Delta} & 0 & 0 & 0 \\ \frac{\nu_{12}+\nu_{13}\nu_{32}}{E_1E_3\Delta} & \frac{1-\nu_{31}\nu_{13}}{E_2E_3\Delta} & \frac{\nu_{32}+\nu_{31}\nu_{12}}{E_1E_3\Delta} & 0 & 0 & 0 \\ \frac{\nu_{13}+\nu_{12}\nu_{23}}{E_1E_2\Delta} & \frac{\nu_{23}+\nu_{13}\nu_{21}}{E_1E_2\Delta} & \frac{1-\nu_{12}\nu_{21}}{E_1E_2\Delta} & 0 & 0 & 0 \\ 0 & 0 & 0 & G_{23} & 0 & 0 \\ 0 & 0 & 0 & 0 & G_{31} & 0 \\ 0 & 0 & 0 & 0 & 0 & G_{12} \end{bmatrix} \tag{4.11}$$

where,

$$\Delta = \frac{1-\nu_{12}\nu_{21}-\nu_{23}\nu_{32}-\nu_{31}\nu_{13}-2\nu_{12}\nu_{23}\nu_{31}}{E_1E_2E_3} \tag{4.12}$$

Now, assuming $\nu_{23} = \nu_{31} = 0$, the plane wave of dilatation speed in direction - 1 and direction - 2 are given by: $\sqrt{\frac{E_1}{\rho(1-\nu_{12}\nu_{21})}}$ and $\sqrt{\frac{E_2}{\rho(1-\nu_{12}\nu_{21})}}$ respectively. It can be observed in these expressions that the dilation wave velocity in an orthotropic material is still a function of the Poisson's ratio.

4.4. SUMMARY OF DYNAMIC BEHAVIOR IN AN AUXETIC CONTINUUM

The effect of auxeticity in the response of a structure subjected to various dynamic loading conditions was examined in this chapter. The study started with the analysis of a one-dimensional wave motion and later focused on the effect of auxeticity in a two-dimensional wave motion. The computational analysis of a shear wave problem in auxetic solids showed that the shear wave velocity is higher in an auxetic material than in a conventional material. The rate of the increase in the shear wave velocity is found to be increasing when a material becomes more auxetic. For a Poisson's ratio smaller than -0.5, the shear wave velocity was evaluated to be higher than the longitudinal wave velocity. Although the ratio of the shear wave velocity to dilatation wave velocity decreases continuously in the auxetic range, the shear wave velocity never exceeds the dilatation wave velocity in the isotropic limit of a Poisson's ratio.

The dynamic analyses of one-dimensional motion, i.e. dilatational wave problem and shear wave problem were found to be in correspondence with the theory. However, the dynamic analysis of a two-dimensional motion (beam impact problem) revealed some numerical complications due to the presence of spurious modes. Two additional computational approaches; Modal Analysis and the B-bar method were adopted to analyze the beam impact problem. The results obtained from the dynamic analyses using both approaches showed that in an auxetic beam subjected to impact loading, the material under the impact flows towards each other and therefore densifies the area under the impact. This results in the increased indentation resistance and is useful to mitigate the effect of an impact loading. The wave speed was observed to be increasing with the increase in the auxeticity. Although, the increase in auxeticity leads to an increase in a wave speed, the intensity of the deformation it propagates was found to be decreasing with the increasing auxetic effect. To summarize, it can be noted that the use of the Modal Analysis and the B-bar method was able to fix the problem of spurious modes and the mesh dependency in the middle portion of the beam. However, the results on the top edge of the beam were still found to be strongly dependent on the mesh size. The comparison of both computational approaches and the results of the mesh sensitivity analyses highlighted the need of additional kinematic strains at the top edge of the beam.

The behavior of orthotropic auxetic material subjected to uniaxial loading is similar to the response of uniaxially loaded auxetic isotropic material. The compression results to contraction in both longitudinal and lateral directions, and the stretching results to expansion. The main difference in the deformation behavior of two materials is that the Poisson's effect is dependent on the direction of loading in orthotropic materials, whereas it is independent of the loading direction in isotropic materials. The major difference in two materials occur when loaded in shear. The shear modulus in orthotropic material is an independent elastic constant. Therefore, the shearing deformation in orthotropic material is not affected by the auxeticity. As a result, the shear wave velocity is also unchanged due to the auxeticity in orthotropic materials. However, the dilatation wave velocity in orthotropic material is still a function of Poisson's ratio, and is therefore affected by the auxeticity.

5

MICRO-STRUCTURE - STATIC ANALYSIS

The man-made auxetic materials are designed by adapting the geometry of the structure into desired shape and size. Many cellular structures have been modified to specific configurations to achieve auxeticity; examples are: re-entrant honeycomb structures, chiral structures, rotating polygons etc. Among them, the re-entrant honeycomb structure was one of the first auxetic structure introduced and studied. The remaining part of the thesis is focused on studying the response of re-entrant structures under various static as well as dynamic loading conditions. The two-dimensional re-entrant structures are formed by modelling array of hexagonal honeycomb unit cells with negative angle which explains the name re-entrant. The representation of conventional honeycomb unit cell and re-entrant honeycomb unit cell is shown in figure 5.1. Re-entrant structures appear to be an interesting structure due to the great range of auxeticity it can exhibit. The mechanics of honeycomb cellular structures was extensively studied by Gibson [4]. Expressions Gibson proposed to evaluate the mechanical properties of hexagonal honeycomb structures revealed that the auxeticity can be easily achieved in the honeycomb structures by forming them with a negative angle. On the application of compressive load on either direction, the inclined ribs bend and move inward resulting in an auxetic behavior. The level of auxeticity it exhibits depends on the ratio of the length of cell members and the re-entrant angle. In addition to the geometrical parameters, the auxeticity it exhibits also depends on the direction of loading, implying the response is not isotropic. Similarly, the stiffness of the structure is dependent on the relative density and properties of the cell member in addition to the geometrical dimensions.

This section of the thesis is focused on finding the answer to the research question relating to the design of a cellular structure that exhibits negative Poisson's ratio. The response of a unit cell and the structure formed by array of those unit cells when subjected to uniaxial loading, biaxial loading, shear loading and bending is studied. The study focuses on the effect of geometrical parameters of cell member on the mechanical properties of re-entrant structures. The results are obtained from the finite element simulations and compared with the analytical solutions proposed by Gibson [4]. The finite element analyses are performed using a finite element package programmed in MATLAB. The finite element code programmed by van der Meer [23] was modified to include various tools and features required for this thesis.

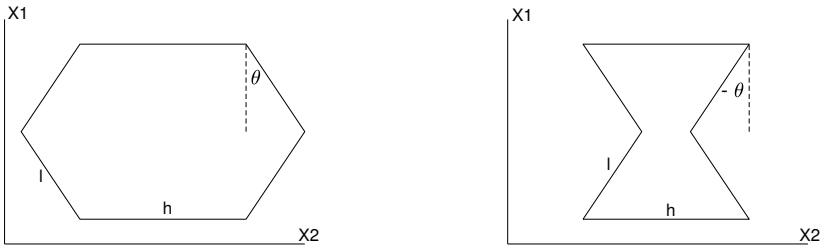

(a) (b)

Figure 5.1: (a) Unit cell of conventional honeycomb (b) Unit cell of re-entrant honeycomb

5.1. UNI-AXIAL LOADING

The re-entrant structure shown in figure 5.1(b) is subjected to external load in either X1 or X2 direction as shown in the figure, throughout the thesis. When load is applied in the X1 direction, the inclined ribs bend and move according to the direction of applied load; tension causes the inclined ribs to move outward, and compression causes the ribs to move inward. Similarly, when the load is applied in X2 direction, similar deformation mechanism can be observed. The relation between the effective mechanical properties of honeycomb structure, and the geometrical dimension and cell member properties are shown in equations 2.2 - 2.4 which only include the bending deformation, and neglect the axial and shear deformations. Gibson also proposed a set of relations including axial and shear deformations [4]. The analytical solutions including these additional deformations are used in this study.

Poisson's ratio and the effective Young's modulus in each direction is obtained computationally. The computational analysis is first performed on an unit cell, and then on the structure formed from the arrays of the unit cells. The effect of geometrical parameters: the aspect ratio h/l and a re-entrant angle θ on effective Poisson's ratio and elastic modulus is investigated. The re-entrant angle is varied between [-15°, -30°, -45°, -60°, -75°]. Similarly, the aspect ratio (h/l) is varied between [1.5, 2.0, 2.5, 3.0]. However, for a re-entrant honeycomb structure, the length of horizontal rib, h must be larger than the absolute value of $2lsin\theta$. Therefore, the h/l ratio equal to 1.5 will not be considered with $\theta = -60°$ and $-75°$. Also, it has to be noted that the results corresponding to $h/l = 1.5$ and $\theta < -60°$ should not be considered in all analytical graphs that are presented as re-entrant honeycomb structure with those parameters can not be realized.

5.1.1. LOADING IN X1

The unit cell shown in figure 5.1(b) is first loaded in the X1 direction. The analytical formula proposed by Gibson for the Poisson's ratio and effective Young's modulus in X1 direction are:

$$\nu_{12} = \left[\frac{cos^2\theta}{(h/l + sin\theta)sin\theta}\right]\left[\frac{1 + (1.4 + 1.5\nu_s)(t/l)^2}{1 + (2.4 + 1.5\nu_s + cot^2\theta)(t/l)^2}\right] \tag{5.1}$$

$$E_1 = \left[\frac{E_s t^3 cos\theta}{l^3(h/l + sin\theta)sin^2\theta}\right]\left[\frac{1}{1 + (2.4 + 1.5\nu_s + cot^2\theta)(t/l)^2}\right] \tag{5.2}$$

where E_s, ν_s, t are the Young's modulus, Poisson's ratio and thickness of the cell wall material respectively. Similarly, h, l, θ represent the length of horizontal rib, the length of inclined rib and the re-entrant angle respectively. The terms in the second bracket in each equations are derived including the axial and shear deformations in the cell members.

The variation of the Poisson's ratio ν_{12} with respect to θ for different values of h/l is shown in figure 5.2. The results are presented for the value of $t/l = 0.1$ and 0 Poisson's ratio of the cell wall material. It can be seen in the figure that for re-entrant angles, the Poisson's ratio is negative. Also, the magnitude of Poisson's ratio is significantly affected by varying the angle θ and the aspect ratio h/l.

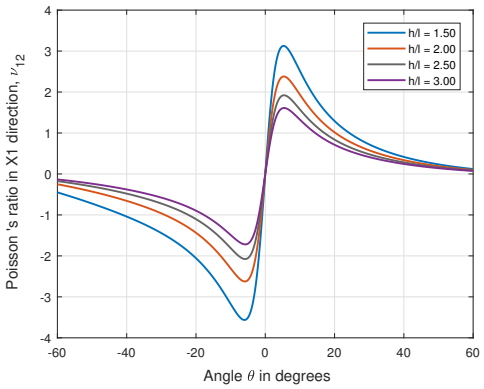

Figure 5.2: Variation of ν_1 with respect to θ for different values of h/l

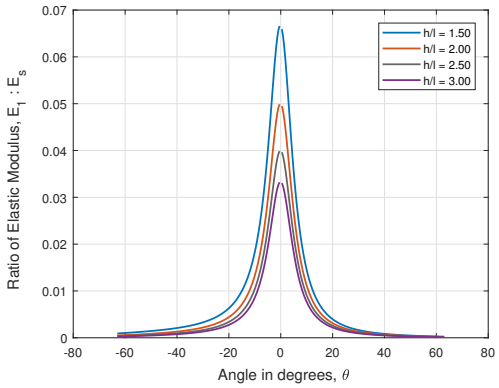

Figure 5.3: Variation of $E_1 : E_s$ with respect to θ for different values of h/l

In a conventional honeycomb, for a given value of angle θ, the Poisson's ratio ν_{12} increases with the decrease in the aspect ratio h/l. Similarly, in the re-entrant honeycomb, for a given value of angle θ, the Poisson's ratio becomes more negative with the decrease in the ratio h/l. Except for a small range of angles near the boundary between a conventional and a re-entrant honeycomb, the absolute value of Poisson's ratio in X1 direction decreases with the increase in the absolute value of angle θ. The result shown in figure 5.2 indicates the possibility of designing an auxetic structure with the Poisson's ratio more negative than -1.

The variation of the ratio of the effective Young's modulus in X1 direction and the Young's modulus of the cell wall material ($E_1 : E_s$) with respect to angle θ for different values of aspect ratio h/l is shown in figure 5.3. Like the results of the Poisson's ratio ν_{12}, the results of E_1 shown in figure 5.3 is also obtained for the value of $t/l = 0.1$ and 0 Poisson's ratio of the cell wall material.

It can be observed in figure 5.3 that the effective Young's modulus in X1 direction is significantly smaller than the Young's modulus of the member which forms the cellular structure. The ratio decreases further with the increase in the aspect ratio (h/l). Also, for a given ratio of h/l, the effective Young's modulus in X1 direction decreases with the increase in the magnitude of the angle θ in both conventional and re-entrant range. The effective Elastic modulus is also inversely proportional to the cube of the cell member slenderness $(l/t)^3$. It means the ratio of the effective elastic modulus of cellular structure to the elastic modulus of a cell wall material increases with the decrease in the slenderness (i.e. increase in relative density of the structure). The variation of the ratio with respect to θ for a set of values of t/l, and a fixed value of $h/l = 2$ is shown in figure 5.4.

The results shown in figures 5.2 and 5.3 highlight the dependence of effective mechanical properties on geometrical parameters of honeycomb unit cell. More importantly, results shows that the geometrical parameters can be easily manipulated to have a desired value of the effective mechanical properties. The analytical results shown in figures 5.2 and 5.3 are now compared with the computational results.

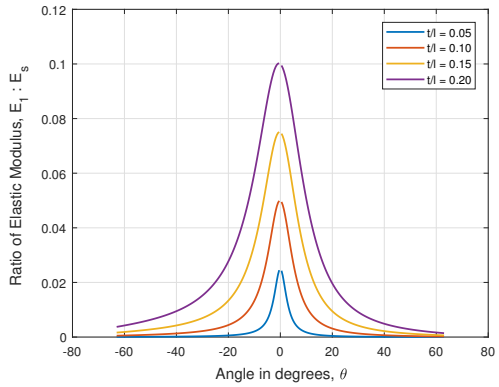

Figure 5.4: Variation of $E_1 : E_s$ with respect to θ for different values of t/l

Box 5.1.1: Unit Cell Loaded in X1

A unit cell is modelled as a rigidly connected network of beams. As shown in figure 5.1, the unit cell comprises of six cell members which are modelled as beams. Each member is discretized into a number of two noded beams with three degrees of freedom in each node. The beam element is formulated using Timoshenko beam theory. The three degrees of freedom in each node are: two translations (u_x, u_y) in the (x, y) plane and a rotation θ_z. The two noded beam element with six degrees of freedom is shown in figure 5.5.

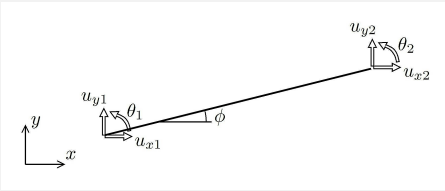

Figure 5.5: Two noded beam element with six degrees of freedom [22]

These degrees of freedoms continuously vary within the element, and is approximated by the linear shape functions (N_1, N_2).

$$\begin{bmatrix} u_x \\ u_y \\ \theta_z \end{bmatrix} = \begin{bmatrix} N_1 & 0 & 0 & N_2 & 0 & 0 \\ 0 & N_1 & 0 & 0 & N_2 & 0 \\ 0 & 0 & N_1 & 0 & 0 & N_2 \end{bmatrix} \begin{bmatrix} u_{x1} \\ u_{y1} \\ \theta_{z1} \\ u_{x2} \\ u_{y2} \\ \theta_{z2} \end{bmatrix} \tag{5.3}$$

Axial strain $(\varepsilon = u'_x)$, shear strain $(\gamma = u'_y - \theta)$ and curvature $(\kappa = \theta')$ represent deformations in the beam element. Finally, the strains and the curvature are related to the forces and moment through: $N = EA\varepsilon$, $V = GA_s\gamma$ and $M = EI\kappa$.
The deformed and undeformed model of the unit cell loaded in X1 direction is shown in figure 5.6. The unit cell is loaded at the top two nodes (A and B) with compressive load in X1 direction. The cell wall members that are connected to form the re-entrant honeycomb are assumed to be isotropic materials with 2e8 Nm^{-2} Young's modulus, 0 Poisson's ratio and 0.01 m out of plane width. The slenderness of the beam (l/t), an angle θ and the aspect ratio h/l are taken to be 10, -45° and 2 respectively. Each beam member is discretized into 8 elements. It can be observed in figure 5.6 that when compressive load is applied, the inclined ribs move inward thus giving the auxetic response.

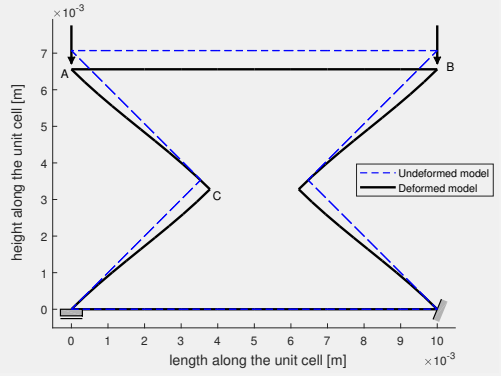

Figure 5.6: Deformation of a unit cell of re-entrant honeycomb loaded in X1 direction

All three degrees of freedom at the right bottom corner node of the unit cell, and two degrees of freedom: vertical displacement and rotation at the left bottom corner are restrained during the finite

element analysis of the unit cell. The Poisson's ratio is observed by evaluating the negative ratio of horizontal strain and vertical strain at point C (shown in the figure 5.6).
As already mentioned before, the inclined ribs bend during the deformation process. Therefore, the mesh sensitivity study is carried out to find the sufficient number of elements required to reproduce the bending of the inclined ribs accurately. After selecting the suitable mesh size, the unit cell analyses are repeated for set of values of θ and h/l. Finally, the computational results are compared with the analytical predictions for all selected cases.

MESH SENSITIVITY

A unit cell is modelled with the cell wall material properties listed in Box 5.1.1. The aspect ratio h/l and angle θ are used as 2 and -45° respectively. The unit cell is loaded in X1 direction as shown in figure 5.7. The boundary condition used in the finite element model is explained in box 5.1.1, and is evident from figure 5.7. Analyses are run by dividing each cell member into 2, 4, 8, 16, 32 and 64 elements. Since the inclined ribs undergo bending deformation, rotation θ_z is analyzed at a fixed point, P (shown in figure 5.7) in each analysis. Point P is the midpoint of the left bottom inclined rib.

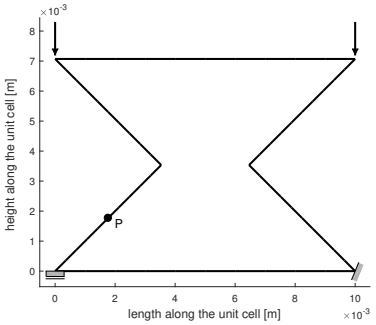

Figure 5.7: Model of the unit cell for mesh sensitivity analyses

The unit cell is loaded with incremental load upto 50 load steps. At each load step, the load on each loaded node increases by 0.1 N. By the end of the final load step, 36 % deformation is produced at loaded point in the direction of loading. The results of the mesh sensitivity analyses are presented in figures 5.8 and 5.9. The variation of rotation θ_z with respect to different mesh sizes after load step 5, 25 and 50 are shown in figure 5.8(a) - 5.8(c). The variation of the rotation with respect to load step for different mesh sizes is shown in figure 5.8(d). It can be observed in figures that the rotation θ_z converges for more than 8 elements. The difference in evaluating the rotation θ_z after 50th load step between using 8 and 64 elements is found to be 0.46%. However, the analysis using 64 elements was 5 times computationally expensive compared to the analysis using 8 elements.

The deformed unit cell after 50th load step while using 2, 4, 8 and 64 elements per member is shown in figure 5.9. It can be easily noticed that the unit cell with 2 elements per member was not able to reproduce the appropriate deformation. Although the performance of using 4 elements is significantly better than the one with 2 elements, the bending of ribs is not as smooth as the one obtained while using 8 or more elements. Even for such a large deformation produced in load step 50, the results of using 8 and 64 elements are found to be comparable with each other. Therefore, taking into consideration the relative difference in the deformation result and the computation time, 8 elements per cell member is found to be sufficient. The remaining analyses are performed using 8 elements per cell member. The presented results of mesh sensitivity analyses are based on a single unit cell. A honeycomb structure on another hand is made from arrays of unit cells. Number of unit cells are connected to each other to form a structure. The suitable mesh size per member of the unit cell at that situation is also dependent on the size and the numbers of the unit cells that are used to model the structure.

ANALYSIS OF A UNIT CELL

A unit cell built from the cell wall material described in the Mesh Sensitivity analysis is modelled using $h/l = 2$ and $\theta = -45°$. The top two corner nodes are loaded with a point load for 10 load steps. The load increases by 0.1 N at each load step. The normal force, shear force and bending moment developed in the members

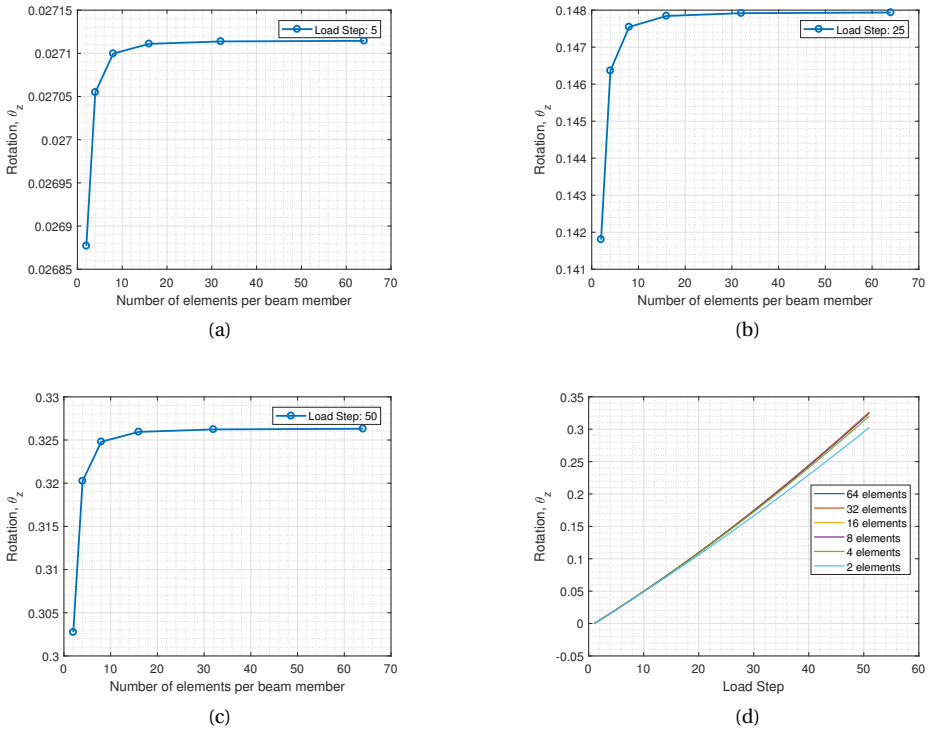

Figure 5.8: Variation of rotation θ_z with respect to number of elements in a member at (a) 5 Load Step (b) 25 Load Step (c) 50 Load Step (d) Variation of rotation θ_z with respect to load steps for different mesh sizes

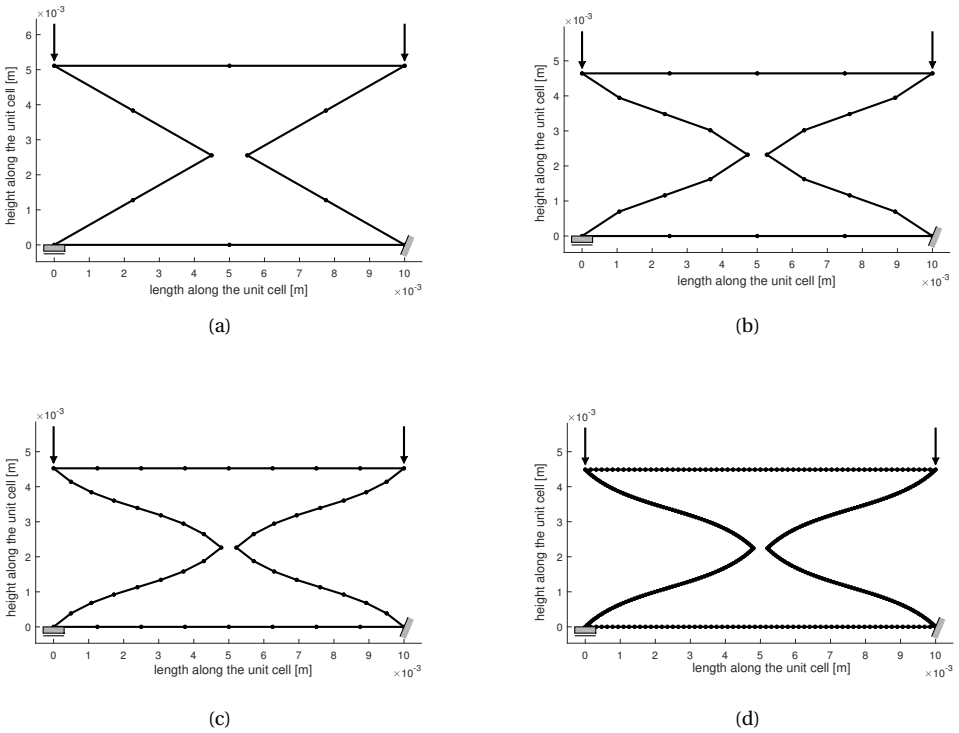

Figure 5.9: Deformed unit cell at final load step using (a) 2 elements (b) 4 elements (c) 8 elements (d) 64 elements

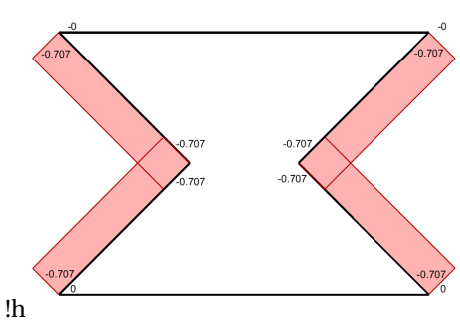

!h

(a) Normal force diagram in a unit cell

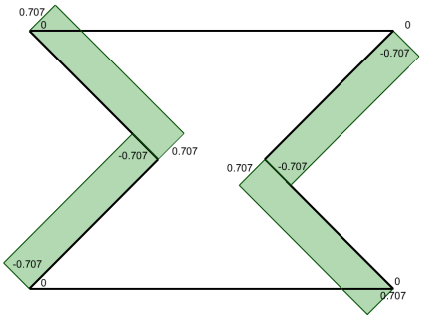

(b) Shear force diagram in a unit cell

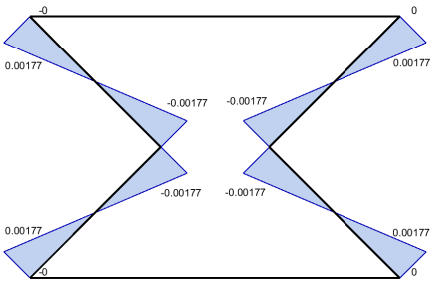

(c) Bending Moment diagram in a unit cell

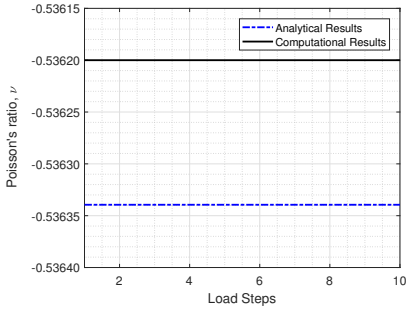

(d) Poisson's ratio ν_{12} when loaded in X1 direction

Figure 5.10: Poisson's ratio and Force, Moment Diagram in a unit cell loaded in X1 direction

of the unit cell after the 10th load step is shown in figure 5.10(a-c). Also, the Poisson's ratio of the unit cell is recorded at each load step and is shown in figure 5.10(d). The presented results are based on geometrical linear analysis. Therefore, the Poisson's ratio is independent of the load step. As the analytical result presented in equation 5.1 is also based on a straight undeformed member and geometrically linear deformation, the analytical and computational results are compared with each other. The values of $h/l, t/l$ and θ for the analyzed case of unit cell are substituted in equation 5.1, and plotted with the computational results in figure 5.10(d).

The load applied on the top two corner nodes is transferred to the members in the form of axial and shear load. Since the re-entrant angle is -45°, the axial and shear force developed on the inclined members due to the external load is same. These forces are different when any other value is chosen for angle θ. It can be observed in figures 5.10(a) and 5.10(b) that no axial and shear force are present in the horizontal cell members. As connections between cell members are rigid, the applied loading condition does not create any deformation in the horizontal cell members, thus resulting in no force developed in them. The inclined members undergo bending deformation as predicted in the theory.

The bending moment diagram developed in the inclined members is shown in figure 5.10(c). It can be observed in figure 5.10(d) that the computational result of the Poisson's ratio exhibited by the unit cell complies with the theoretical prediction. The relative error between the analytical and computational results was found to be only 0.03%.

The Poisson's ratio exhibited by the unit cell including geometrical non-linearity is shown in figure 5.11. The legends GNL - on and GNL - off in figure 5.11 indicate the inclusion and exclusion of geometrical non-linearity in computational analyses. It can be observed in figure 5.11 that the Poisson's ratio exhibited by the unit cell is no longer constant. Since the geometrical non-linearity is included, the Poisson ratio in each load step is now based on the updated geometrical configuration of the unit cell. When the incremental compressive load is applied at points A and B (shown in figure 5.6), the position of point C with respect to A changes with the increasing load step. The re-entrant angle θ between A and C increases with the increase in the compressive load. As the Poisson's ratio is dependent on the re-entrant angle, the Poisson's ratio also varies with the increasing load step. It was observed in figure 5.2 that the Poisson's ratio in X1 direction becomes less negative with the increase in a re-entrant angle. Similar observation can be made in figure 5.11 as well. The Poisson's ratio tends to grow towards 0 with the increasing load step i.e. increasing re-entrant angle θ. The

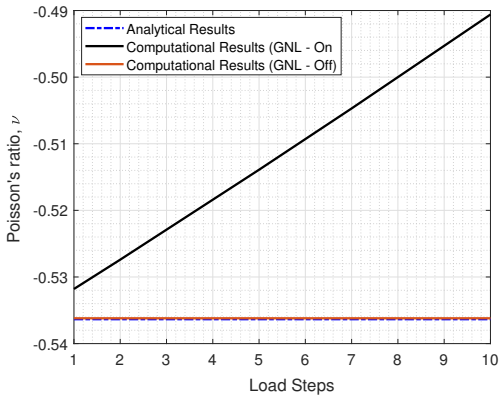

Figure 5.11: Comparison of analytical and computational results of Poisson's ratio exhibited by the unit cell loaded in X1 direction

Table 5.1: Analytical and computational results (linear analyses) of Poisson's ratio (ν_{12}) for different values of h/l and θ

h/l	**1.5**			**2.0**			**2.5**			**3.0**		
θ	**CR**	**AR**	**E(%)**	**CR**	**AR**	**E(%)**	**CR**	**AR**	**E(%)**	**CR**	**AR**	**E(%)**
-15°	-2.527	-2.532	0.201	-1.801	-1.805	0.198	-1.399	-1.402	0.197	-1.144	-1.146	0.203
-30°	-1.442	-1.443	0.061	-0.962	-0.962	0.057	-0.706	-0.707	0.095	-0.551	-0.552	0.118
-45°	-0.874	-0.875	0.029	-0.536	-0.536	0.026	-0.387	-0.387	0.043	-0.302	-0.302	0.042
-60°	-	-	-	-0.251	-0.251	0.026	-0.174	-0.174	0.044	-0.134	-0.134	0.015
-75°	-	-	-	-0.066	-0.066	0.055	-0.045	-0.045	0.076	-0.034	-0.034	0.112

analytical results and computational results of the geometrical linear analysis are based on an undeformed geometrical configuration and a constant angle θ. Therefore, the Poisson's ratio stays constant as expected.

Also, the computational results including geometrical nonlinear effects can not be compared with the analytical results obtained by using the updated re-entrant angle θ, because the analytical relation is derived on assumptions of constant strain rate and undeformed ribs. However, the computational results are based on the updated geometry of the unit cell as the inclined ribs are already bent with the application of an external load. Thus, the results of geometrical nonlinear analysis cannot be compared with the analytical relations given in equation 5.1.

Now, since the finite element code is validated through the close comparison of computational and analytical results, 17 more analyses are performed to compute the Poisson's ratio of unit cell modelled using a set of values of θ and h/l.. As the computational analysis does not include the geometrical non-linearity, the Poisson's ratio is independent of the load step as shown in figure 5.10(d). The results are shown in table 5.1 where index CR, AR and E(%) mean computational results, Analytical results and relative error percentage respectively. It must be noted that analyses with $h/l = 1.5$, and $\theta = -60°$ and $-75°$ are omitted because a re-entrant honeycomb structure can not be realized with those parameters.

It can be observed in table 5.1 that all results are within 0.5% error range. The variation of a Poisson's ratio with the aspect ratio h/l and angle θ is found to agree with the analytical results presented in figure 5.2. The Poisson's ratio shifts towards zero with the increase in the ratio h/l and the magnitude of the re-entrant angle θ. The consistent results obtained from the analytical predictions and computational analyses show that the great range of auxeticity can be achieved through a re-entrant honeycomb unit cell. In addition, the possibility to predict the geometrical nonlinear behavior of a re-entrant honeycomb structure using a finite element analysis helps to resolve the limitation of the analytical formula to predict geometrical nonlinear behavior. The validation of the finite element code provide a freedom to extend the study of re-entrant honeycomb unit cells to structural level and relatively complex loading conditions, such as: bi-axial loading and bending.

ANALYSIS OF ARRAYS OF UNIT CELL

A structural member is formed by the connection of a number of arrays of unit cell. The behavior of the structure can be predicted based on the analysis of a unit cell as all unit cells deform in a similar manner. A beam which is formed by the repetition of a unit cell with dimensions: $h = 10$ mm, $l = 5$ mm and $\theta = -30°$ in both X1 and X2 directions is shown in figure 5.12.

The assembly of unit cells is loaded in X1 direction as shown in figure 5.12. Displacement controlled

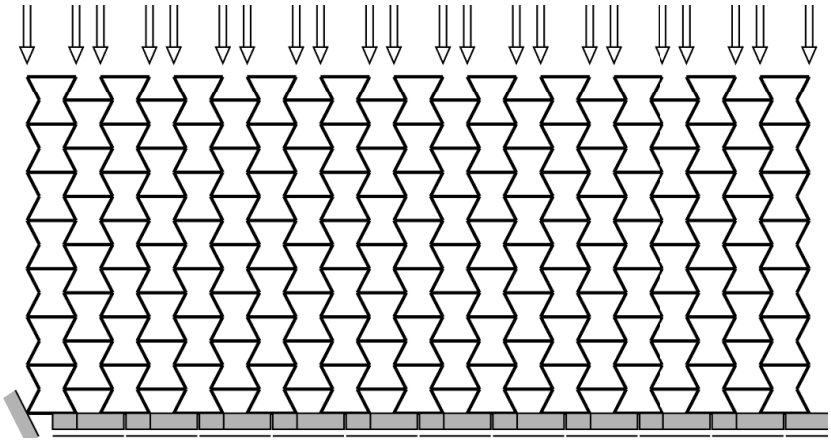

Figure 5.12: A re-entrant structure made from the connection of unit cells

loading is applied in ten load steps. The prescribed displacement is increased by 0.5 mm ($\varepsilon_{X1} = 0.08333$) in each load step. The bottom edge of the assembly is restrained in X1 direction and rotation θ_z. In addition, the left corner node is also restrained in the horizontal direction to avoid rigid body translation. All cell members are rigidly connected to each other. Each cell member is discretized into 8 elements. Preliminary analyses are run with 2, 4, 8 and 16 elements per cell member to select a suitable mesh size. The material properties and dimensions of the cell members are taken same as the previous analyses.

The deformed structure after the final load step is shown in figure 5.13. It can be seen in the figure that the structure does not just compress in the direction of loading, but also in the lateral direction, thus displaying the desired auxetic effect at the structural level.

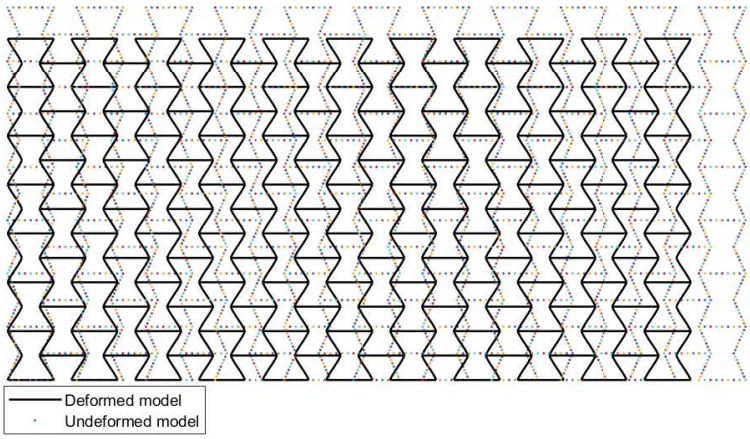

Figure 5.13: Deformed structure exhibiting the auxetic effect when loaded in X1 direction

The Poisson's ratio of the structure is obtained by finding the negative ratio of strain in horizontal direction to the strain in vertical direction at any point in the structure. Similarly, the effective Elastic modulus in loading direction is computed by dividing the stress obtained in the loaded points by the imposed strain. The stress at the loaded edge is calculated by dividing the sum of reaction forces obtained at the loaded nodes by the cross-sectional area of the edge (i.e. product of the length of the edge and the out of plane width, b). The computational results of the Poisson's ratio and the effective Young's modulus in X1 direction are shown in figure 5.14. The analytical results are also shown along with the computational results to show the comparison between them. For both effective mechanical properties, the analytical and computational results based on linear analysis (Computational results GNL - off) are close to each other. The relative difference between the analytical and the computational linear analysis results for Poisson's ratio ν_{12} and the effective Elastic modulus in X1 direction are only 0.06 %, and 4.68% respectively. Moreover, the result of the Poisson's ratio obtained at the structural level is found to be less than 0.5% different than the results of the Poisson's ratio obtained at a unit cell level. The results at both the level should have been same. The difference in results,

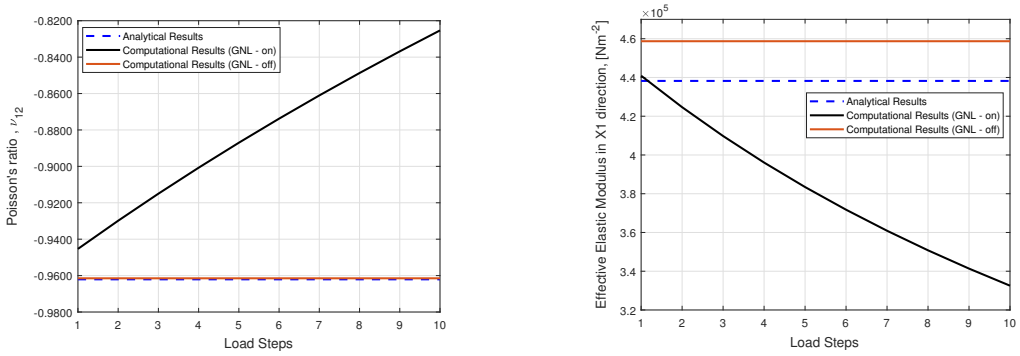

(a) Comparison of Poisson's ratio

(b) Comparison of effective elastic modulus

Figure 5.14: Comparison of analytical and computational results of mechanical properties of structure loaded in X1 direction

Table 5.2: Analytical and computational results (linear analyses) of effective Young's modulus in X1 direction

h/l	**1.5**			**2.0**			**2.5**			**3.0**		
θ	**CR** [Nm^{-2}]	**AR** [Nm^{-2}]	**E(%)**	**CR** [Nm^{-2}]	**AR** [Nm^{-2}]	**E(%)**	**CR** [Nm^{-2}]	**AR** [Nm^{-2}]	**E(%)**	**CR** [Nm^{-2}]	**AR** [Nm^{-2}]	**E(%)**
-15°	2100130.5	1997382.3	5.14	1501292.8	1423811.1	5.44	1168191.2	1106163.6	5.61	956063.2	904395.9	5.71
-30°	682732.6	657324.8	3.87	458710.9	438216.5	4.68	345382.4	328662.4	5.09	276957.5	262929.9	5.34
-45°	352017.0	344992.6	2.04	219337.1	211573.8	3.67	159296.2	152570.3	4.41	125062.0	119300.0	4.83
-60°	-	-	-	117481.6	114452.2	2.65	82416.9	79429.5	3.76	63472.4	60818.8	4.36
-75°	-	-	-	53328.4	52357.9	1.85	36453.1	35292.9	3.29	27690.6	26617.5	4.03

even of a small magnitude, should be due to the discretization problem. It is expected that for the same global dimensions of the assembled structure, if the number of unit cells along X1 and/or X2 direction is increased, the difference in results obtained from analyses at two different levels diminishes.

The effective mechanical properties of the structure when loaded in X1 direction including geometrical non-linearity is also shown in figure 5.14. As expected, the Poisson's ratio and effective Young's modulus of the structure do not remain constant at each load step when the geometrical non-linearity is included. The Poisson's ratio varies in the similar manner as observed and discussed in the unit cell analysis (figure 5.11). When the compressive load increases, the orientation of the unit cell arrangement changes and thus affects the mechanical properties which are dependent on the re-entrant angle θ. It was discussed previously based on figure 5.3 that the effective Elastic modulus decreases with the increase in a re-entrant angle. Similar trend can be noticed in the computational results of E_1 as well which is based on the updated geometry of the structure i.e. the inclusion of geometrical non-linearity. With the increase in the compressive load, the re-entrant angle increases and thus leads to the decreased effective Young's modulus in X1 direction.

Next, the comparative study is done by performing geometrical linear analysis of re-entrant structures modelled with varying geometrical parameters to observe the effect of geometrical dimensions in the effective Young's modulus of the structure. The aspect ratio h/l and a re-entrant angle are varied according to the variation for the unit cell analysis. The cell member material properties, number of unit cells in the assembly and the remaining geometrical parameters are kept constant in all analyses.

The model of the assembled structure which depends on the dimensions and numbers of micro-structure unit cell is created by a script programmed in MATLAB. Simply by changing the ratio h/l and θ, the structure to be considered can be modelled and used in the finite element analyses. The results of all analyses are listed in table 5.2. The index CR, AR and E (%) in the table mean computational results, Analytical results and relative error percentage respectively. It can be observed in table 5.2 that all results are within 6% error range. The variation of the effective Young's modulus with the aspect ratio h/l and angle θ for constant value of t/l is found to be as predicted by the analytical formula. The effective Young's modulus in X1 direction was found to be decreasing with the increase in the magnitude of re-entrant angle θ and the ratio h/l.

The comparison of the computational results obtained at the structural level and the analytical results based on a unit cell level showed that the numerical model was correctly able to implement the homogeneous effective mechanical properties. In addition, the results of the computational analyses including geometrical non-linearity provided a useful insight into the change of the effective mechanical properties during the deformation. The results showed that with the increase in the compressive deformation in X1 direction, the structure becomes less auxetic and less stiff.

5.1.2. LOADING IN X2

The unit cell is now loaded in the X2 direction. The analytical formula for the Poisson's ratio and effective Young's modulus in X2 direction are:

$$\nu_{21} = \left[\frac{(h/l + sin\theta)sin\theta}{cos^2\theta}\right]\left[\frac{1 + (1.4 + 1.5\nu_s)(t/l)^2}{1 + \left(2.4 + 1.5\nu_s + tan^2\theta + 2\frac{(h/l)}{cos^2\theta}\right)(t/l)^2}\right] \tag{5.4}$$

$$E_2 = \left[\frac{E_s t^3 (h/l + sin\theta)}{l^3 cos^3\theta}\right]\left[\frac{1}{1 + \left(2.4 + 1.5\nu_s + tan^2\theta + 2\frac{(h/l)}{cos^2\theta}\right)(t/l)^2}\right] \tag{5.5}$$

where symbols $E_s, \nu_s, t, h, l, \theta$ have the same meanings as discussed previously. These relations are also derived including the axial, shear and bending deformations in the cell members.

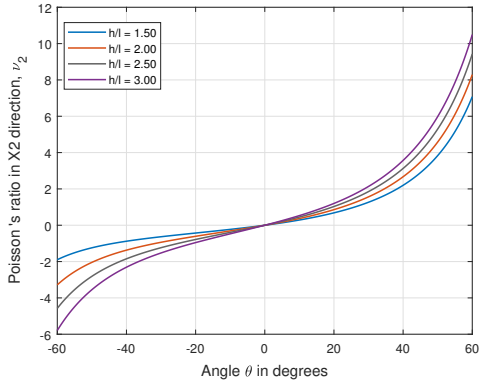

Figure 5.15: Variation of ν_{21} with respect to θ for different values of h/l

The variation of the Poisson's ratio ν_{21} with respect to θ for different values of h/l is shown in figure 5.15. The results are presented for the value of $t/l = 0.1$ and 0 Poisson's ratio of the cell wall material. As in previous case, it can be seen in the figure that for angles less than 0°, the Poisson's ratio is negative. Also, the magnitude of the Poisson's ratio is strongly dependent on the angle θ and the aspect ratio h/l. However, it is obvious that the Poisson's ratio exhibited by the unit cell when loaded in X1 direction is quite different than the one loaded in X2 direction. It means the unit cell is anisotropic in nature.

The absolute value of a Poisson's ratio exhibited by a re-entrant honeycomb unit cell in X2 direction increases with the aspect ratio h/l and the magnitude of the angle θ. It can be observed in figure 5.15 that for a given value of aspect ratio h/l, the Poisson's ratio increases with the increase in θ in conventional honeycomb, and also becomes more negative with the increase in the re-entrant angle. The variation of the ratio

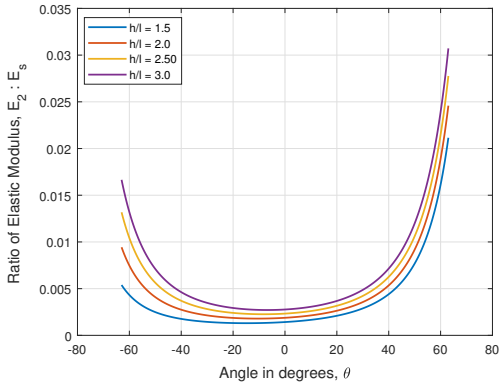

Figure 5.16: Variation of $E_2 : E_s$ with respect to θ for different values of h/l

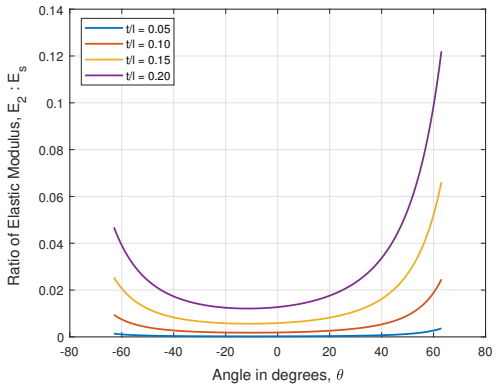

Figure 5.17: Variation of $E_2 : E_s$ with respect to θ for different values of t/l

of the effective elastic modulus in X2 direction and the elastic modulus of the cell wall material ($E_2 : E_s$) with respect to angle θ for different values of h/l is shown in figure 5.16. Like the results of the Poisson's ratio ν_{21}, the results of E_2 shown in figure 5.16 is also obtained for the value of $t/l = 0.1$ and 0 Poisson's ratio of the cell wall material.

It can be observed in figure 5.16 that, like the effective elastic modulus in X1 direction, the effective Young's modulus in X2 direction is also significantly smaller than the Young's modulus of the individual member which forms the cellular structure. However, the variation of the effective elastic modulus in two directions with angle θ and the aspect ratio (h/l) is different. The ratio of E_2 and E_s increases with the increase in the aspect ratio (h/l) and the magnitude of the angle θ in both conventional and re-entrant range. Besides its dependence on an angle θ and the ratio h/l, the effective Elastic modulus in X2 direction is also inversely proportional to cube of the cell member slenderness $(l/t)^3$. The variation of the ratio with respect to θ for a set of values of t/l, and a fixed value of $h/l = 2$ is shown in figure 5.17. The effective elastic modulus significantly increases with the decrease in the unit cell member slenderness.

The analytical results shown in figures 5.15 and 5.16 are now compared with the computational results. Number of cases are selected and analyzed to observe the effect of the aspect ratio h/l and a re-entrant angle θ on effective mechanical properties in X2 direction. The set of values of aspect ratio h/l and re-entrant angle θ used in these comparative studies are same as the ones adopted in the X1 loaded case.

ANALYSIS OF A UNIT CELL

A unit cell built from the cell wall material adopted in previous analyses is modelled using $h/l = 2$ and $\theta = -60°$. The unit cell modelled for examining the mechanical properties in X2 direction is shown in figure 5.18. The figure shows both the deformed and the undeformed model.

As seen in the figure, the horizontal ribs of length $0.5h$ are extruded from inner nodes on both sides of the unit cell. These extensions are used as loading and support points in the unit cell. As shown in the figure, the end of the left extension is restrained in both directions and rotation. A point load is applied in X2 direction for 10 load steps at the end of the right extension. The load increases by 0.2 N at each load step. The deformation behavior of the unit cell loaded in X2 was found to be similar to the one observed in a unit cell loaded in X1 direction. The primary deformation is due to the bending of the inclined ribs. When loaded with compressive force at the right end, the unit cell compresses in X1 direction as well. The remarkable feature is that for the

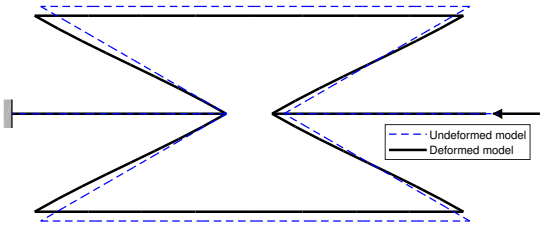

Figure 5.18: Deformation of a unit cell of re-entrant honeycomb loaded in X2 direction

selected case of the unit cell, the compression in X1 direction is more than the compression in the loaded direction. It means the Poisson's ratio more negative than -1 is observed. The Poisson's ratio is obtained at each load step, and is shown in figure 5.19(d). As the results presented are based on a geometrical linear analysis, the Poisson's ratio stays constant at each load step. The values of h/l, t/l and θ for the analyzed case of a unit cell are substituted in equation 5.4 and plotted along with the computational results in figure 5.19(d).

In addition, the normal force, shear force and bending moment developed in the members of the unit cell after the 10th load step are also shown in figure 5.19(a-c). The external load applied in X2 direction develops axial force in all members unlike the model loaded in X1 direction where normal force is developed only in the inclined ribs. The inclined members undergo bending deformation as predicted in the theory and observed in the previous model loaded in X1 direction. The bending moment diagram developed in the inclined members is shown in figure 5.19(c). The computational result of the Poisson's ratio exhibited by the unit cell complies with the theoretical prediction. The relative error between the analytical and computational results was found to be only 0.26 %.

The Poisson's ratio exhibited by the unit cell including geometrical non-linearity is shown in figure 5.20. It can be observed in figure 5.20 that the Poisson's ratio exhibited by the unit cell is no longer constant. Since the geometrical non-linearity is included, the Poisson ratio is now based on the updated geometrical configuration of the unit cell. It can be observed in figure 5.18 that when the right extended member is compressed, it causes bending in the inclined edge and top right corner moves downward. The angle between two ends of the inclined ribs now becomes more negative. This change continues to increase with the increase in the compressive load. As the Poisson's ratio is an angle dependent property, the Poisson's ratio also varies with the increasing load step. It was observed in figure 5.15 that the Poisson's ratio in X2 direction becomes more negative with the increase in re-entrant angle. Similar observation can be made in figure 5.20 as well.

Besides, another important observation is the difference in the Poisson's ratio exhibited by the unit cell when loaded in different directions. It can be noted from table 5.1 that the Poisson's ratio ν_{12} for the considered case of $h/l = 2$ and $\theta = -60$ was evaluated to be - 0.251 when the unit cell is loaded in X1 direction. However, for the unit cell made using the same geometrical dimensions and material properties exhibits Poisson's ratio of -3.273 when loaded in the perpendicular direction i.e. X2 direction. This highlights the anisotropic behavior of the unit cell. The mechanical properties are not only strongly dependent on the geometrical

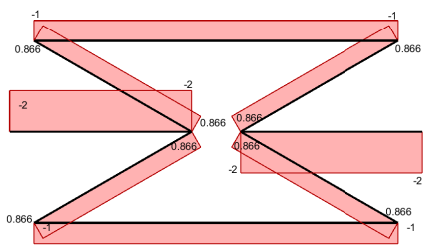

(a) Normal force diagram of unit cell

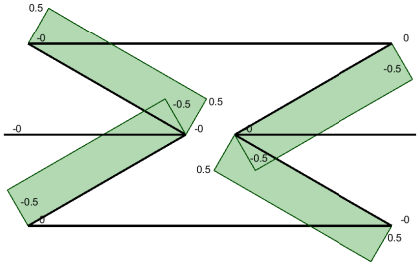

(b) Shear force diagram of unit cell

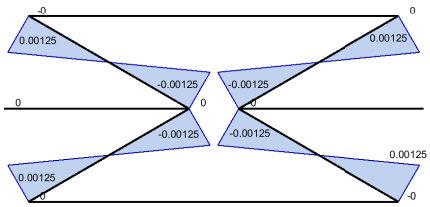

(c) Bending Moment diagram of unit cell

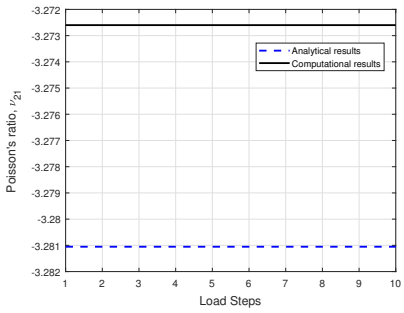

(d) Poisson's ratio ν_{21} when loaded in X2 direction

Figure 5.19: Poisson's ratio and Force, Moment Diagram in a unit cell loaded in X2 direction

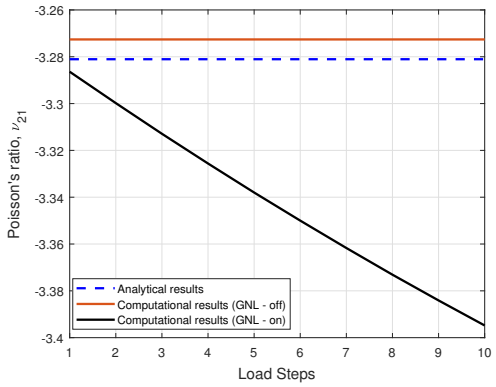

Figure 5.20: Comparison of analytical and computational results of Poisson's ratio exhibited by the unit cell when loaded in X2

Table 5.3: Analytical and computational results of Poisson's ratio ν_{21} for different values of h/l and θ

h/l	**1.5**			**2.0**			**2.5**			**3.0**		
θ	**CR**	**AR**	**E(%)**	**CR**	**AR**	**E(%)**	**CR**	**AR**	**E(%)**	**CR**	**AR**	**E(%)**
-15°	-0.330	-0.330	0.042	-0.459	-0.459	0.057	-0.584	-0.585	0.056	-0.708	-0.708	0.074
-30°	-0.633	-0.633	0.056	-0.938	-0.938	0.065	-1.235	-1.236	0.075	-1.525	-1.526	0.084
-45°	-1.039	-1.039	0.070	-1.663	-1.664	0.090	-2.265	-2.267	0.107	-2.846	-2.849	0.121
-60°	-	-	-	-3.273	-3.281	0.258	-4.568	-4.577	0.191	-5.780	-5.793	0.215
-75°	-	-	-	-8.532	-8.589	0.659	-11.691	-11.746	0.465	-14.372	-14.445	0.503

configuration and dimensions but also on the direction of the loading.

Now, to observe the effect of the geometrical dimensions and compare the computational results with the analytical predictions, 17 other unit cells modelled using a set of values of θ and h/l are analyzed. The results of the Poisson's ratio exhibited by these unit cells based on linear analyses are shown in table 5.3. The index CR, AR and E(%) in the table mean computational results, Analytical results and relative error percentage respectively.

It can be observed in table 5.3 that all results are within 0.6% relative difference. The results are in accordance with the theory that the re-entrant unit cell exhibits negative Poisson's ratio which can be tuned by modifying the geometrical parameters: aspect ratio h/l and the re-entrant angle θ. As suggested by the theory, the Poisson's ratio ν_{21} becomes more negative with the increase in a re-entrant angle θ and the aspect ratio (h/l). The results from the geometrical non-linear computational analyses showed that the auxeticity in a re-entrant unit cell can be increased with the increase in the compressive deformation. The magnitude of the lateral deformation is then also dependent on the amount of deformation the structure is subjected in the longitudinal direction. This feature can in-fact be useful to have a smart application device where the structure deforms laterally as per the requirement (i.e. the amount of external deformation it receives).

ANALYSIS OF ARRAYS OF UNIT CELL

The structural member formed by the connection of a number of arrays of unit cell is now loaded in X2 direction. As in the X1 direction loaded case, the effective mechanical properties of the structure are predicted

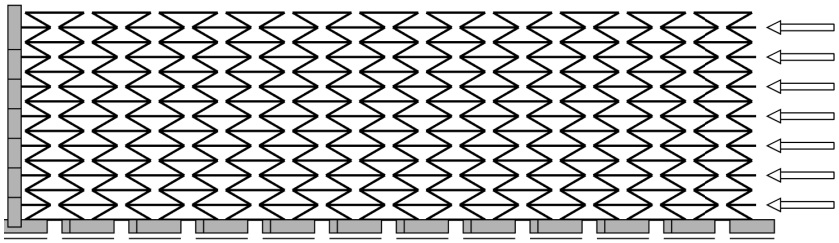

Figure 5.21: A re-entrant structure model for loading in X2 direction

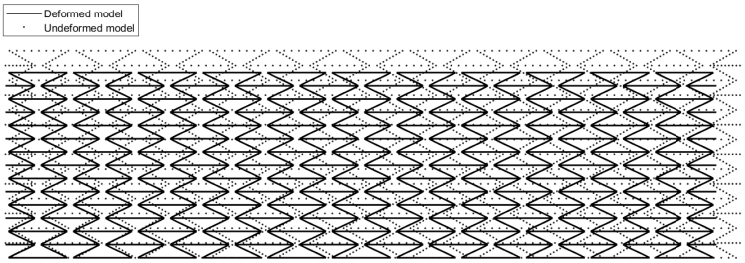

Figure 5.22: Deformed structure exhibiting the auxetic effect when loaded in X2 direction

based on the response of the unit cell used to model it. An assembled structure which is formed by the repetition of a unit cell with dimensions: $h = 10$ mm, $l = 5$ mm and $\theta = -60°$ in both X1 and X2 directions is shown in figure 5.21. The assembly of unit cells is loaded in X2 direction as shown in the figure. Displacement controlled loading is adopted with total ten load steps. The prescribed displacement is increased by 0.2 mm ($\varepsilon_{X2} = 0.0016$) in each load step. The bottom edge of the assembly is restrained in X1 direction and rotation θ_z. In addition, the left edge is restrained in the horizontal direction (X_2) and rotation θ_z. All cell members are rigidly connected to each other, and each member is discretized into 8 elements. The material properties and dimensions of the cell members are taken same as previous analyses i.e. $E_s = 2e8$ Nm^{-2}, $\nu_s = 0$, $t/l = 0.1$ and $b = 0.01$m. The deformed structure after the final load step is shown in figure 5.22. It can be noticed in the figure that the structure exhibits auxetic effect and the deformation in the lateral direction is more than the deformation in the direction of the application of the load.

The Poisson's ratio of the structure is obtained by finding the negative ratio of the strain in the vertical direction to the strain in horizontal direction at any point in the structure. Similarly, the effective Elastic modulus in loading direction is obtained by dividing the stress in the loaded points by the imposed strain. The stress at loaded edge is computed by dividing the sum of reaction forces obtained at the loaded nodes by the cross sectional area of the edge (i.e. product of the height of the edge and the out of the plane width, b). The computational results of the Poisson's ratio and the effective Young's modulus based on the linear analysis are shown in figure 5.23. In addition to the computational results of the linear analysis, the analytical results and computational results of the geometrical non-linear analysis are also shown to examine the comparison between them. For both effective mechanical properties, the analytical and computational results based on the geometrical linear analysis are close to each other. The relative differences between the analytical and the computational results (linear analysis) for the Poisson's ratio ν_{21} and the effective Elastic modulus in X2 direction are only 0.6 %, and 1.64% respectively.

The effective mechanical properties of the structure when loaded in X2 direction, and including geometrical non-linearity is also shown in figure 5.23. As expected, the Poisson's ratio and the effective Young's modulus of the structure do not remain constant at each load step when the geometrical non-linearity is included. The Poisson's ratio varies in the similar manner as observed and discussed in the unit cell analysis

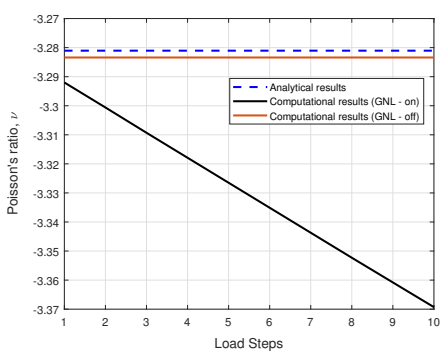

(a) Comparison of Poisson's ratio

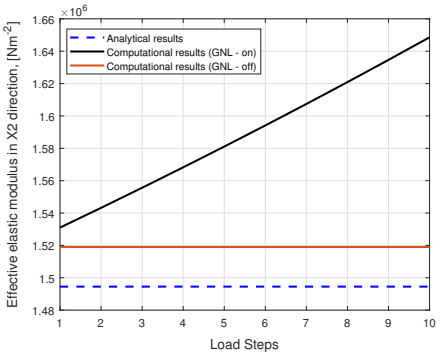

(b) Comparison of effective elastic modulus

Figure 5.23: Comparison of analytical and computational results of effective mechanical properties of structure loaded in X2 direction

Table 5.4: Analytical and computational results (linear analyses) of effective Young's modulus in X2 direction

h/l	**1.5**			**2.0**			**2.5**			**3.0**		
θ	**CR** [Nm^{-2}]	**AR** [Nm^{-2}]	**E(%)**	**CR** [Nm^{-2}]	**AR** [Nm^{-2}]	**E(%)**	**CR** [Nm^{-2}]	**AR** [Nm^{-2}]	**E(%)**	**CR** [Nm^{-2}]	**AR** [Nm^{-2}]	**E(%)**
-15°	264729.1	260622.2	1.58	367677.2	361941.3	1.58	468597.0	461246.2	1.59	567548.0	558596.5	1.60
-30°	293048.5	288494.8	1.58	434196.8	427403.0	1.59	571935.1	562925.3	1.60	706386.3	695183.9	1.61
-45°	416488.2	409989.2	1.59	667041.8	656526.8	1.60	908837.3	894368.2	1.62	1142328.3	1123965.6	1.63
-60°	-	-	-	1518993.4	1494529.9	1.64	2119579.0	2084816.1	1.67	2683388.2	2638608.5	1.70
-75°	-	-	-	6898017.8	6776089.4	1.80	9441198.0	9266682.6	1.88	11619469.0	11396124.3	1.96

(figure 5.20). When the compressive load increases, the orientation of the unit cell arrangement changes and thus, affects the mechanical properties which are dependent on the re-entrant angle θ. It was discussed previously based on figure 5.16 that the effective Elastic modulus increases with the increase in the re-entrant angle. Similar trend can be noticed in the computational results of E_2 as well which is based on the updated geometry of the structure. With the increase in the compression, the re-entrant angle increases and thus leads to the increased effective Young's modulus in X2 direction.

The results of the Poisson's ratio obtained from the computational analysis of a unit cell and the assembled structure are presented in figure 5.23(a) and figure 5.20. The comparison of two results show that the results obtained from the unit cell and the assembled structure are not identical. The difference in the results is expected to be arising from the discretization problem. The difference in the result should therefore diminish with the increase in the number of unit cells along X1 and/or X2 direction for the same structural size.

For the comparative study, additional analyses are performed by modifying the geometry to observe the effect of the geometrical dimensions in the effective Young's modulus. The aspect ratio h/l and re-entrant angle θ are varied as shown in table 5.3. The results of all analyses listed in table 5.4 do not include any form of non-linearity, and the index CR, AR and E(%) in the table mean computational results, Analytical results and relative error percentage respectively.

It can be observed in table 5.4 that all results are within 2% error range. The variation of the effective Young's modulus with the aspect ratio h/l and a re-entrant angle θ for the constant value of t/l is found to be in agreement with the analytical predictions. It can be observed that the effective elastic modulus in X2 direction increases with the increase in the aspect ratio h/l and re-entrant angle θ. The geometrical linear analyses of the assembled structure show that the homogeneous effective mechanical properties at structure level can be predicted using the analytical formulas which are based on the unit cell level. Moreover, the results of the geometrical non-linear analyses of assembled structure uncover the fact that the re-entrant honeycomb structure becomes more auxetic and more stiff with the increase in the compressive deformation in X2 direction. This property can be useful in the impact problem where it is advantageous to have high lateral deformations and stiffer structures with the increase in the longitudinal compression.

5.2. BI-AXIAL LOADING

The unit cell and the structure composed of unit cells were only loaded in one direction in previous sections. Now, the structure is loaded in two directions perpendicular to each other (X1 and X2 directions) at the same time. The response of the structure in bi-axial loading is in accordance to the response of the structure subjected to the individual uniaxial loading, and therefore can be assessed by the effective mechanical properties evaluated using equations 5.1, 5.2, 5.4 and 5.5. The close comparison of the results obtained from the computational model and the analytical predictions provides a groundwork to use the computational model to assess the bi-axial loading of the assembled structure.

The re-entrant honeycomb structure exhibited a strong anisotropic characteristics in the analyses of the uni-axial loading. Therefore, a linear elastic orthotropic compliance relation is considered in the computational analysis which is is given by:

$$\begin{bmatrix} \varepsilon_1 \\ \varepsilon_2 \\ \gamma_{12} \end{bmatrix} = \begin{bmatrix} \frac{1}{E_1} & \frac{-\nu_{21}}{E_2} & 0 \\ \frac{-\nu_{12}}{E_1} & \frac{1}{E_2} & 0 \\ 0 & 0 & \frac{1}{G_{12}} \end{bmatrix} \begin{bmatrix} \sigma_1 \\ \sigma_2 \\ \tau_{12} \end{bmatrix} \tag{5.6}$$

As the global behavior of the assembly can be defined by the effective mechanical properties of the structure, the compliance relation shown above can be used in the analysis of the cellular structure assembly as well. Due to the symmetry of the compliance matrix, the relation $\frac{-\nu_{21}}{E_2} = \frac{-\nu_{12}}{E_1}$ has to hold true. Using this

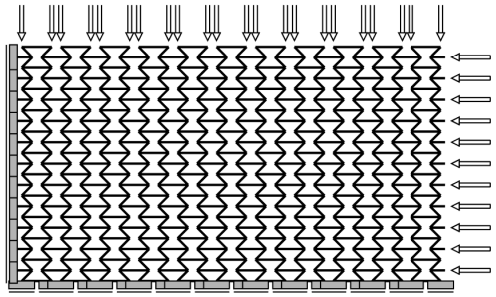

Figure 5.24: A model constructed by assembly of unit cells, and subjected to bi-axial loading

condition, the relation of elastic modulii E_1 and E_2 with stress and strain components can be defined by:

$$E_1 = \frac{\sigma_1 - \nu_{12}\sigma_2}{\varepsilon_1} \tag{5.7}$$

$$E_2 = \frac{\sigma_2 - \nu_{21}\sigma_1}{\varepsilon_2} \tag{5.8}$$

Therefore, the elastic modulii can be obtained when stress and strain state of a assembled structure is known. In order to obtain the values of elastic modulli from computational analysis, the model shown in figure 5.21 is now subjected to loading in X1 direction as well. The model for bi-axial loading is shown in figure 5.24.

In the model shown above, all connections between the cell members are rigid. The bottom edge of the assembly is restrained in the vertical direction and rotation θ_z. Similarly, the left edge is restrained in the horizontal direction and rotation θ_z. As shown above, the assembly of the unit cells is loaded at the right edge in X2 direction, and at the top edge in X1 direction. The compressive load is applied at both the edges. The displacement controlled loading is adopted with 10 load steps in total. The prescribed displacement increases by 0.1 mm in each load step in both the directions. The reaction force developed in the loaded node is obtained after every load step. The sum of the reaction forces is then divided by the corresponding area to obtain the stresses σ_1 and σ_2. The area for the top edge is the product of the length of the assembly and the out of the plane width of cell member. Similarly, the area for right edge is the product of the height of the assembly and the out of the plane width of the cell member. The Poisson's ratio ν_{12} and ν_{21} are obtained using equations 5.1 and 5.4 respectively. As the values of stress, strain and Poisson's ratio are known, they are substituted in equations 5.7 and 5.8 to obtain the computational results of the elastic modulii. These computed values are then checked with the analytical results of E_1 and E_2 obtained using equations 5.2 and 5.5 respectively.

Like in the previous loading cases, comparative study is done by analyzing the assembled structure formed by using different geometrical dimensions: h/l and θ. These parameters vary in the same range as listed in previous cases. The unit cell is formed by using the same cell wall material properties and slenderness ($l/t = 10$). The results of the comparative studies are shown in tables 5.5 and 5.6. The computational results are based on geometrical linear analysis, and are found to be close to the analytical results. The relative error difference was observed to be less than 3 %. The trend of the variation of elastic modulii with varying h/l and θ agrees with the analytical predictions and as observed in the loading in uniaxial directions. The effective elastic modulus in X1 direction decreases with the increase in h/l ratio and re-entrant angle θ, whereas the effective elastic modulus in X2 direction increases with the increase in h/l ratio and the re-entrant angle θ.

The results presented in tables 5.5 and 5.6 showed that the relative error in computing elastic modulus in X1 direction is lower at a lower magnitude of the re-entrant angle. Exactly opposite trend is observed in the

Table 5.5: Analytical and computational results of effective elastic modulus in X1 direction (E_1) for different values of h/l and θ

h/l	**1.5**			**2.0**			**2.5**			**3.0**		
θ	**CR** [Nm^{-2}]	**AR** [Nm^{-2}]	**E(%)**	**CR** [Nm^{-2}]	**AR** [Nm^{-2}]	**E(%)**	**CR** [Nm^{-2}]	**AR** [Nm^{-2}]	**E(%)**	**CR** [Nm^{-2}]	**AR** [Nm^{-2}]	**E(%)**
-15°	2008140.1	1997382.3	0.54	1431627.1	1423811.1	0.55	1112339.5	1106163.6	0.56	909522.8	904395.9	0.57
-30°	664445.0	657324.8	1.08	442969.8	438216.5	1.08	332232.0	328662.4	1.09	265789.4	262929.9	1.09
-45°	350347.6	344992.6	1.55	214858.8	211573.8	1.55	154939.7	152570.3	1.55	121153.0	119300.0	1.55
-60°	-	-	-	116928.9	114452.2	2.16	81162.6	79429.5	2.18	62152.6	60818.8	2.19
-75°	-	-	-	54144.9	52357.9	3.41	36511.2	35292.9	3.45	27539.8	26617.5	3.47

Table 5.6: Analytical and computational results of effective elastic modulus in X2 direction (E_2) for different values of h/l and θ

h/l	**1.5**			**2.0**			**2.5**			**3.0**		
θ	**CR** [Nm^{-2}]	**AR** [Nm^{-2}]	**E(%)**	**CR** [Nm^{-2}]	**AR** [Nm^{-2}]	**E(%)**	**CR** [Nm^{-2}]	**AR** [Nm^{-2}]	**E(%)**	**CR** [Nm^{-2}]	**AR** [Nm^{-2}]	**E(%)**
-15°	267236.3	260622.2	2.54	371796.5	361941.3	2.72	474570.6	461246.2	2.89	575568.3	558596.5	3.04
-30°	294959.2	288494.8	2.24	437276.9	427403.0	2.31	576234.6	562925.3	2.36	711921.2	695183.9	2.41
-45°	416293.2	409989.2	1.54	666612.5	656526.8	1.54	908099.0	894368.2	1.54	1141212.9	1123965.6	1.53
-60°	-	-	-	1507427.2	1494529.9	0.86	2102586.3	2084816.1	0.85	2660902.2	2638608.5	0.84
-75°	-	-	-	6798469.5	6776089.4	0.33	9296901.1	9266682.6	0.33	11433108.1	11396124.3	0.32

computation of the elastic modulus in X2 direction. When a re-entrant angle is of smaller magnitude, inclined ribs of the assembled structure are inclined towards the X1 direction. Whereas, higher magnitude of a re-entrant angle means the inclined ribs are more inclined towards the X2 direction. Therefore, the results from the biaxial loading indicate that the computational results seem to be closer to the analytical results when the contribution of the axial deformation is more dominant. Similarly, the results of the effective modulii obtained from the bi-axial loading and independent uni-axial loading were also found to be different with each other. The analytical predictions are based on the loading in either X1 or X2 direction. The interaction of the deformation mechanism when loaded at two directions at the same time might have resulted in the small magnitude of difference between the results of uni-axial loading and the bi-axial loading.

The results obtained from the computational analysis of the bi-axially loaded re-entrant honeycomb structure indicated that the continuum approach can be adopted to assess the global response of the assembled cellular model. This helps to extend the concept of a uni-axially loaded re-entrant honeycomb unit cell that exhibits an auxetic effect to a homogeneous continuum level possessing the great range of auxeticity.

5.3. SHEAR LOADING

The response of a re-entrant honeycomb structure subjected to shear loading is examined next. Evaluation of the effective elastic modulii and Poisson's ratios in two transverse directions have shown that a re-entrant cellular structure is orthotropic in nature. In orthotropic materials, nine elastic constants are required to form the compliance matrix relating stress and strain components. As two dimensional re-entrant cellular structure is taken in consideration, only 4 independent elastic constants are required to define a compliance matrix. Elastic modulii and Poisson's ratios in two transverse directions have already been determined previously. Those four constants are related to each other to satisfy the symmetry of the compliance matrix thus fulfilling three of the four independent elastic constants required to form the compliance matrix. The fourth independent constant is the effective shear modulus, G.

Gibson [4] studied the elastic deformation of a hexagonal honeycomb cells subjected to shear stress. The deformation mechanism of the shear loaded cells is shown in figure 2.17. The shearing deflection is found to be the result of the rotation at the connection between inclined and horizontal ribs, and bending of the horizontal ribs. The relation between the effective shear modulus, geometrical dimensions and cell member material properties was proposed to be:

$$G = \frac{E_s t^3 (h + l sin\theta)}{(hl)^2 cos\theta} \frac{1}{F} \tag{5.9}$$

$$F = 1 + 2(h/l) + (t/l)^2 \Big(\frac{1}{h/l}(2.4 + 1.5\nu_s)(2 + h/l + sin\theta) + \frac{h/l + sin\theta}{(h/l)^2}[(h/l + sin\theta) tan^2\theta + sin\theta] \Big) \tag{5.10}$$

where the symbols have the same meanings as described previously in section 5.1. This relation is also based on the inclusion of the axial and shear deformation of the cell members. Like other effective mechanical properties of the honeycomb structure, the effective shear modulus is also strongly dependent on the parameters: θ and h/l. The variation of the effective shear modulus with respect to an angle θ for different values of h/l is shown in figure 5.25. As in previous cases, the results for the variation of the effective shear modulus presented in figure 5.25 is based on $t/l = 0.1$ and 0 Poisson's ratio of the cell wall material.

It can be observed in figure 5.25 that the effective shear modulus decreases with the increase in the aspect ratio h/l. It is obvious in the figure that the effective shear modulus decreases with the decrease in an angle in a conventional honeycomb cell. This trend continues in the auxetic range too (i.e. in a re-entrant honeycomb cell). However, when the re-entrant angle is more negative than -60°, the effective shear modulus starts to increase.

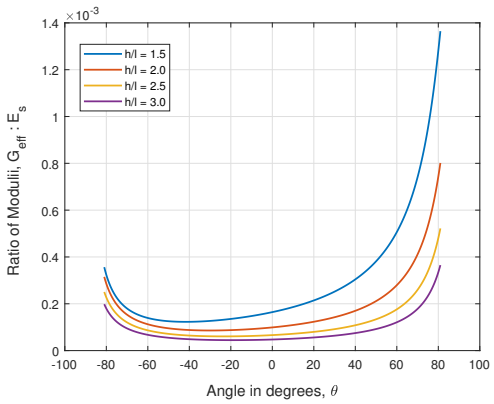

Figure 5.25: Variation of G with respect to θ for different values of h/l

Comparing figures 5.3, 5.16 and 5.25 it can be observed that the ratio of the effective shear modulus to the Young's modulus of base material is significantly smaller than the ratio of other two effective elastic modulii. The variation of the effective shear modulus with angle θ for different values of cell member slenderness is shown in figure 5.26. As expected, the effective shear modulus increases with the increase in the ratio t/l.

The re-entrant honeycomb cell loaded in shear will now be analyzed using finite element analysis. First, a representative study is performed in a unit cell level and then on the assembled structure. The aspect ratio h/l and a re-entrant angle θ are varied and its effect on the computational results of the effective shear modulus is examined.

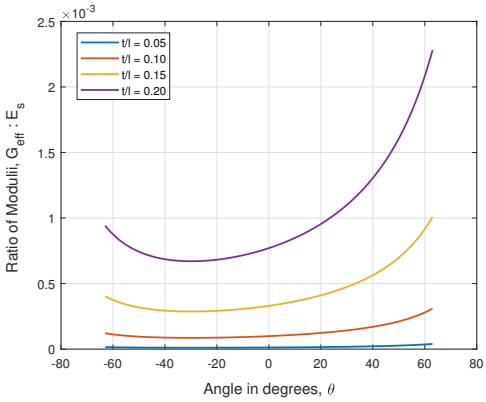

Figure 5.26: Variation of G with respect to θ for different values of t/l

Box 5.3.1: Re-entrant Cell Loaded in shear

Re-entrant honeycomb cells are modelled using following cell wall material properties and geometrical dimensions: $E_s = 2e8$ Nm^{-2}, $\nu_s = 0, b = 0.01$ m and $t/l = 0.1$. The aspect ratio h/l and an angle θ are varied between [1.5, 2.0, 2.5, 3.0] and [-15°, -30°, -45°, -60°, -75°] respectively. However, as mentioned earlier, the aspect ratio $h/l = 1.5$ is omitted with $\theta = -60°$ and $-75°$.

The finite element type and integration points used in the analysis are same as discussed in box 5.1.1. Each cell member is discretized into 8 elements. The model of the re-entrant cells and its deformed state when loaded in shear is shown in figure 5.27.

All connections of the cell members are restrained in horizontal direction in the re-entrant honeycomb finite element model. The cell members are free to rotate and deform in the vertical direction. As in the model loaded in X2 direction, the horizontal ribs are extended outward from the connection of inclined ribs. These extensions are used as loading and support points. The vertical load is applied at the end of the right extension as shown in figure 5.27. The end of the left extension is restrained in both horizontal and vertical directions but is free to rotate. It can be observed in figure 5.27 that the horizontal ribs bend in the shear loading problem unlike the models loaded in X1 or X2 direction. The

shearing deflection mechanism observed in the computational analysis is similar to the analytical deformation mechanism.

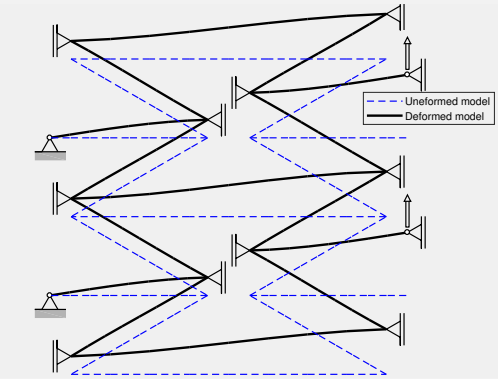

Figure 5.27: Re-entrant unit cell deformed due to shear loading

The displacement controlled loading method was adopted in the analysis. Ten load steps were applied in total with the vertical displacement increasing by 0.2 mm ($\gamma = 0.02$) at each load step. The reaction force developed at the loaded nodes is obtained at the end of the analyses, and these are used to calculate the shear stress. The ratio of shear stress and imposed shear strain results in the computational estimation of the effective shear modulus of the re-entrant honeycomb cell. The analytical prediction of the effective shear modulus for analyzed honeycomb was 2.25 x 10^4 Nm^{-2}, whereas the computational result based on linear analysis was observed to be 2.58 x 10^4 Nm^{-2}. The relative error in the present analysis was found to be approximately 14 %. However, the relative error in the computational analysis of the assembled structure formed by the connection of a number of re-entrant unit cells was found to be of smaller magnitude.

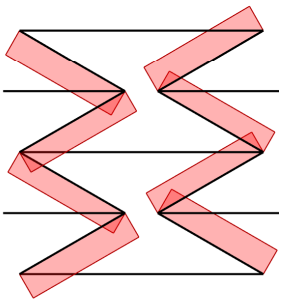

(a) Normal force diagram in a unit cell

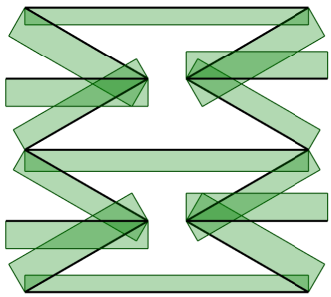

(b) Shear force diagram in a unit cell

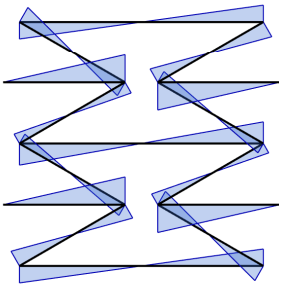

(c) Bending Moment diagram in a unit cell

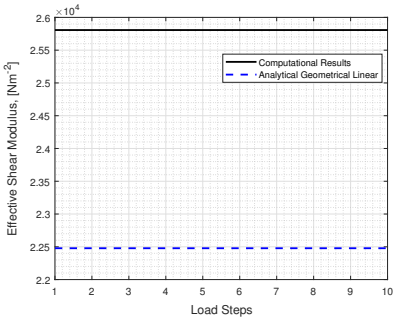

(d) Effective shear modulus of the unit cell

Figure 5.28: Effective shear modulus, and Force, Moment Diagram in a unit cell loaded in shear

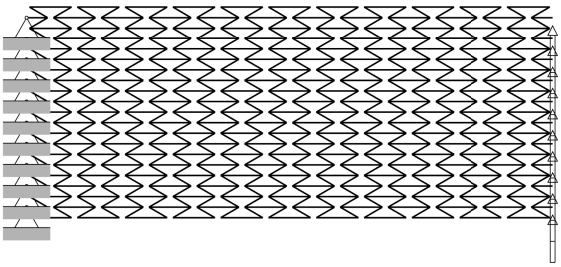

Figure 5.29: A re-entrant structure model for loading in shear

The normal force diagram, shear force diagram and bending moment diagram of the re-entrant honeycomb cell loaded in shear is shown in figure 5.28. It can be observed that no normal force is developed on the horizontal cell members which is an expected result as there is no axial deformation in those members of the unit cell. The bending moment diagram obtained from the computational analysis is also found to be similar to the one presented by Gibson [4]. The comparison of the computational and analytical results of the effective shear modulus is also shown in the figure.

The computational study is now performed on the structure formed by the connection of a number of unit cells. A structural member formed by the connection of array of unit cells is shown in figure 5.29. The assembly is formed from unit cells with $h/l = 2$ and a re-entrant angle $\theta = -60°$. All connections in the assembly is restrained in horizontal direction. It is to be noted that the horizontal restraints are not indicated in the figure. The right edge is loaded with vertical displacement incremented by 0.2 mm ($\gamma = 0.0042$) at each load step. The deformed structure at the end of the tenth load step is shown in figure 5.30. The comparison of the computational and analytical results of the effective shear modulus of the structure is shown in figure 5.31. Comparing the results shown in figure 5.31 and figure 5.28(d), it can be noticed that the error between the computational and analytical results is reduced to approximately 4 % in the assembled structure. With the increase in the number of unit cells, the global behavior of the computational model can be predicted by the analytical solution of a unit cell.

The comparative study is done for the assembled structure loaded in shear as well. The unit cell dimensions that form the structure are varied between the set of values listed in box 5.3.1. Other properties including the number of unit cells forming the structure is kept constant in all analyses. The results are used to compare the computational results with the analytical predictions shown in figure 5.25. The computational results along with the analytical predictions are listed in table 5.7. The index CR, AR and E(%) in the table mean computational results, Analytical results and relative error percentage respectively.

It can be observed in table 5.7 that all results are within 5 % error range thus indicating the validation of the finite element model. The variation of the effective shear modulus with the aspect ratio h/l and re-entrant angle θ for constant value of t/l is found to be as predicted by the analytical relations. The effective shear modulus decreases with the increase in h/l ratio for a constant re-entrant angle. However, the variation of effective shear modulus with the re-entrant angle for a constant h/l ratio is not so straightforward. The variation depends on the value of h/l ratio as well. It can also be observed in figure 5.25 that the effective shear modulus starts to increase with the increase in the re-entrant angle only after a certain limit. The limit is dependent on the aspect ratio h/l. The effective shear modulus continues to decrease upto -30° and then starts increasing for $h/l = 2.0$ and 2.5. However, the turning point limit for $h/l = 3.0$ is already observed at $\theta = -15°$.

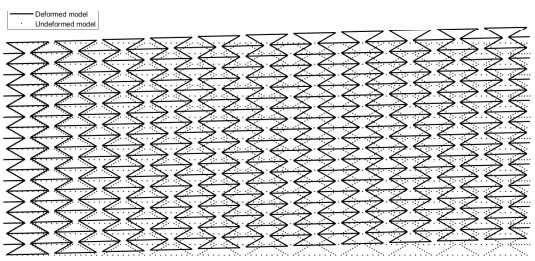

Figure 5.30: Deformed model after the application of shear deformation

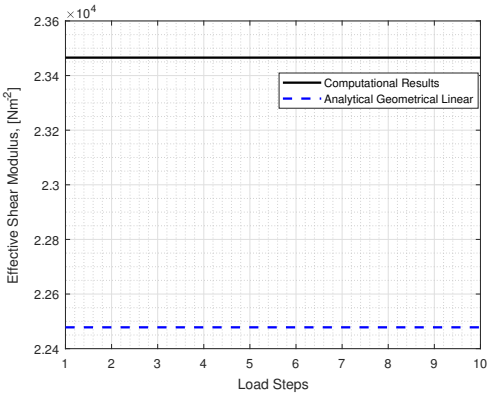

Figure 5.31: Comparison of analytical and computational results of effective shear modulus of the re-entrant honeycomb structure

Table 5.7: Analytical and computational results of effective shear modulus for different values of h/l and θ

h/l	**1.5**			**2.0**			**2.5**			**3.0**		
θ	**CR** [Nm^{-2}]	**AR** [Nm^{-2}]	**E(%)**	**CR** [Nm^{-2}]	**AR** [Nm^{-2}]	**E(%)**	**CR** [Nm^{-2}]	**AR** [Nm^{-2}]	**E(%)**	**CR** [Nm^{-2}]	**AR** [Nm^{-2}]	**E(%)**
-15°	29348.6	28195.8	4.09	18670.0	17867.7	4.49	12876.7	12291.9	4.76	9404.6	8960.8	4.95
-30°	26382.9	25360.4	4.03	17941.6	17176.2	4.46	12816.7	12237.4	4.73	9566.1	9116.2	4.94
-45°	25622.1	24641.1	3.98	18936.3	18134.1	4.42	14067.3	13434.3	4.71	10741.5	10238.0	4.92
-60°	-	-	-	23465.7	22478.1	4.39	18108.9	17298.1	4.69	14119.5	13460.2	4.90
-75°	-	-	-	41101.9	39393.0	4.34	32619.4	31175.3	4.63	25810.7	24618.4	4.84

The consistent and close results obtained from the computational analyses and the analytical predictions of the shear loaded re-entrant honeycomb structure mean all effective mechanical properties required to define a compliance matrix can be accurately estimated using the computational model. This presents the possibility to assess the assembled cellular structure subjected to bending and compare the results with the equivalent continuum model.

5.4. RE-ENTRANT STRUCTURE SUBJECTED TO BENDING

After examining the response of a re-entrant structure subjected to uniaxial, bi-axial and shear loading, now the assembly of the re-entrant structure is subjected to bending. Comparison of the computational and analytical results when analyzing the response of a re-entrant honeycomb structure subjected to various loading conditions has shown the possibility to use the continuum approach to study the global response of the re-entrant structure. The response of the assembly of re-entrant honeycomb unit cells subjected to bending is obtained by the finite element analysis of the cellular structure. Simultaneously, a continuum model with same global dimensions and effective mechanical properties of the re-entrant structure is also analyzed. The results obtained from the computational analysis of these two different models are compared to observe if it is possible to approximate the re-entrant structure model with a homogeneous continuum model.

Box 5.4.1: Re-entrant structure subjected to bending

An assembly of re-entrant honeycomb unit cells is modelled by connecting a number of unit cells in both X1 and X2 directions. The re-entrant unit cells are modelled with following geometrical and mechanical properties: $h = 0.01$ m, $E_s = 2e8$ Nm^{-2}, and $b = 0.01$ m. The re-entrant angle θ and the aspect ratio h/l are varied between $[-15°, -30°, -45°, -60°, -75°]$ and [1.5, 2.0, 2.5, 3.0] respectively. The finite element type and integration points used in the analyses are the same as discussed in box 5.1.1. The assembly of re-entrant structure consists of 7 rows and 41 columns of re-entrant honeycomb unit cells. Each cell member in a unit cell is discretized into 8 elements. The structural model formed from an assembly of unit cells with $h/l = 2$ and $\theta = -45°$ is shown in figure 5.32.
As it can be seen in the figure, the corners of the third unit cell at the bottom edge from both right and left edges are restrained in the vertical direction. In addition, the horizontal displacement is also restrained in one of the two unit cells to avoid the rigid body motion. The ends of the 21^{st} unit cell at the top edge is subjected to a compressive point load equal to 0.2 N(each) in X1 direction. The loading and boundary conditions used in the model shown in figure 5.32 is the representation of a

three point bending problem in an equivalent continuum model. The deformed shape of the model after an analysis is shown in figure 5.33.

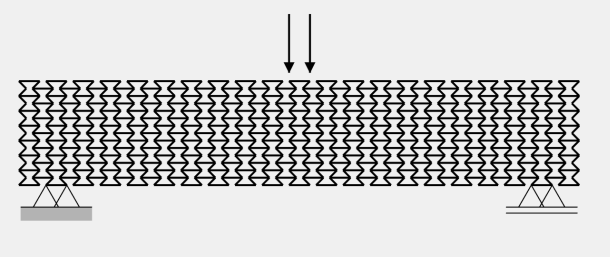

Figure 5.32: Re-entrant structure subjected to bending

Now, the problem is modelled from the continuum approach as well. A beam of length, height and thickness equal to the assembled cellular structure is modelled with the effective mechanical properties of the re-entrant honeycomb unit cell. The effective mechanical properties can be analytically calculated using the formulas presented in previous sections, or can also be extracted from the results of computational analyses of re-entrant structures. It has already been noted in earlier sections that the re-entrant honeycomb structure is orthotropic in nature. Therefore, the continuum model is also modelled as an orthotropic material. The stiffness matrix to be used in the continuum analysis is the inverse of the compliance matrix presented in equation 5.6. The continuum beam is modelled using six noded triangular element with six integration points.
The response to the loading is assessed by obtaining the deflection of the midpoint of the bottom edge of both the continuum and the cellular structure models. The results are then compared to observe if the behavior of the re-entrant honeycomb cellular structure can indeed be estimated by using the continuum approach with same global dimensions and effective mechanical properties.

As a comparative study, the analyses of cellular structure and the equivalent continuum model are repeated for re-entrant structure modelled by varying h/l and θ in the range listed in box 5.4.1. The remaining mechanical properties and geometrical dimensions including the number of unit cells is kept constant. The results of the comparative study are presented in table 5.8. The indexes MS, C and E(%) in table 5.8 represent the results of micro-structure model, continuum model and the relative error percentage respectively. It was found that the results from the cellular structure model and an equivalent continuum model were in good agreement for $\theta = -15°, -30°, -45°$ and $-60°$. The difference between the results from two different models was found to be less than 5%. However, when the cell members are more inclined i.e. at $\theta = -75°$, the difference between the results of two models was found to be increasing. Nevertheless, all results were found to be within 10 % difference. Thus, the results indicate that the global response of the assembly of re-entrant honeycomb structure can be reasonably assessed using the continuum approach.

The results presented above showed the comparison of adopting continuum approach to model the cellular structure. The obtained results however can not be used to assess the effect of an individual parameter in the structure. As different parameters such as the overall dimensions of the structure, the global position of the loading and support points, and effective mechanical properties of the structure are varied in each case, assessing the effect of only one parameter based on these results will be difficult. Therefore, two additional analyses were performed for the case of $\theta = -45°$ and $h/l = 2$ by varying the number of unit cells along the X1

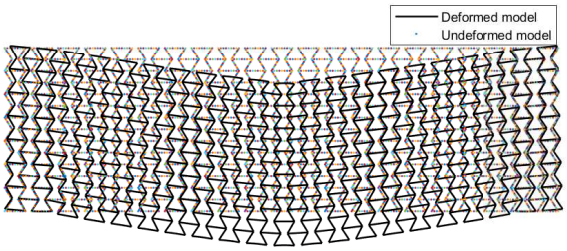

Figure 5.33: Deformed re-entrant structure subjected to bending

Table 5.8: Comparison of results of the bending problem from the continuum approach (C) and the micro-structure approach (MS)

h/l	**1.5**			**2.0**			**2.5**			**3.0**		
θ	**MS** [m]	**C** [m]	**E**(%)	**MS** [m]	**C** [m]	**E**(%)	**MS** [m]	**C** [m]	**E**(%)	**MS** [m]	**C** [m]	**E**(%)
-15°	-0.00297	-0.00302	1.60	-0.00609	-0.00615	0.97	-0.01068	-0.01073	0.52	-0.01696	-0.01701	0.24
-30°	-0.00258	-0.00264	2.53	-0.00560	-0.00569	1.70	-0.01007	-0.01022	1.47	-0.01623	-0.01647	1.42
-45°	-0.00223	-0.00234	4.76	-0.00513	-0.00529	2.98	-0.00954	-0.00978	2.43	-0.01565	-0.01602	2.31
-60°	-	-	-	-0.00484	-0.00509	4.83	-0.00927	-0.00965	3.92	-0.01550	-0.01609	3.68
-75°	-	-	-	-0.00506	-0.00551	8.28	-0.01011	-0.01093	7.49	-0.01744	-0.01885	7.47

direction. These additional analyses will provide an insight into the effect of slenderness in the deformation response of the auxetic orthotropic beam. The additional analyses included 8 and 9 unit cells along the X1 direction as compared to 7 unit cells as shown in figure 5.32. The external load is applied at two ends of the cell at the middle of the top edge. Other parameters like the number of unit cells in X2 direction, the support point, the magnitude of load, cell member material properties etc. are kept constant in these two additional models.

The deflection of the beam mid-span at the bottom edge of the structure with 8 cells and 9 cells along the height were computed to be 0.00408 m and 0.00338 m respectively. The deflection of the beam mid-span is observed to be decreasing with the increase in the height of the structure. As the remaining parameters are constant, the decrease in the deflection is the result of the decrease in the beam slenderness. The results from the continuum approach are found to be in accordance with the results from cellular model. The relative difference between a continuum model and the cellular model results are computed to be 2.74 % and 2.62 %.

5.5. SUMMARY OF STATIC ANALYSIS OF MICRO-STRUCTURE

The goal of this chapter was to focus mainly on the second research question presented in section 1.2. The model of a honeycomb cellular structure used in this research was proposed by Gibson et al. [4] in which all the cell members of a unit cell are assumed to be rigidly connected to each other. The analytical and computational results presented in this chapter have highlighted the possibility of achieving a negative Poisson's ratio in a honeycomb structure built with a re-entrant angle between the inclined and the horizontal ribs. The primary deformation of a unit cell loaded in either directions was the bending of the inclined ribs. However, the contribution of an axial and shear deformation was also significant especially for less slender cell members and the values of a re-entrant angle close to 0° and -90°.

The Poisson's ratio exhibited by a re-entrant honeycomb structure can be easily modified by varying the geometrical parameters. Results presented in figures 5.2, 5.15 and tables 5.1 and 5.3 displayed the strong dependence of a Poisson's ratio on two geometrical parameters, i.e. the aspect ratio of a unit cell h/l and the angle of connection between cell members θ. Thus, it indicates the possibility of achieving the desired value of Poisson's ratio by simply modifying the parameters h/l and θ in a unit cell. The results of Poisson's ratio presented in tables 5.1 and 5.3 showed that it is possible to obtain Poisson's ratio more negative than -1 for certain values of aspect ratio h/l and a re-entrant angle θ. This particular feature can be used to design a displacement amplifier where it is useful to have the large lateral deformation for a small longitudinal deformation.

The computational results of the effective Poisson's ratios exhibited by a unit cell loaded in either directions were always found to be less than 1% different than the analytical predictions. Such a close comparison between the computational analyses and the analytical predictions mean the finite element code used in the unit cell analysis can be adopted to analyze the honeycomb cellular model with the inclusion of geometrical non-linearity and extend the study of re-entrant honeycomb to the structural level and other loading conditions like bi-axial loading and bending.

The computational analyses of a cellular model at structural level highlighted the fact that the effective elastic modulii and Poisson's ratios exhibited by the structure in either directions are equal to the analytical predictions based on a unit cell analysis. The relative difference between the computational results and the analytical predictions of the effective modulii were always found to be less than 6%. The magnitude of error reduces with the increase in the number of unit cells for the same structural size. The results from analyses of assembled structure have showed that the computational model was able to reproduce the homogeneous effective mechanical properties at the structural level. In addition, the consistent and close results also provided a basis to extend the computational investigation to the comparison of an assembled discrete model with its equivalent continuum model.

The computational and analytical study of a re-entrant honeycomb structure at the unit cell level and the structural level revealed that a re-entrant honeycomb structure is orthotropic in nature. The effective mechanical properties exhibited by a re-entrant honeycomb structure were not only dependent on the geometrical parameters, but also on the direction of the loading. For instance, a unit cell designed with $\theta = -45°$ and $h/l = 2$ exhibited Poisson's ratio equal to -0.536 when loaded in X1 direction and Poisson's ratio equal to -1.66 when loaded in X2 direction.

The geometrical nonlinear analyses of a unit cell and an assembled cellular structure provided insights into the change of the effective mechanical properties of a re-entrant honeycomb structure during the deformation. The results indicated that with the increase in the compressive deformation in X1 direction, a re-entrant honeycomb structure becomes less auxetic and less stiff. Exactly opposite behavior was observed in a re-entrant structure loaded with the increasing compressive deformation in X2 direction. The structure was found to be exhibiting stiffer and higher auxetic behavior with the increase in the compressive deformation in X2 direction. This finding not only indicate the orthotropic nature of auxetic structures but also gives information necessary to consider while loading a re-entrant honeycomb structure. The results inferred that it is important to be cautious when a re-entrant honeycomb structure is loaded in compression in X1 direction as the structure becomes less stiff with the increasing compressive deformation. However, the geometrical nonlinear response demonstrated by a re-entrant structure loaded in compression in X2 direction can be utilized to alleviate the effect of the impact load. As the structure in such a loading scenario becomes more auxetic and stiffer, its resistance against the impact increases making it a promising structure in the defense application.

After obtaining the consistent and accurate results of the effective mechanical properties from the computational analyses of a re-entrant honeycomb structure at a unit cell level and structural level, the study was then shifted to the bi-axially loaded assembled structure and bending of the assembled structure. These analyses aimed to provide a link between the computational analysis of a cellular structure and an equivalent continuum model. The comparison of results obtained from two models demonstrated the possibility of assessing the global behavior of a cellular structure using the homogeneous continuum approach. The results from a cellular model and an equivalent continuum model for both the loading cases (bi-axially loaded and bending) were less than 6% different from each other which is expected to decrease further with the increase in the number of unit cells used in the analyses.

The effective in-plane elastic modulii and the effective density of a re-entrant honeycomb structure were found to be reduced by the order of 2 to 3 compared to its cell member base properties. The reduction in the effective elastic modulii is considered to be one of the serious constraints in the design and practical use of auxetic cellular structures. However, the flexibility, light weight and the great range of auxeticity it is capable of exhibiting have demonstrated its promising use in applications that need high deformations under targeted loads.

6

MICRO-STRUCTURE - DYNAMIC ANALYSIS

The effect of the geometrical parameters on the static response of a negative Poisson's ratio exhibiting re-entrant honeycomb unit cell and the assembled cellular structure was investigated using computational analyses in the previous chapter. The response of a re-entrant honeycomb structure to dynamic loading, and the effect of the geometrical parameters on its dynamic response are examined in this chapter. The characteristics of the wave propagation in a re-entrant unit cell, the estimation of wave velocities and their relationship with the geometrical parameters are discussed in detail. The study however does not cover other important aspects of dynamic analysis like the energy absorption during the propagation of vibration, structural response of a unit cell and assembled cellular structure etc.

A re-entrant honeycomb unit cell is formed by six cell members. These cell members are connected to each other with a re-entrant angle, and thus, forms a kink. During the propagation of an elastic wave in a unit cell, the wave passes at each of these kinks, and wave reflection-transmission process takes place. Along with the reflection transmission process, the characteristics of propagating wave changes as well. The incident wave, irrespective of its nature (longitudinal or shear wave) generates both longitudinal and shear wave at the kinks by reflection transmission phenomenon. These transmitted and reflected waves propagate along the cell member before encountering next kink where the reflection, transmission and mode conversion of waves take place again.

The wave propagation in a unit cell and its behavior when passing at the connections of cell members is investigated first. Later, the wave speed in cellular structure is determined as well. The global behavior of the cellular structure is considered in estimating the shear wave velocity and the longitudinal wave velocities in X1 direction and X2 direction independently. The effective mechanical properties and effective density of

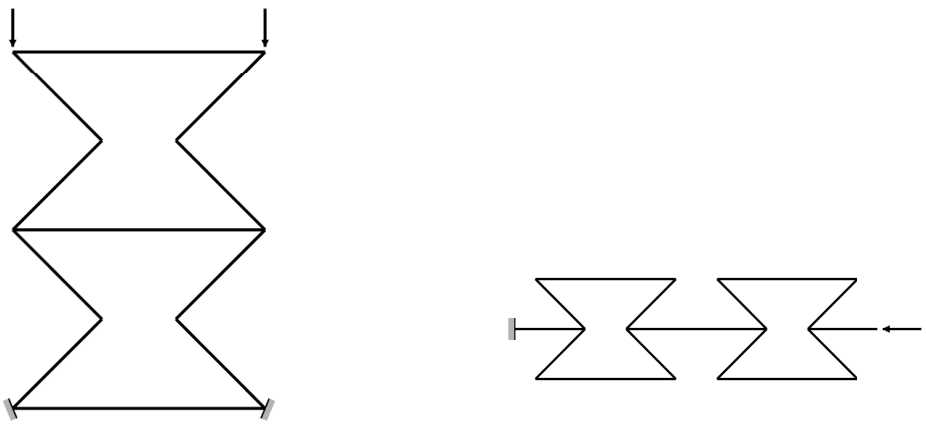

(a) (b)

Figure 6.1: Models used for examining wave propagation in unit cell when loaded in (a) X1 direction (b) X2 direction

unit cells analyzed in previous section are used for the estimation of wave velocities.

6.1. WAVE PROPAGATION IN UNIT CELL

The propagation characteristics in a unit cell is examined when loaded uniaxially either in X1 or X2 direction. The wavelength of the external load is smaller than the unit cell length. When the re-entrant honeycomb structure is loaded, it generates wave which propagates along the cell member undisturbed until it reaches the connection of two cell members. At the connection, the reflection-transmission process takes place along with the generation of new waves. Since a lot of processes take place simultaneously, the analysis and observation are done by considering one cell member at a time. Two unit cells along the X1 direction and X2 direction are modeled to examine the wave propagation characteristics in a unit cell when loaded in X1 direction and X2 direction respectively. The models used for examining the wave propagation in different loading directions are shown in figure 6.1. The dynamic analysis is performed to observe the propagation of longitudinal and shear stress waves in the structure. The reflection, transmission and the mode conversion process is observed at the connection of the cell members.

Box 6.1.1: Wave Propagation in Unit Cell

The re-entrant honeycomb unit cell is modeled using horizontal beam of length 0.01 m and rectangular cross-section. The aspect ratio (h/l) and slenderness of the cell members is taken to be $h/l = 2$, and $t/l = 0.1$. The out of plane width of the beam is used as 0.01 m and the material properties chosen for the cell members are: E_s = 2e8 Nm^{-2}, $\nu_s = 0$ and ρ = 1 kgm^{-3}. The re-entrant angle is adopted as $\theta = -45°$ for both loading cases.
The cell members are rigidly connected to each other in both the models. Each cell member is divided into 100 elements to clearly observe the wave propagation phenomenon within the unit cell. The loading and support conditions are shown in figure 6.1. In a model loaded in X1 direction, the corner nodes at the bottom edge are completely restrained, and the corner nodes at the top edge are subjected to an external compressive load. The model loaded in X2 direction has two horizontal members of length equal to $0.5h$ extended outward from the end cells. The ends of these extended members are used as loading and support points. The external load is applied as a trapezoidal pulse load in both analyses. The (compressive)load has a rise time of 10 time steps to reach a value of 10 N, then stays constant at 10 N for the next 10 time steps and then linearly decreases to 0 N again in 10 time steps. The time step is chosen to be 2e-9 s, and the dynamic analysis is performed for 1000 time steps when loaded in X1 direction, and 2000 time steps when loaded in X2 direction.
The applied loading generates longitudinal wave in the horizontal beam of the unit cell loaded in X2 direction. This wave propagates along the horizontal beam, and encounters the connection of three beams at the end of the horizontal beam. The characteristics of the wave when it reaches the connection, and after it passes the connection is studied. Similarly, when the unit cell is loaded in X1 direction, the configuration of the structure is such that it generates both longitudinal and shear wave at the loaded point. The waves propagate along the horizontal and inclined beams connected to the loading nodes. The characteristics of these waves when they pass the connection at the other ends are examined.

LOADED IN X1 DIRECTION

First, the wave propagation characteristics in a unit cell loaded in X1 direction is examined. The top two corner nodes are loaded in X1 direction with the loading described in box 6.1.1. The external force generates longitudinal and shear waves in both cell members connected to the loaded points. The generated waves then start to propagate along the cell member with their respective wave speed. The longitudinal and shear stresses developed along the cell member at different stages are observed to study the wave propagation characteristics. As the longitudinal wave speed is larger than the shear wave speed, the longitudinal stress wave is observed to be propagating faster than the shear stress wave in both cell members. The longitudinal wave velocity and shear wave velocity are measured to be approximately 14000 ms^{-1} and 10000 ms^{-1} respectively. The computed wave velocities are in agreement with the analytical wave speed predicted by $\sqrt{\frac{E_s}{\rho_s}}$ and $\sqrt{\frac{E_s}{2\rho_s(1+\nu_s)}}$ respectively for the given values of E_s, ρ_s and ν_s.

As the horizontal cell member connects two loaded points, the waves in the horizontal member travel towards each other. The waves traveling towards each other from two ends meet at the mid point of the

beam and continue propagating towards their respective ends, the superposition of waves occurs. First, the longitudinal wave reaches the kink at the other end, where longitudinal and shear waves are both transmitted and reflected due to the geometrical discontinuity created by the kink. The transmitted and reflected waves now superpose with the already present waves of their corresponding type and continue to propagate along the cell members. Similar phenomenon occurs when the shear wave propagating along the horizontal cell member reaches the kink as well. The shear wave when passes the kink also generates both longitudinal and shear waves which are reflected and transmitted at the kink. In this entire process of reflection, transmission, mode conversion and superposition, the longitudinal wave is always found to be propagating faster than the shear wave as expected.

The loaded points are the connection of the horizontal and inclined cell members. Therefore, the external force introduces both longitudinal and shear waves in the inclined cell members as well. The waves in these members continue to propagate undisturbed until they reach the connection of two inclined cell members. At the connection of two inclined cell members, again the process of reflection and transmission of the waves takes place. When the longitudinal wave in the inclined member reaches the connection, longitudinal and shear waves are reflected and transmitted at the connection. As upto this moment, waves have not yet reached the lower inclined cell member, the transmitted waves generated from the longitudinal wave at the connection propagate undisturbed in the lower inclined cell member. However, the reflected waves superpose with the already present waves of corresponding type and propagate along the upper inclined member of the top cell. Later, when the incident shear wave also reaches the connection, the reflection-transmission process takes place again. The reflected and transmitted waves superpose with the present waves of similar type in the member and propagate in their respective directions. Finally, when the waves in the bottom inclined beam reach the connection of two unit cells, there are three possible paths for the wave: transmission to the upper inclined beam of bottom cell, transmission to the horizontal beam or reflection to the lower inclined beam of the top cell. Therefore, the entire process of reflection, transmission and superposition of wave take place all over again. The wave propagation in a cellular structure is hence the continuous process of reflection, transmission, mode conversion and superposition of waves. The reflection transmission process occurs only at the connection. Therefore, the process can be controlled by modifying a parameter at the connection i.e., the re-entrant angle θ.

First, the unit cell that is modelled using a re-entrant angle, $\theta = -45°$ is considered. The reflection transmission process occurring at the connection of two inclined cell members is discussed here. As explained before, the external force induces both longitudinal and shear wave in the inclined member. These wave propagate along the inclined member. In a longitudinal wave, the direction of vibration is along the direction of propagation i.e. along the axis of the inclined member. Whereas, in a shear wave, the direction of vibration is perpendicular to the direction of propagation i.e. perpendicular to the axis of the inclined member. When the longitudinal wave in the upper inclined member of the top cell modelled with angle $\theta = -45°$ reaches the connection, almost the whole longitudinal wave is transmitted as a shear wave to the lower inclined member. The angle between the upper and lower inclined member in a unit cell modelled with $\theta = -45°$ is a right-angle i.e. 90°. Also, since the angle between the direction of vibration for longitudinal and shear wave is a right-angle, the incoming longitudinal wave in upper inclined member now propagates as a shear wave in the lower inclined member. Similarly, later when the incident shear wave reaches the connection, almost the whole shear wave is now transmitted as the longitudinal wave in the lower inclined member. A small part of the incident wave is still reflected due to the rotation constraint applied at the connection point.

As the longitudinal wave that reached the connection earlier is transmitted as a shear wave, and the shear wave that reached the connection later is transmitted as a longitudinal wave, the shear wave stays ahead of the longitudinal wave in the inclined beam member. However, as a longitudinal wave travels faster, it finally catches up the shear wave in the inclined member at the end. Both the longitudinal and shear wave reach the connection of three cell members at the same time. The waves at this connection then have three paths to be transmitted and/or reflected. Therefore, the complete conversion of the longitudinal and shear waves to each other do not occur at this connection of a re-entrant honeycomb cell irrespective of the re-entrant angle used.

However, the special feature of a shear wave being ahead of the longitudinal wave in an inclined member can only be observed with the re-entrant angle $\theta = -45°$. When the re-entrant angle is not equal to $-45°$, the angle between the inclined members is no longer a right-angle and thus the complete mode conversion does not take place. At such re-entrant unit cells, when the incident wave reaches the connection, the transmission of both longitudinal and shear wave takes place. As both waves are generated at the same time, the longitudinal wave travels faster in the new segment, and the shear wave follows it.

The process of the wave propagation in unit cell loaded in X1 direction is shown in figure 6.2 and figure 6.3. The longitudinal stress and shear stress are marked as red and blue respectively. The model in figure 6.2 is modelled with $\theta = -45°$, and the models in figure 6.3 are modelled with θ equal to $-30°$ and $-60°$. The four

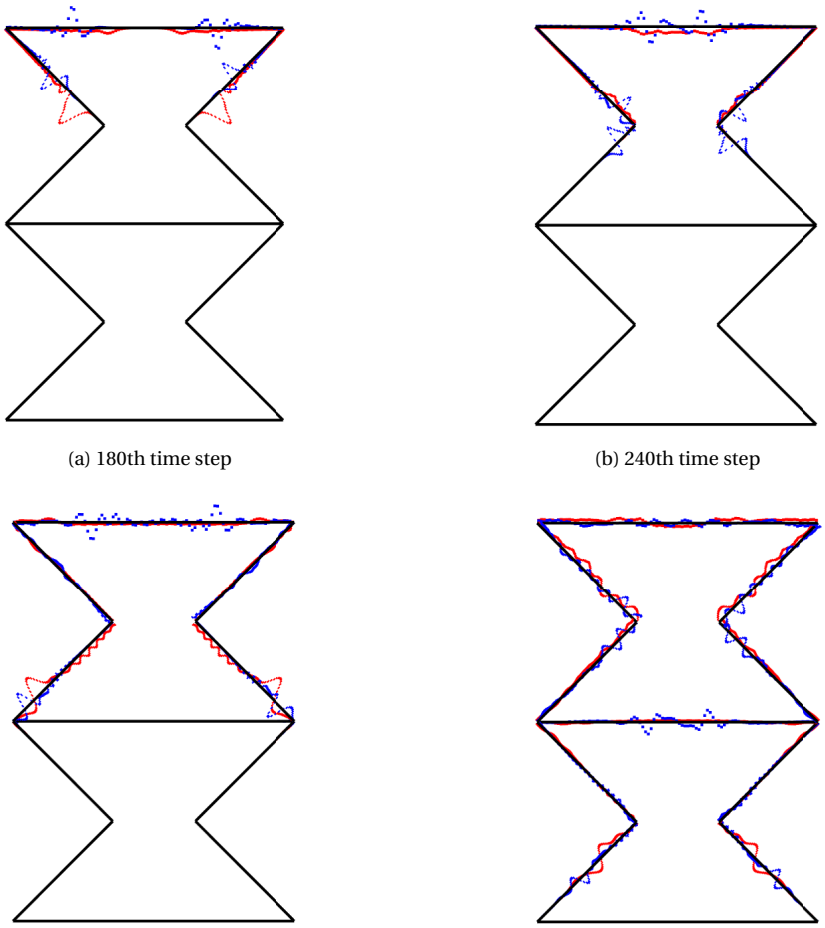

(a) 180th time step

(b) 240th time step

(c) 420th time step

(d) 800th time step

Figure 6.2: Wave propagation in a re-entrant structure ($\theta = -45°$) loaded in X1 direction at different time steps

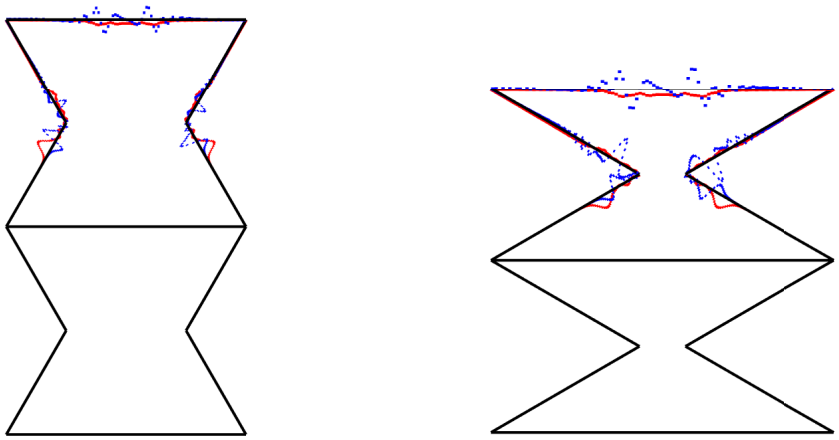

(a)

(b)

Figure 6.3: Wave propagation in a re-entrant structure loaded in X1 direction at 240th time step with (a) $\theta = -30°$ (b) $\theta = -60°$

sub-figures in figure 6.2 show the wave propagation stages in the 180th, 240th, 420th and 800th time steps. These time steps are selected to represent the wave propagation characteristics discussed above. In subfigure 6.2(a), it can be seen that the longitudinal and shear wave are propagating away from the loaded node in both horizontal and inclined member. The longitudinal wave is observed to be ahead of the shear wave as expected. In sub-figure 6.2(b), the longitudinal wave in the upper inclined member has already crossed the connection, and has been transmitted as shear wave in the lower inclined member. It can be seen that there is no longitudinal wave yet in the lower inclined member, because the incident shear wave has just reached the connection. In sub-figure 6.2(c), it can be observed that the incident shear wave that was transmitted as the longitudinal wave in lower inclined member propagates faster and finally catches up with the shear wave in the lower inclined member. The process of complete mode conversion also occurs at the connection of inclined members of bottom cell. It can be seen in sub-figure 6.2(d) that the mode conversion has taken place at this connection as well, and therefore the longitudinal wave is following the shear wave in the lower inclined member of the bottom cell. However, as observed in sub-figure 6.2(c), the longitudinal wave catches up, and both waves reach the end at the same time.

The two sub-figures in figure 6.3 show the wave propagation stage at 240th time step in re-entrant structure modelled with θ equals to $-30°$ and $-60°$. The results support the discussion presented above that the complete mode conversion takes place only when $\theta = -45°$. At this time step, the incident shear wave has only reached the connection of two inclined members at the top cell. However, both longitudinal and shear wave is observed to be propagating in the lower inclined member. This implies the incident longitudinal wave was transmitted as longitudinal and shear wave when it passes at the connection node.

LOADED IN X2 DIRECTION

The wave propagation characteristics in the model shown in figure 6.1(b) is analyzed next. As it is evident from the figure, the load is applied in X2 direction at the end of the member extended outward in X2 direction from the connection of two inclined beams. The compressive load described in box 6.1.1 is used as an external load. The modelling technique and parameters, material properties and geometrical dimensions adopted in the analysis have already been discussed in box 6.1.1. The external force generates a longitudinal compressive stress in the horizontal cell member. The incident longitudinal wave then starts to propagate along the cell member and passes the first connection of three cell members. When the wave passes the kink, the reflection transmission process of longitudinal and shear waves takes place.

As a result of the geometrical discontinuity created due to kink, the incident longitudinal wave splits into longitudinal and shear wave, and are transmitted to two connected inclined cell members. As expected, the longitudinal wave propagates faster than the shear wave generated at the same point. Same material properties were used in the present analysis as before. Therefore, the wave speed of the longitudinal wave and shear wave is measured to be same as obtained in the previous analysis.

When the incident longitudinal wave encounters the kink, though longitudinal and shear waves are transmitted to the inclined cell members, only longitudinal wave is reflected to the horizontal cell member. This occurs due to the geometrical configuration. As the incident wave passes at the connection, the incident compressive longitudinal stress is transmitted as tensile longitudinal stress, but shear stress of different sign to the inclined members. As a result, only the longitudinal wave is reflected to the horizontal member to maintain equilibrium at the connection node. The reflected longitudinal wave superpose with the present longitudinal wave in the member and propagate towards the loaded edge. The wave reflects from the loaded end and the whole phenomenon is repeated. It is a continuous process.

The longitudinal and shear waves transmitted to the inclined cell members continue to propagate along the member. The longitudinal wave reaches earlier to the connection of the inclined cell member and the horizontal member. As both the upper and lower inclined cell members are of equal length, the wave reaches the connection at the top and bottom edges at the same time. When the connection is encountered, the reflection-transmission process of the longitudinal and shear waves take place again. The reflected longitudinal and shear waves superpose with the present wave of similar type and propagate towards the other end. The transmitted longitudinal and shear wave start to propagate along the horizontal cell members towards their respective end. As a wave had not yet reached to these members, the propagation of transmitted longitudinal and shear wave can be clearly observed at these members. Although the shear wave has not yet reached the connection of inclined cell member and horizontal member, the shear wave generated due to longitudinal wave passing the connection is found to be already propagating in the horizontal member. Later, when the shear wave reaches the connection of the horizontal and inclined cell members, the reflection transmission process of the longitudinal and shear waves take place again. These new waves then superpose with

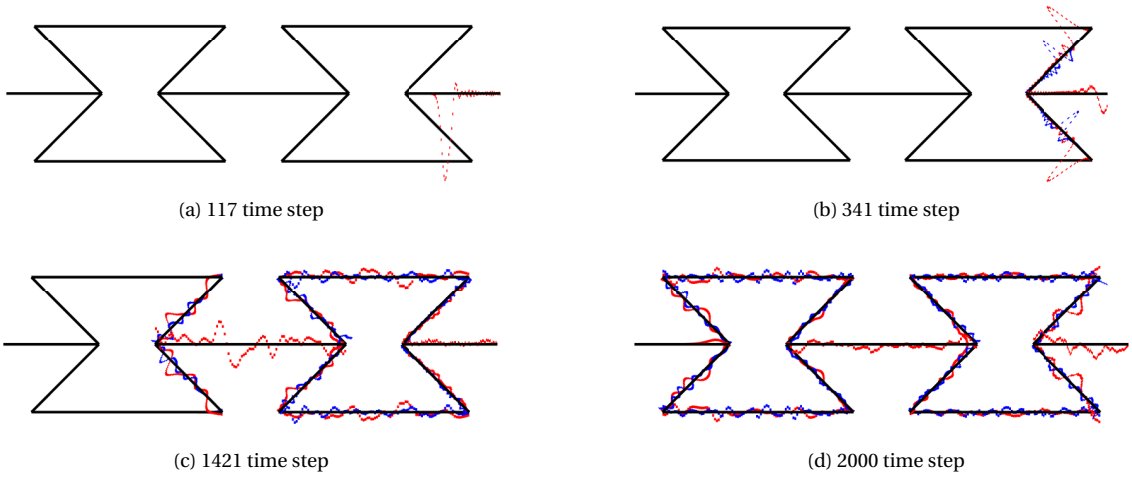

(a) 117 time step (b) 341 time step

(c) 1421 time step (d) 2000 time step

Figure 6.4: Wave propagation in a re-entrant structure ($\theta = -45°$) loaded in X2 direction at different time steps

already present waves and propagate in their respective directions. This way the incident longitudinal wave undergoes number of reflection, transmission, mode conversion and superposition before it finally reaches the support. As all these processes take place in the connection of the members, the proportion of the mode conversion and reflection transmission process is affected by the re-entrant angle θ. However, the characteristics and features of the process described above do not change with the re-entrant angle θ.

The wave propagation phenomenon examined in a re-entrant structure modelled with $\theta = -45°$, and loaded in X2 direction is shown in figure 6.4. The longitudinal stress and shear stress are marked as red and blue respectively. The four sub-figures in figure 6.4 show the wave propagation stages in the 117th, 341st, 1421st and 2000th time steps. These time steps highlight different stages of the wave propagation characteristics discussed above. In subfigure 6.4(a), it can be noted that the incident compressive longitudinal wave is propagating in the horizontal cell member. When the longitudinal wave passes the connection it was approaching, the transmission of the longitudinal and shear wave to the inclined cell member takes place. Similarly, a part of the longitudinal wave is also reflected to the horizontal cell member. This stage is shown in the sub-figure 6.4(b). It is also evident in the figure that the transmitted longitudinal wave propagates faster than the shear wave in the inclined cell member. The process of reflection-transmission, mode conversion and superposition continue taking place which can be seen in subfigures 6.4(c) and 6.4(d).

6.2. LONGITUDINAL WAVE PROBLEM

After examining the wave propagation characteristics in a unit cell, now the speed of the wave propagation in re-entrant structures is investigated. The prospective use of re-entrant structures for shock mitigation problems makes it essential to understand the speed of elastic wave propagation in re-entrant structures. An assembly of re-entrant cells formed by connecting number of unit cells along X1 and X2 direction are modelled to measure the speed of longitudinal wave propagation in X1 and X2 direction respectively. The continuum approach of determining the elastic wave speed is used to estimate the longitudinal wave velocity in re-entrant structures. The effective mechanical properties of re-entrant structures with varying geometrical parameters have already been computed with sufficient accuracy and consistency in Section 5. These effective mechanical properties are used along with the continuum approximation to estimate the wave velocity. Besides, the results of dynamic analysis of the assembly of re-entrant unit cells when loaded in X1 direction and X2 direction are used to compare the results of computational analysis and continuum approximation.

6.2.1. LOADING IN X1

The longitudinal wave speed in a re-entrant structure in X1 direction is determined using the results of computational analysis of re-entrant honeycomb structure modelled by connecting several unit cells in X1 direction. The honeycomb structure is loaded in X1 direction, and the dynamic analysis is performed by using finite element method. The results of the numerical studies are compared with the wave velocity obtained by using continuum approximation. The continuum approximation of longitudinal wave velocity in X1 direction

is obtained by using following relation:

$$c_{l,X1} = \sqrt{\frac{E_1}{\rho^\star}} \tag{6.1}$$

where E_1 and $\rho^\star$ are the effective elastic modulus in X1 direction and effective density of a re-entrant unit cell respectively. The expressions of E_1 and $\rho^\star$ are shown in equations 5.2 and 2.21 respectively. As the effective density and elastic modulus in X1 direction are dependent on geometrical parameters of the unit cell, the longitudinal speed in X1 direction in a re-entrant structure is also dependent on the geometrical parameters: $t/l, h/l$ and θ of a re-entrant honeycomb structure. Besides the geometrical parameters, it is also dependent on the material properties of the cell member i.e. the Elastic modulus (E_s), density (ρ) and Poisson's ratio (ν_s) of the cell member material. As the continuum estimation of the longitudinal wave velocity depends on various geometrical parameters, a graph is plotted to examine the variation of wave velocity in X1 direction with respect to the angle θ for different values of h/l. The result presented in figure 6.5 is based on $t/l = 0.1$, $E_s = 2\text{e}8$ Nm^{-2}, $\nu_s = 0$ and $\rho = 1$ kgm^{-3}.

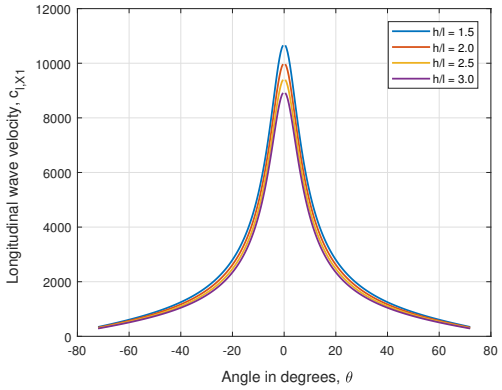

Figure 6.5: Variation of continuum estimation of $c_{l,X1}$ with respect to θ for different values of h/l

It can be observed in figure 6.5 that the longitudinal wave velocity in X1 direction is strongly dependent on an angle θ and the aspect ratio h/l. The effect of re-entrant angle is more significant than the aspect ratio h/l. It can be noted from the figure that the longitudinal wave velocity in X1 direction in a honeycomb structure is not affected due to the auxeticity. The longitudinal wave velocity in X1 direction in a conventional honeycomb modelled with angle θ is the same as in a re-entrant honeycomb modelled with angle -θ. Like the effective elastic modulus in X1 direction, the longitudinal wave velocity in X1 direction also decreases with the increase in the magnitude of an angle θ and the aspect ratio h/l. The result shown in figure 6.5 is now compared with the computational results to validate the continuum approach of estimating the wave velocity in re-entrant cellular structures.

Box 6.2.1: Longitudinal Wave Velocity in Re-entrant Structures

A re-entrant honeycomb structure is formed by connecting 40 unit cells in X1 direction. The single row of 40 unit cells in X1 direction is loaded in X1 direction at one end and restrained at the other end. The unit cells are modelled using following cell wall material properties and geometrical dimensions: $E_s = 2e8$ Nm^{-2}, $\nu_s = 0, \rho = 1$ kgm^{-3}, $b = 0.01$ m and $t/l = 0.1$. The ratio h/l and angle θ are varied between [1.5, 2.0, 2.5, 3.0] and [-15°, -30°, -45°, -60°, -75°] respectively, omitting the combination of $h/l = 1.5$ with $\theta = -60°$ and $-75°$. A model of the re-entrant structure with $h/l = 2$ and $\theta = -45°$ is shown in figure 6.6

The finite element type, integration points and modelling techniques adopted in the analysis are the same as discussed in box 5.1.1. Each cell member is discretized into 8 elements, and all members are rigidly connected to each other. At the restrained end of the assembly, all three degrees of freedoms (u_{X1}, u_{X2}, θ_z) are restrained at one corner node and only two degrees of freedom (u_{X1}, θ_z) are restrained at the other corner. Similarly, at the loaded end, both corner nodes are subjected to a compressive external load in X1 direction. The trapezoidal load is used as an external load. The load has a rise time of 5 time steps to a value of 10 N, then stays constant at 10 N for five time steps and then decreases to 0 N again in five time steps. The time step used in the analysis is 0.4 μs. Implicit time

step method is used for the dynamic analysis with parameters $\beta = 0.25$ and $\gamma = 0.5$. The analysis is performed for 2000 time steps.

Figure 6.6: Model of re-entrant structure to estimate the longitudinal wave velocity in X1 direction

The displacement of the connection of two inclined members are studied at various time steps to estimate the wave velocity in X1 direction. The difference between the time when the displacement in the direction of loading is maximum at two extreme inner nodes i.e. the one closest to the loaded end and the one closest to the restrained end is noted to estimate the velocity of the wave propagation in X1 direction. The distance between these two points is then divided by the time difference which results in the computational estimation of the longitudinal wave velocity in X1 direction. To support this estimation, the difference between the time when displacement is maximum at other points which are away from the ends of the structure is also calculated. These time differences also result in the approximately same velocity, thus providing a consistency in the estimation.
The computational result obtained from this procedure is then compared with the continuum approach estimation. As a comparative study, the analyses are performed for 18 different re-entrant structures modelled using a set of values of h/l and θ specified above.

The analysis is first performed for a re-entrant structure modelled with $h/l = 2$ and $\theta = -45°$. The displacement (u_{X1}) - time graph of two extreme inner nodes described in box 6.2.1 is shown in figure 6.7. The cells are numbered 1 to 40, starting from the restrained end to the loaded end. Since the two inner nodes are the connection of two inclined members in extreme cells, they are numbered 1 and 40. The difference between the time when the displacement in X1 direction is maximum at these two nodes is 252 μs. As the distance between nodes in X1 direction is 0.2758 m, the wave velocity in X1 direction is estimated to be 1094.44 ms^{-1}. The consistency of measuring the wave velocity using this method is checked by repeating the process for other nodes as well. The displacement time graph of nodes in the 6th and 35th cells, the 9th and 32nd cells, the 15th and 26th cells, and the 18th and 23rd cells are also shown in figure 6.8. The difference between the time when the displacement was maximum at those sets of points was found to be 187.6 μs, 148.4 μs, 71.2 μs and 32.4 μs respectively. This results in the wave speed in X1 direction to be 1093.1 ms^{-1}, 1095.9 ms^{-1}, 1092.4 ms^{-1} and 1091.2 ms^{-1}. The effective modulus in X1 direction and the effective density of the re-entrant structure for the adopted values of geometrical dimensions and material properties are 211573.757 Nm^{-2} and 0.2188 kgm^{-3} respectively. For these values of effective elastic modulus and density, the continuum approach estimation of the longitudinal wave velocity in X1 direction is 983.4216 ms^{-1}. The continuum approach estimation is found to be 10% lower than the results obtained from the finite element simulations.

Next, the re-entrant structure is modified by varying the re-entrant angle θ and the ratio h/l in a specified set of values listed in box 6.2.1. The finite element modelling technique and parameters, material properties and remaining geometrical parameters are kept the same. The wave velocity in X1 direction is estimated by observing the displacement time profile of two inner nodes, and the consistency of results are checked by comparing the results with other set of points too. The results of finite element analysis and the continuum approach for all 18 analyzed cases are shown in table 6.1. The index MS, C and E (%) in the table mean results from computational analysis of micro-structure, results from the continuum approach and the relative difference between the results respectively.

The results obtained from the computational analysis were found to follow the trend of the continuum approach results in terms of their variation with respect to the re-entrant angle θ and the aspect ratio h/l. The wave velocity decreases with the increase in the re-entrant angle and the ratio h/l. However, the difference between the computational and continuum approach estimation of the wave velocity in X1 direction is computed to be around 10%. Two more analyses were performed with two rows of 80 elements along the length. The length of the horizontal ribs was adjusted to have the same structural size. The analyses with increased number of unit cells were performed for $h/l = 2$, $\theta = -30°$ and $h/l = 3$, $\theta = -60°$. The computational results of the longitudinal wave speed in X1 direction for these two additional cases were computed to be only 4.14% and 5.62% different than the results from continuum approach.

The results presented in table 6.1 showed that the results from computational and continuum approach

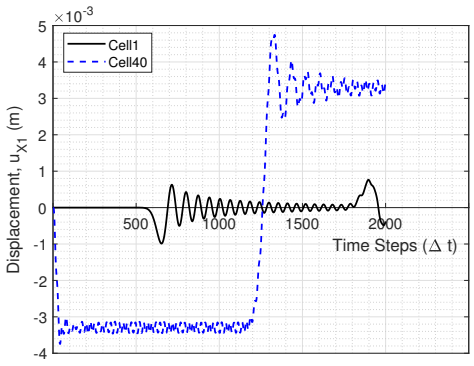

Figure 6.7: Displacement time graph of two nodes in 1st and 40th cell to estimate the wave velocity in X1 direction

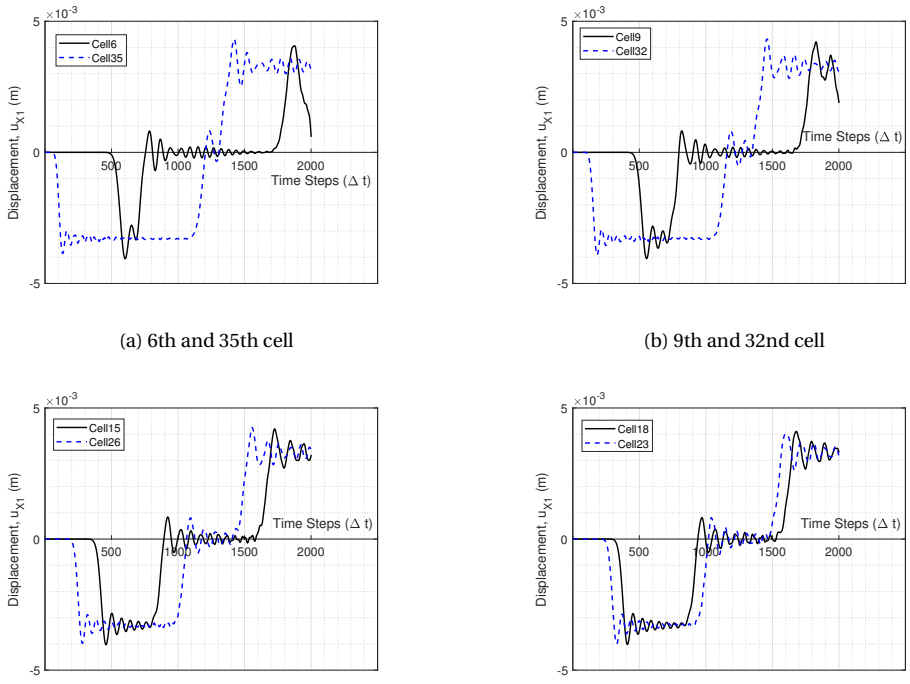

(a) 6th and 35th cell

(b) 9th and 32nd cell

(c) 15th and 26th cell

(d) 18th and 23rd cell

Figure 6.8: Displacement time graph of two nodes in various cells to estimate the wave velocity in X1 direction

Table 6.1: Comparison of results of longitudinal wave velocity in X1 direction by continuum approach and numerical analysis

h/l	**1.5**			**2.0**			**2.5**			**3.0**		
θ	**MS** [ms^{-1}]	**C** [ms^{-1}]	**E(%)**	**MS** [ms^{-1}]	**C** [ms^{-1}]	**E(%)**	**MS** [ms^{-1}]	**C** [ms^{-1}]	**E(%)**	**MS**	**C**	**E(%)**
-15°	3840.45	3699.14	3.68	3667.93	3460.23	5.66	3524.53	3262.34	7.44	3428.44	3094.92	9.73
-30°	1920.96	1803.58	6.11	1838.98	1687.10	8.26	1759.36	1590.61	9.59	1694.87	1508.99	10.97
-45°	1147.73	1051.32	8.40	1093.10	983.42	10.03	1037.60	927.18	10.64	984.58	879.60	10.66
-60°	-	-	-	641.50	569.62	11.20	606.65	537.04	11.47	576.77	509.48	11.67
-75°	-	-	-	298.20	264.70	11.23	281.15	249.56	11.23	267.30	236.75	11.43

are consistent with respect to the variation of speed with geometrical parameters. Two additional computational analyses showed that relatively larger magnitude of error obtained in results of table 6.1 could be decreased by increasing the number of unit cells for the same structural size. However, due to the large computational effort required for the increased number of unit cells, more analyses with the increased number of unit cells were not performed at this stage.

6.2.2. LOADING IN X2

The longitudinal wave speed in a re-entrant structure in X2 direction is also determined in a similar manner as discussed above. First of all, a re-entrant honeycomb structure is modelled by connecting a number of unit cells in X2 direction. The honeycomb structure is then loaded in X2 direction, and the result obtained from the dynamic analysis is compared with the wave velocity obtained by using the continuum approach.

Like the longitudinal wave velocity in X1 direction, the longitudinal wave velocity in X2 direction is also dependent on the effective elastic modulus of the re-entrant honeycomb structure in X2 direction and its effective density. According to continuum approach, the longitudinal wave velocity in X2 direction is obtained using:

$$c_{l,X2} = \sqrt{\frac{E_2}{\rho^\star}} \tag{6.2}$$

where E_2 and $\rho^\star$ are the effective elastic modulus in X2 direction and the effective density of a re-entrant unit cell respectively. The expressions of E_2 and $\rho^\star$ are shown in equations 5.5 and 2.21 respectively. Like other effective mechanical properties of a re-entrant honeycomb structure, the longitudinal wave velocity in X2 direction is also dependent on the geometrical parameters: $t/l, h/l$ and θ of the re-entrant honeycomb structure in addition to the material properties of the cell member i.e. the elastic modulus (E_s), density (ρ) and the Poisson's ratio (ν_s) of the cell member material.

In order to examine the variation of the longitudinal wave velocity in X2 direction ($c_{l,X2}$) with respect to geometrical parameters, a graph of $c_{l,X2}$ is plotted against the angle θ for different values of h/l. The results are based on $t/l = 0.1$, $E_s = 2e8$ Nm^{-2}, $\nu_s = 0$ and $\rho = 1$kgm^{-3}, and is shown in figure 6.9.

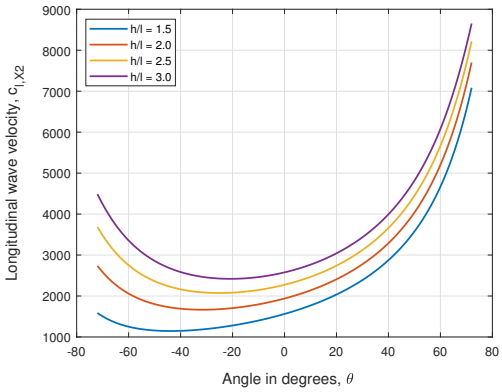

Figure 6.9: Variation of continuum estimation of $c_{l,X2}$ with respect to θ for different values of h/l

It can be observed in figure 6.9 that the trend of the longitudinal wave velocity in X2 direction with angle θ and the aspect ratio h/l is similar to the trend of the effective modulus in X2 direction with θ and h/l. The wave velocity increases with the increase in h/l ratio, whereas the variation with respect to θ is not consistent. In a conventional honeycomb, the wave velocity decreases with the decrease in the angle θ. However, in a re-entrant honeycomb, the wave velocity in X2 direction decreases with the increase in the re-entrant angle. But, after a certain point, the wave velocity starts to increase with the increase in the re-entrant angle. The turning point is dependent on the aspect ratio h/l. It can be observed in figure 6.9 that the turning point is present around -45° when $h/l = 1.5$. However, when $h/l = 3.0$, the turning point can already be observed around -20°. Comparing the results presented in figure 6.5 and 6.9, it can be noticed that the longitudinal wave velocity in X2 direction is higher than the wave velocity in X1 direction for the larger magnitude of re-entrant angles. The results shown in figure 6.9 are now compared with the computational results to validate the continuum approach of estimating the wave velocity in re-entrant structures.

Box 6.2.2: Longitudinal Wave Velocity in Re-entrant Structures

A re-entrant honeycomb structure is formed by connecting 40 unit cells in X2 direction. The single row of 40 unit cells in X2 direction is loaded in X2 direction at one end and restrained at the other end. The unit cells are modelled using following cell wall material properties and geometrical dimensions: $E_s = 2e8$ Nm^{-2}, $\nu_s = 0, \rho = 1$ kgm^{-3}, $b = 0.01$ m and $t/l = 0.1$. The ratio h/l and angle θ are varied between [1.5, 2.0, 2.5, 3.0] and [-15°, -30°, -45°, -60°, -75°] respectively. A model of the re-entrant

structure with $h/l = 2$ and $\theta = -45°$ is shown in figure 6.10
The finite element type, integration points and modelling techniques adopted in the analysis are the same as discussed in box 5.1.1. Each cell member is discretized into 8 elements, and all members are rigidly connected to each other. At the end cells, horizontal cell member of half length $(h/2)$ is extended outwards whose ends are used as loading and support points. At the restrained end of the assembly, all three degrees of freedoms $(u_{X1}, u_{X2}, \theta_z)$ are restrained. Similarly, at the loaded end, the re-entrant structure is subjected to a compressive external load in X2 direction. The trapezoidal load is used as an external load. The load has a rise time of 5 time steps to a value of 10 N, then stays constant at 10 N for five time steps and then decreases to 0 N again in five time steps. The time step used in the analysis is 0.4 μs. Like in the previous analysis, implicit time step method is used for the dynamic analysis.

Figure 6.10: Model of re-entrant structure to estimate the longitudinal wave velocity in X2 direction

The displacement of the connection of the horizontal and inclined members are recorded at various time steps to estimate the wave velocity in X2 direction. The difference between the time when the displacement in the direction of loading is maximum at two extreme nodes i.e. the one closest to the loaded end and the one closest to the restrained end is noted. The distance between these two points in X2 direction is then divided by the time difference which results in the computational estimation of the longitudinal wave velocity in X2 direction. The difference between the time when the displacement is maximum at other points which are away from the ends of the structure is also calculated to check the consistency of the results.
The computational result obtained from this procedure is then compared with the continuum approach estimation. As a comparative study, the analyses are performed for 18 re-entrant structures modelled using a set of values of h/l and θ specified above.

The analysis is first performed for a re-entrant structure modelled with $h/l = 2$ and $\theta = -45°$. The displacement (u_{X2}) - time graph of two end nodes at the top edge (described in box 6.2.2) is shown in figure 6.11. It can be seen that at the top edge, there are 80 nodes that are the connection of the inclined members and the horizontal members. These nodes are numbered 1 to 80, with 1 indicating the node at the end close to restraints and 80 indicating the node close to the loading end. The difference between the time when the displacement in X2 direction is maximum at these two nodes is 330 μs. As the distance between two nodes in X2 direction is 0.5142 m, the wave velocity in X2 direction is estimated to be 1558 ms^{-1}. The consistency of the result is checked by repeating the process for other nodes as well. The displacement time graph of the 17th and 64th nodes, the 21st and 60th nodes, the 25th and 56th nodes, and the 27th and 54th nodes are also shown in figure 6.12. The difference between the time when the displacement in X2 direction is maximum at those sets of points is found to be 200.4 μs, 165.6 μs, 130.4 μs and 113.2 μs respectively. This results in the wave speed in X2 direction to be 1534 ms^{-1}, 1544 ms^{-1}, 1564 ms^{-1} and 1573 ms^{-1} respectively. The effective modulus in X2 direction and the effective density of the re-entrant structure for the adopted values of geometrical dimensions and material properties are 656526.795 Nm^{-2} and 0.2188 kgm^{-3} respectively. For these values of effective elastic modulus and density, the continuum approach estimation of longitudinal wave velocity in X2 direction is 1732 ms^{-1}. The continuum approach estimation is found to be 11 % higher than the results obtained from the finite element simulations.

Next, the comparative study is done by comparing the results of the continuum approach and the computational analysis of the re-entrant structure modelled by varying the re-entrant angle θ and the aspect ratio h/l in a specified set of values listed in box 6.2.2. The finite element modelling technique and parameters, material properties and remaining geometrical parameters are still kept the same. The wave velocity in X2 direction is estimated by observing the displacement time profile of two nodes, and the consistency of the results are checked by comparing results with few other set of points too. The results of the finite element analysis and the continuum approach for all 18 analyzed cases are shown in table 6.2. The index MS, C and E(%) in the table represent results from the computational analysis of micro-structure, results from the continuum approach and the relative difference between the results respectively.

The results obtained from the computational analysis were found to follow the trend of continuum ap-

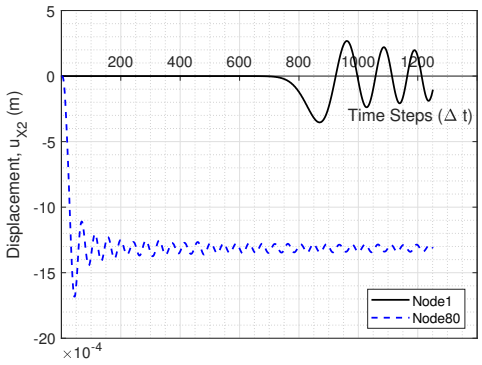

Figure 6.11: Displacement time graph of two nodes in 1st and 40th cell to estimate the wave velocity in X2 direction

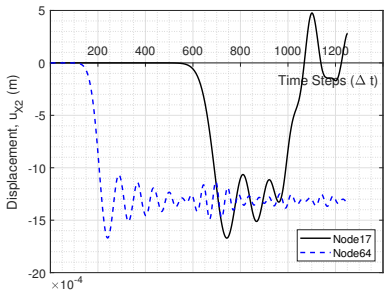

(a) 17th and 64th nodes

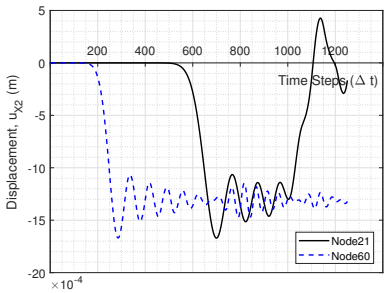

(b) 21st and 60th nodes

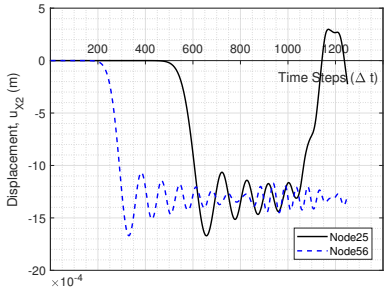

(c) 25th and 56th nodes

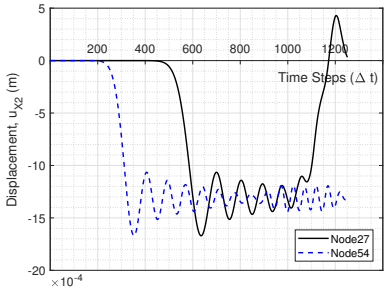

(d) 27th and 54th nodes

Figure 6.12: Displacement time graph of various nodes to estimate the wave velocity in X2 direction

Table 6.2: Comparison of results of longitudinal wave velocity in X2 direction by continuum approach and numerical analysis

h/l	**1.5**			**2.0**			**2.5**			**3.0**		
θ	**MS** [ms^{-1}]	**C** [ms^{-1}]	**E(%)**	**MS** [ms^{-1}]	**C** [ms^{-1}]	**E(%)**	**MS** [ms^{-1}]	**C** [ms^{-1}]	**E(%)**	**MS**	**C**	**E(%)**
-15°	1428.54	1336.21	6.46	1570.33	1744.61	11.10	1876.32	2106.62	12.27	2148.36	2432.32	13.22
-30°	1078.62	1194.86	10.78	1496.48	1666.15	11.34	1849.47	2081.68	12.56	2165.35	2453.66	13.31
-45°	1046.34	1146.09	9.53	1558.27	1732.35	11.17	1999.24	2244.85	12.29	2382.67	2699.86	13.31
-60°	-	-	-	1868.80	2058.37	10.14	2499.04	2751.38	10.10	2966.87	3355.81	13.11
-75°	-	-	-	2895.34	3011.26	4.00	3890.38	4043.82	3.94	4574.96	4898.80	7.08

proach results in terms of their variation with respect to the re-entrant angle θ and the aspect ratio h/l. The wave velocity increases with the increase in the aspect ratio h/l. The trend of the variation of the wave velocity with respect to a re-entrant angle is also in agreement with the results presented in figure 6.9. However, the results obtained from the finite element simulations and continuum approach estimation is found to be around 10 to 13 % different from each other. Two additional analyses were performed with two rows of 80 unit

cells along the length. The structural size of the assembled structure was kept same by modifying the magnitude of the length of horizontal ribs. The analyses with the increased number of unit cells were performed for $h/l = 2, \theta = -30^\circ$ and $h/l = 3, \theta = -60^\circ$. The longitudinal wave speed in X2 direction obtained from these analyses were found to be only 5.72% and 4.61% different than the results from the continuum approach. The results inferred that the relatively large magnitude of error presented in table 6.2 can be decreased with the increased number of unit cells for the constant structural size.

6.3. SHEAR WAVE PROBLEM

Now, after determining the longitudinal wave speed in both X1 and X2 directions in a re-entrant structure, the shear wave speed is determined as well. The static response of a re-entrant honeycomb structure when subjected to the shear loading and the computation of its effective shear modulus was discussed in chapter 5. Like in the estimation of the longitudinal wave velocity, both continuum approximation and numerical method are used to determine the shear wave speed in re-entrant structures.

The assembled re-entrant structure is modelled by connecting several unit cells in X2 direction. Then the re-entrant structure is loaded in shear, and the computational estimation of shear wave study is evaluated by observing the displacement-time profile at various positions in the structure. The continuum approximation of shear wave velocity on the other hand is obtained by using the relation:

$$c_s = \sqrt{\frac{G}{\rho^\star}} \tag{6.3}$$

where G and $\rho^\star$ are the effective shear modulus and effective density of a re-entrant unit cell respectively. The expressions of G and $\rho^\star$ are shown in equations 5.9 and 2.21 respectively. Like the effective shear modulus G and effective density $\rho^\star$, the shear wave speed c_s is also significantly affected by material properties of cell members E_s, ρ_s, and geometrical parameters such as $t/l, h/l$ and θ of a re-entrant honeycomb structure. To examine the variation of the shear wave velocity with the two geometrical parameters θ and h/l, a graph of shear wave velocity is plotted against the angle θ for different values of h/l. The result presented in figure 6.13 is based on $t/l = 0.1, E_s = 2e8$ Nm^{-2} and $\rho = 1$ kgm^{-3}

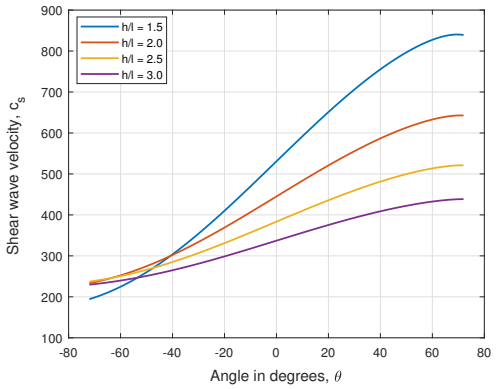

Figure 6.13: Variation of continuum estimation of c_s with respect to θ for different values of h/l

It is evident from figure 6.13 that the shear wave speed in re-entrant structures can be controlled by modifying the geometrical parameters, the aspect ratio h/l and an angle θ. For a conventional honeycomb, the shear wave speed decreases with the decrease in the angle θ. Whereas, in a re-entrant honeycomb, the shear wave speed decreases with the increase in the re-entrant angle (i.e. as θ becomes more negative). Also, comparing the results shown in figures 6.5, 6.9 and 6.13, the shear wave speed in a re-entrant structure is found to be remarkably lower than the longitudinal wave speed in either directions. The result shown in 6.13 is now compared with the computational estimation of the shear wave velocity in re-entrant structures.

Box 6.3.1: Shear Wave Velocity in Re-entrant Structures

The shear wave speed is determined computationally by performing dynamic analysis in a re-entrant honeycomb structure formed by connecting 40 unit cells in X2 direction. The single row of 40 unit cells in X2 direction is loaded in shear at one end and restrained at the other end. The model used

for examining the shear wave propagation speed is similar to the one used in determining the longitudinal wave speed in X2 direction. However, the loading and the boundary conditions are different in both the models. The unit cells are modelled using following cell wall material properties and geometrical dimensions: $E_s = 2e8$ Nm^{-2}, $\nu_s = 0, \rho = 1$ kgm^{-3}, $b = 0.01$ m and $t/l = 0.1$. The aspect ratio h/l and the re-entrant angle θ are varied between [1.5, 2.0, 2.5, 3.0] and [-15°, -30°, -45°, -60°, -75°] respectively. A model of the re-entrant structure with $h/l = 2$ and $\theta = -30°$ is shown in figure 6.14.
The finite element type, integration points and modelling techniques adopted in the analysis are same as discussed in box 5.1.1. Each cell member is discretized into 8 elements. At the end cells, horizontal cell member of half length $(h/2)$ is extended outwards whose ends are used as loading and support points. At the restrained end of the assembly, two degrees of freedoms (u_{X1} and u_{X2}) are restrained, whereas, the third degree of freedom θ_z is free i.e. the rotation is allowed at the restrained end. Similarly, at the loaded end, the re-entrant structure is subjected to a shear load. The load is applied in the X1 direction. As shear deformation is to be modelled, the connection of all cell members are also restrained in X2 direction. Therefore, the re-entrant structure is now only free to move in X1 direction thus producing the desired shearing effect. The trapezoidal load pulse is used as an external load. The load has a rise time of 5 time steps to a value of 10 N, then stays constant at 10 N for five time steps and then decreases to 0 N again in five time steps. The time step used in the analysis is 0.4 μs. Like in the previous analyses, implicit time step method is used for the dynamic analysis.

Figure 6.14: Model of re-entrant structure to estimate the shear wave velocity

The displacement of the connection of horizontal and inclined members are noted at various time steps to estimate the shear wave velocity. The difference between the time when displacement in X1 direction is maximum at two extreme nodes: the one closest to the loaded end and the one closest to the restrained end is noted. The distance between these two points along the direction of the propagation of a wave (i.e. along X2 direction) is then divided by the time difference which results in the computational estimation of the shear wave velocity. The difference between the time when the displacement is maximum in X1 direction at other pair of points which are away from the ends of the structure is also calculated to check the consistency of the results.
Finally, the results obtained from computational analysis and the continuum approach are compared with each other. As a comparative study, the analyses are performed for 18 different types of re-entrant structures modelled by varying the aspect ratio h/l and re-entrant angle θ in a certain range listed above.

A re-entrant structure modelled with $h/l = 2$ and $\theta = -30°$ is analyzed first. The displacement (u_{X1}) - time graph of two end nodes at the top edge (described in box 6.3.1) is shown in figure 6.15. Similar to the model used to measure the longitudinal wave speed in X2 direction, there are 80 nodes at the top edge that are the connection nodes of the inclined members and horizontal members. These nodes are numbered 1 to 80, with 1 indicating the node at the end close to restraints, and 80 indicating the node close to the loading end. The difference between the time when the displacement in X1 direction is maximum at these two nodes is 1.76 ms. As the distance between nodes in X2 direction is 0.5950 m, the shear wave velocity is estimated to be 338 ms^{-1}. The consistency of the result is checked by repeating the process for other nodes as well. The displacement time graph of the 3rd and 78th nodes, the 17th and 64th nodes, the 25th and 56th nodes, and the 31st and 50th nodes are also shown in figure 6.16. The difference between the time when the displacement in X1 direction is maximum at those sets of points is found to be 1.596 ms, 1.078 ms, 0.707 ms and 0.433 ms respectively. This results in the shear wave propagation speed to be 354 ms^{-1}, 329 ms^{-1}, 332 ms^{-1} and 335 ms^{-1}. The effective shear modulus and the effective density of the re-entrant structure for the adopted values of geometrical dimensions and material properties are 17176.2 Nm^{-2} and 0.1540 kgm^{-3} respectively. Substituting the values of the effective shear modulus and the density in equation 6.3, the continuum approach estimation of shear wave velocity is found to be 334 ms^{-1}. The continuum approach estimation is found to be only 1.44 % lower

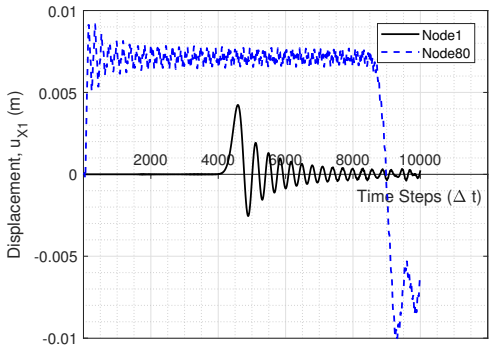

Figure 6.15: Displacement time graph of two nodes in 1st and 40th cell to estimate the shear wave velocity

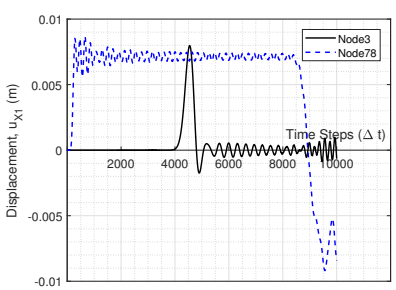

(a) 6th and 35th cell

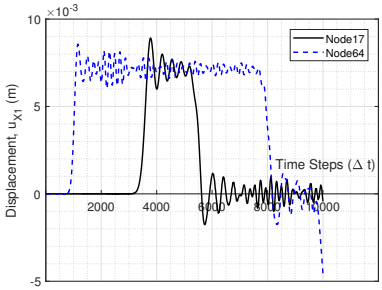

(b) 9th and 32nd cell

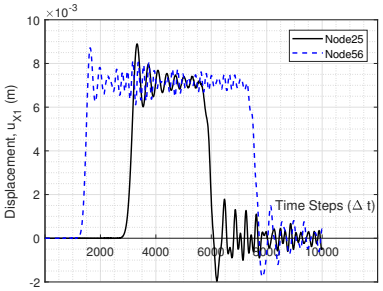

(c) 15th and 26th cell

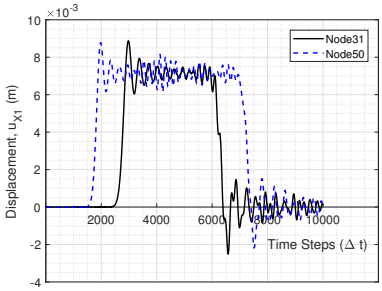

(d) 18th and 23rd cell

Figure 6.16: Displacement time graph of various nodes to estimate the shear wave velocity

Table 6.3: Comparison of results of shear wave velocity by continuum approach and numerical analysis

h/l	**1.5**			**2.0**			**2.5**			**3.0**		
θ	**MS** [ms^{-1}]	**C** [ms^{-1}]	**E(%)**	**MS** [ms^{-1}]	**C** [ms^{-1}]	**E(%)**	**MS** [ms^{-1}]	**C** [ms^{-1}]	**E(%)**	**MS**	**C**	**E(%)**
-15°	431.55	439.50	1.84	377.74	387.63	2.62	333.74	343.90	3.04	303.00	308.07	1.67
-30°	345.81	354.26	2.44	338.87	334.01	1.44	297.25	306.93	3.26	275.86	280.98	1.85
-45°	272.20	280.97	3.22	301.09	287.91	4.38	265.35	275.13	3.69	252.61	257.67	2.01
-60°	-	-	-	262.81	252.44	3.95	241.36	250.62	3.84	234.76	239.68	2.10
-75°	-	-	-	236.98	229.60	3.11	226.04	234.55	3.76	223.53	227.69	1.86

than the results obtained from the finite element simulations. The relative difference between the shear wave velocity obtained from the numerical simulations and the continuum approach is relatively lower than the difference obtained in estimating the longitudinal wave velocity in X1 direction and X2 direction.

Proceeding further, the numerical analysis is performed on re-entrant structures modelled by varying h/l and θ in the range listed in box 6.3.1. The finite element modelling technique and parameters, material prop-

erties and remaining geometrical parameters are kept the same. As explained before, for each case, the shear wave velocity is estimated by observing the displacement time profile of two nodes, and the consistency of results are checked by comparing results with few other set of points as well. The continuum approximation of the shear wave velocity in a re-entrant structure for adopted geometrical parameters is calculated using equation 6.3. The results of the shear wave velocity estimated by using finite element analysis and continuum approach for all 18 analyzed cases are shown in table 6.3. As specified before, index MS, C and E(%) in the table represent results from the computational analysis of a micro-structure, results from the continuum approach and the relative difference between the results respectively.

The computational results of the shear wave velocity was found to be decreasing with the increase in the aspect ratio h/l as predicted by the continuum approach approximation. The wave velocity is also observed to be decreasing with the increase in a re-entrant angle. Therefore, it is concluded that the trend of variation of shear wave velocity with respect to geometrical parameters is the same for both the continuum approximation and the computational analysis of cellular model. The results from both continuum approach and the cellular model were found to be relatively close to each other in comparison to the longitudinal wave velocity in either directions. All results were found to be within 1.5% to 5% difference. The shear wave problem is a one dimensional motion unlike the longitudinal wave problem in a two dimensional structure. As only one dimensional motion was dealt, relatively smaller magnitude of error was obtained on using the same number of unit cells as well.

6.4. SUMMARY OF DYNAMIC ANALYSIS OF MICRO-STRUCTURE

This chapter focused on the wave propagation characteristics and the speed of a wave propagation in a re-entrant honeycomb structure. First, the wave propagation characteristics in a re-entrant honeycomb unit cell was studied by examining the processes occurring at the kinks which are formed due to the connection of the cell members. The wave propagation phenomenon in a honeycomb structure is a result of several reflection, transmission, mode conversion and superposition of waves passing the kinks. The proportion of the reflection and transmission of the incident wave when it passes the kink can be controlled by modifying the angle between the cell members. Almost complete mode conversion of a incident wave takes place in a unit cell loaded in X1 direction when the re-entrant angle is -45°. This feature can be used in circumstances where it is beneficial to propagate the shear wave faster than the longitudinal wave in certain parts of the structure. The repeated process of reflection, transmission, mode conversion and superposition of waves occurring at the re-entrant structure sometimes lead to the destructive wave interference in a certain range of frequency. This feature of the re-entrant structure is called the band gap and is examined in detail in Chapter 7.

The longitudinal and shear wave velocity in a re-entrant honeycomb structure is computed from the results of the numerical analyses. The displacement time graph of certain nodes are obtained to estimate the wave velocity. The velocity in a certain direction is computed from the division of the distance between a pair of nodes by the difference between the time when displacement is maximum in the corresponding direction. The computational analyses for each type of wave speed was performed for 18 different cases formed by varying the aspect ratio h/l and a re-entrant angle θ. The results showed that like the effective modulii and Poisson's ratios of a re-entrant honeycomb structure, the wave speed can also be manipulated by modifying the geometrical parameters i.e. the ratio h/l and an angle θ. Besides, the computational study of wave propagation characteristics and wave speed also supported the findings of static analyses that a re-entrant honeycomb structure is strongly orthotropic in nature.

The close comparison of a cellular structural model and an equivalent continuum model subjected to bi-axial loading and three point bending in Chapter 5 had presented a groundwork for relating the cellular assembled model with an equivalent continuum model. Therefore, the wave speed results obtained from the finite element analyses were compared with the speed estimated using the continuum approach based on the effective mechanical properties of the re-entrant honeycomb structure. The results from both approaches were found to follow similar trend and variation with respect to two geometrical parameters, the aspect ratio h/l and a re-entrant angle θ. However, the relative difference between the results of the computational approach and the continuum approach is computed to be around 10% in the estimation of the longitudinal wave velocity in X1 and X2 direction. The shear wave velocity on the other hand is estimated with 5% relative difference between the computational and the continuum approach. The relatively large magnitude of error obtained in the computation of longitudinal wave speed was found to be reduced to around 5% after performing the computational analyses with the increased number of unit cells for the same structural size.

7

APPLICATION AND ADDITIONAL FEATURES

Interesting applications of auxetic structures were briefly highlighted in Section 2. One of the applications, the band gap exhibited by the re-entrant structures will be examined in the present section. In addition, the dispersion relation obtained from the Bloch wave analysis will be used to investigate the velocity of the plane wave propagation in the re-entrant structures. The results will then be utilized to make a comparison with the results of wave speed obtained from computational analysis and continuum approach in Section 6. Besides this, the possibility of having an isotropic re-entrant honeycomb structure will be discussed. The highly anisotropic behavior of re-entrant structure was evident from the results of previous sections. Therefore, it will be explored if it is possible to have an isotropic re-entrant structure by modifying geometrical parameters or any other modelling parameters.

7.1. STOP-PASS BAND

It is already evident from previous sections that a re-entrant honeycomb structure is a connection of the periodically repeated honeycomb unit cells. The periodicity of the re-entrant honeycomb structure is responsible for the way the structure responds to both static and dynamic loading conditions. One of the interesting features of such periodic structures when subjected to dynamic loading is exhibiting pass and stop bands. Researchers in physics and structural engineering have discovered that the wave propagation in periodic cellular structures like re-entrant honeycomb results in pass and stop bands [15]. The pass and stop bands are defined as the range of the frequency in which the wave propagation through the cellular structure is possible and not possible respectively. The stop and pass band is obtained as a result of the destructive wave interference phenomenon taking place in a certain frequency range [6]. The elastic wave propagation characteristics in a re-entrant honeycomb unit cell was discussed in detail in Section 6. The wave propagation results in a repeated process of reflection, transmission, mode-conversion and superposition of waves due to the geometrical discontinuity at every connection of cell members. This characteristic leads to the structure displaying the stop band feature in a certain range of frequency.

Like all effective mechanical properties of re-entrant honeycomb, the frequency range in which stop band is exhibited by the structure is also dependent on the geometrical parameters of the re-entrant honeycomb unit cell. Therefore, the range of the frequency in which the wave propagation in structure is to be prohibited can be monitored by varying the geometrical parameters of the unit cell that forms the structure. The feature of stop band can be used to isolate the wave propagation in a certain frequency range. This feature of the cellular structure is used for various acoustic applications, vibration isolation, photonic devices etc.

The stop-pass band of the re-entrant honeycomb structure is examined by obtaining the dispersion curve or dispersion surface of the structure. The dispersion curve is obtained by using the Bloch wave theorem. The use of the Bloch wave theorem to investigate the wave propagation in re-entrant honeycomb structure reduces the size of the problem. The theorem can be employed to study the wave propagation in a unit cell, and the results are used to understand the behavior of the structure formed by the connection of a number of unit cells. The dynamic analysis of the wave propagation in re-entrant structures is performed by using finite element method and the Bloch wave method. The concept of the Bloch wave method will be presented in brief at section 7.1.1. Later, the finite element method will be combined with the Bloch wave method to examine the band gap behavior of re-entrant structures.

7.1.1. BLOCH WAVE METHOD

A honeycomb structure is formed by the tessellation of the unit cells along lattice vectors. The lattice vectors in a conventional hexagonal honeycomb are shown in figure 7.1. It is considered that the unit cell shown in figure 7.1 is defined by the following geometrical parameters; θ: angle between the connection of vertical and inclined ribs, h: the dimension of the vertical rib, and $l/2$: the dimension of inclined ribs. Then, the lattice vectors $\mathbf{x_1}$ and $\mathbf{x_2}$ are given by:

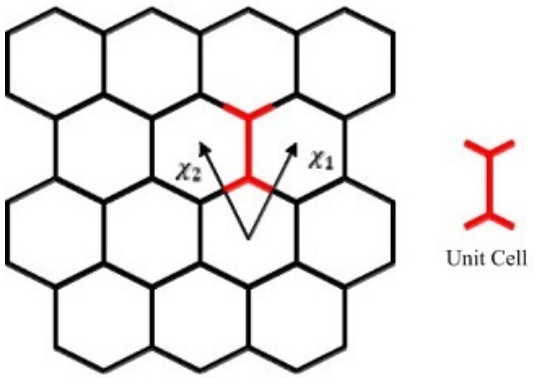

Figure 7.1: Conventional hexagonal honeycomb unit cell and lattice vectors [10]

$$\mathbf{x_1} = [lcos\theta, h + lsin\theta]^T \tag{7.1a}$$

$$\mathbf{x_2} = [-lcos\theta, h + lsin\theta]^T \tag{7.1b}$$

Let $\mathbf{r_j}$ and $u(\mathbf{r_j})$ represent the position and displacement of a lattice point in the reference unit cell respectively. During the propagation of an elastic plane wave in the assembly of unit cells, the displacement of the lattice point in the reference unit cell is given by:

$$u(\mathbf{r_j}) = u_j e^{(-i\omega t + \mathbf{k r_j})} \tag{7.2}$$

where, $u_j, \omega, \mathbf{k}$ represent the amplitude, angular frequency and Bloch wave vector respectively. Now, a point 'P' in an arbitrary unit cell corresponding to the point 'j' in the reference unit cell is considered. It is assumed that the arbitrary unit cell is located at n_1 translation along the lattice vector $\mathbf{x_1}$ and n_2 translation along the lattice vector $\mathbf{x_2}$. Therefore, the position of the point in the arbitrary unit cell corresponding to point 'j' in the reference unit cell is given by:

$$\mathbf{r_P} = \mathbf{r_j} + n_1\mathbf{x_1} + n_2\mathbf{x_2} \tag{7.3}$$

Then, the displacement of point 'P' in the arbitrary unit cell defined by the translation (n_1, n_2) is:

$$u(\mathbf{r_P}) = u_j e^{(-i\omega t + \mathbf{k r_P})} \tag{7.4}$$

Substituting $\mathbf{r_P}$ from equation 7.3 in equation 7.4, and using equation 7.2, it can be obtained that:

$$u(\mathbf{r_P}) = u(\mathbf{r_j}) e^{\mathbf{k}(\mathbf{r} - \mathbf{r_j})} \tag{7.5a}$$

$$u(\mathbf{r_P}) = u(\mathbf{r_j}) e^{\mathbf{k}(n_1\mathbf{x_1} + n_2\mathbf{x_2})} \tag{7.5b}$$

$$u(\mathbf{r_P}) = u(\mathbf{r_j}) e^{(k_1 n_1 + k_2 n_2)} \tag{7.5c}$$

where, k_1 and k_2 are the components of the Bloch wave vector $\mathbf{k}$ in the direction of the lattice vectors $\mathbf{x_1}$ and $\mathbf{x_2}$ i.e. $k_1 = \mathbf{k}.\mathbf{x_1}$ and $k_2 = \mathbf{k}.\mathbf{x_2}$. The components k_1, k_2 are complex number whose real and imaginary parts are represented by the attenuation of the amplitude, and change of phase during the wave propagation through unit cells respectively. During the process of identifying stop-pass bands, the wave propagating without attenuation is considered. Therefore, the real part of the components k_1 and k_2 are equal to zero, thus reducing the components to imaginary number: $k_i = i\epsilon_i$.

The Bloch theorem states that in a wave propagating through unit cells in a periodic structure, the proportion of the change of wave amplitude is independent of the position of the unit cell within the structure. Therefore, it provides a basis to understand the behavior of the wave propagation in the entire structure simply by studying the wave propagation in the reference unit cell. Equation 7.5c provides a periodic boundary condition between the displacements, and will be used later for the dynamic analysis of the unit cell.

For the direct lattice vectors defined in equation 7.1, the basis vectors of the reciprocal lattice are defined such that they satisfy the relation:

$$\mathbf{x_i x_j^\star} = \delta_{ij} \tag{7.6}$$

where $\mathbf{x_i}$ and $\mathbf{x_j^\star}$ are direct and reciprocal lattice vectors, and δ_{ij} is the Kronecker delta. For the hexagonal honeycomb considered in the present study, the reciprocal lattice vector is then obtained as:

$$\mathbf{x_1^\star} = \left[\frac{1}{2lcos\theta}, \frac{1}{2(h+lsin\theta)}\right]^T \tag{7.7a}$$

$$\mathbf{x_2^\star} = \left[-\frac{1}{2lcos\theta}, \frac{1}{2(h+lsin\theta)}\right]^T \tag{7.7b}$$

Also, the wave vector $\mathbf{k}$ when represented in terms of reciprocal lattice vectors, can be expressed as:

$$\mathbf{k} = k_1\mathbf{x_1^\star} + k_2\mathbf{x_2^\star} \tag{7.8}$$

Since the direct lattice vector is periodic, the reciprocal lattice vector is periodic as well. The reciprocal lattice defines the periodicity of the frequency-wave number relation. This periodicity of the reciprocal lattice further aids to reduce the problem of dynamic analysis as the relation of the wave vectors and frequency can now be examined only in a region in the reciprocal lattice known as the first Brillouin zone. The points in the first Brillouin zone are closer to the origin of the reciprocal lattice space compared to the other reciprocal lattice points. "The first Brillouin zone is also defined as the locus of points in the reciprocal lattice that can be reached from the origin of the reciprocal lattice without crossing any Bragg plane which bisects the reciprocal cell basis"[21]. The first Brillouin zone zone of the conventional hexagonal honeycomb is shown in figure 7.2.

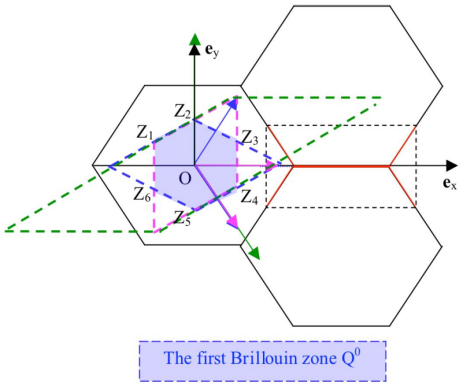

Figure 7.2: First Brillouin zone of conventional hexagonal honeycomb [21]

7.1.2. ANALYSIS OF FREE WAVE PROPAGATION

The finite element modelling of the re-entrant honeycomb structures was discussed in Section 5 and 6. The modelling technique and parameters adopted in previous analyses of the micro-structure are used in the determination of the band gap as well. The unit cell of the re-entrant honeycomb structure that will be considered for examining the band gap is shown in figure 7.3. As it can be seen in the figure, the unit cell comprises 5 cell members. The vertical cell member is of length h and four inclined cell members of the unit cell are of length $l/2$. The cell members are rigidly connected to each other, and each cell member is divided into 16 elements. After the assembly of the stiffness matrix and the mass matrix of the unit cell, the equation of motion of the unit cell can be expressed as:

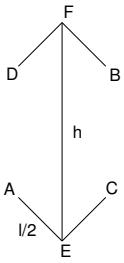

Figure 7.3: Unit cell of re-entrant hexagonal honeycomb used for analysis

$$\mathbf{M}\ddot{\mathbf{u}} + \mathbf{K}\mathbf{u} = \mathbf{f} \tag{7.9}$$

where **M**, **K**, **u**, **ü** and **f** are global mass matrix, global stiffness matrix, nodal displacement vector, nodal acceleration vector and external force vector of the unit cell respectively. During the propagation of the plane elastic wave with angular frequency ω, the equation of motion shown in equation 7.9 can be updated as:

$$(-\omega^2\mathbf{M} + \mathbf{K})\mathbf{u} = \mathbf{f} \tag{7.10}$$

The periodic boundary condition established with the aid of Bloch's wave theorem in the previous section is now used in conjunction with the finite element method to perform the dynamic analysis of the unit cell. The unit cell consists of six ends or connections. Points A, B, C and D are the points that are connected to neighboring cells, whereas points E and F are the points within the unit cell that connects three different unit cell members. Using equation 7.5c, the periodic boundary conditions that can be used for the points A, B, C and D are:

$$\mathbf{u_B} = \mathbf{u_A}e^{k_1} \tag{7.11a}$$

$$\mathbf{u_D} = \mathbf{u_C}e^{k_2} \tag{7.11b}$$

The nodal displacement vector **u** introduced in equation 7.9 can be expressed as $[\mathbf{u_A}, \mathbf{u_B}, \mathbf{u_C}, \mathbf{u_D}, \mathbf{u_i}]^T$ where $\mathbf{u_A}, \mathbf{u_B}, \mathbf{u_C}, \mathbf{u_D}$ denotes the displacement at nodes A, B, C and D, and $\mathbf{u_i}$ denotes the displacement at all other internal nodes in the unit cell including nodes E and F. After applying the periodic boundary conditions, the reduced nodal displacement vector can be written as: $\mathbf{u_r} = [\mathbf{u_A}, \mathbf{u_C}, \mathbf{u_i}]^T$. Therefore, the nodal displacement vector **u** and the reduced nodal displacement vector $\mathbf{u_r}$ can be expressed as:

$$\mathbf{u} = \mathbf{L}\mathbf{u_r} \tag{7.12}$$

where, **L** is the transformation matrix given by:

$$\mathbf{L} = \begin{bmatrix} \mathbf{I} & \mathbf{0} & \mathbf{0} & \mathbf{0} & ..... & \mathbf{0} & \mathbf{0} \\ \mathbf{I}e^{k_1} & \mathbf{0} & \mathbf{0} & \mathbf{0} & ..... & \mathbf{0} & \mathbf{0} \\ \mathbf{0} & \mathbf{I} & \mathbf{0} & \mathbf{0} & ..... & \mathbf{0} & \mathbf{0} \\ \mathbf{0} & \mathbf{I}e^{k_2} & \mathbf{0} & \mathbf{0} & ..... & \mathbf{0} & \mathbf{0} \\ \mathbf{0} & \mathbf{0} & \mathbf{I} & \mathbf{0} & ..... & \mathbf{0} & \mathbf{0} \\ \mathbf{0} & \mathbf{0} & \mathbf{0} & \mathbf{I} & ..... & \mathbf{0} & \mathbf{0} \\ : & : & : & : & ..... & : & : \\ \mathbf{0} & \mathbf{0} & \mathbf{0} & \mathbf{0} & ..... & \mathbf{I} & \mathbf{0} \\ \mathbf{0} & \mathbf{0} & \mathbf{0} & \mathbf{0} & ..... & \mathbf{0} & \mathbf{I} \end{bmatrix} \tag{7.13}$$

with **I** and **0** as identity matrix and zero matrix of dimension 3 x 3 respectively. Now, substituting the transformation represented by equation 7.12 in equation 7.10, pre-multiplying the outcome with $\mathbf{L^T}$, where $\mathbf{L^T}$ is the complex transpose conjugate of **L**, and considering the free wave motion i.e. **f** = 0, the resulting equation of motion is:

$$(-\omega^2\mathbf{L^T}\mathbf{M}\mathbf{L} + \mathbf{L^T}\mathbf{K}\mathbf{L})\mathbf{u_r} = 0 \tag{7.14a}$$

$$(-\omega^2\mathbf{M_r} + \mathbf{K_r})\mathbf{u_r} = 0 \tag{7.14b}$$

The matrices $\mathbf{M_r}$ and $\mathbf{K_r}$ are reduced mass and stiffness matrices respectively. As the transformation matrix $\mathbf{L}$ is a function of components of Bloch wave vector $\mathbf{k}$: k_1 and k_2, the reduced matrices $\mathbf{M_r}$ and $\mathbf{K_r}$ are also the functions of k_1 and k_2. Therefore, the eigenvalue problem given in in equation 7.14b has three unknowns: k_1, k_2 and ω. The solution of the equation is only possible when two of the three unknowns are defined. It has already been mentioned earlier that the wave without attenuation during propagation through the unit cells is taken into consideration to obtain the dispersion relation. Thus, the components k_1 and k_2 are imaginary numbers with $k_1 = i\epsilon_1$ and $k_2 = i\epsilon_2$. The phase constant ϵ_i vary within the first Brillouin zone in the reciprocal space. Thus, the result of the eigenvalue problem in equation 7.14b is the frequency of the wave propagation for a set of values of k_1 and k_2 i.e. $\omega = \omega(k_1, k_2)$. The solution yields the surface known as dispersion surfaces $(\omega - k_1 - k_2)$, and the number of surfaces is equal to the number of eigenvalues. When any of these two dispersion surfaces do not cross each other, the gap thus created between the surfaces is called stop band or band gap. The propagation of wave with the frequencies in this range do not take place.

The computational effort in obtaining the dispersion relation can be further reduced due to the symmetry of the first Brillouin zone. The phase constants ϵ_1 and ϵ_2 need not vary in the first Brillouin zone, but is sufficient to vary along the edge of the irreducible zone. This method of reducing the size of the computational analysis is widely used in literature and the results have been promising [6]. For the first Brillouin zone shown in figure 7.2, the irreducible zone is shown in figure 7.4.

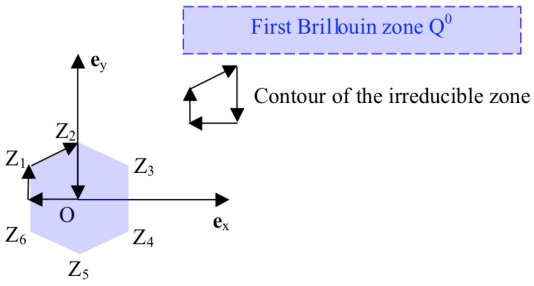

Figure 7.4: Irreducible zone of the first Brillouin zone of conventional hexagonal honeycomb unit cell [21]

The position of the corners of the irreducible Brillouin zone shown in figure 7.4 are evaluated in terms of the reciprocal lattice vectors $\mathbf{x_1^\star}$ and $\mathbf{x_2^\star}$. The derivation of expressions that define these position in terms of the reciprocal basis vectors is shown in Appendix C. The edges of the irreducible zone are then discretized to vary the components k_1 and k_2 along these edges.

Both methods discussed above are used to obtain the dispersion relation in a unit cell. The numerical simulations are first performed to obtain the dispersion surface in $\omega - k_1 - k_2$ co-ordinates. The phase constant ϵ_i is varied in the range $[-2\pi\ 2\pi]$. Then, the numerical simulation is limited only to the irreducible edge of the first Brillouin zone. The results obtained from these simulations are used for the comparison, and to observe the band gap behavior of the re-entrant honeycomb structures.

7.1.3. BAND GAP IN RE-ENTRANT HONEYCOMB LATTICE

Two different cases of re-entrant honeycomb structures were considered for analyzing the dispersion relation. The mechanical properties, out of plane width and the slenderness of the cell members were kept constant in the considered cases. The parameters that were kept constant were: $E_s = 2e8$ Nm^{-2}, $\rho = 1$ kgm^{-3}, $b = 0.01$ m, and $t/l = 0.1$. However, the re-entrant angle θ and the aspect ratio h/l were varied. Two different cases considered during the analysis are: $(i)\theta = -60°, h/l = 3.0$ and $(ii)\theta = -30°, h/l = 2.5$. These two cases are selected in such a way that one configuration exhibits the band gap and the other one does not. The results highlight the fact that the band gaps characteristics exhibited by the re-entrant honeycomb structure can be manipulated by modifying the geometrical parameters of the honeycomb unit cell.

Only the first ten eigenvalues are considered to obtain the dispersion relation. The results of the dispersion analysis of a re-entrant honeycomb structure are shown in figures 7.5, 7.6 and 7.7. Figure 7.5 shows the dispersion surface obtained from the complete analysis, and figure 7.6 shows the surface shown in the previous figure when viewed in the $\omega - k_1$ plane. The complete relation between wave angular frequency (ω) and components of the wave vector (k_1, k_2) is provided by the results of the full analysis. Whereas, figure 7.7 shows the dispersion relation along the irreducible edge of first Brillouin Zone. The vertical axis in figure 7.7 represents the angular frequency and the horizontal axis represents the position along the irreducible edge of the first Brillouin Zone. The wave vector components k_1 and k_2 are discretized along the edges, and the

angular frequency is obtained for each of these values. The dispersion relation obtained on the edge of first Brillouin zone mainly highlights the band gap exhibited by the structure (if any).

The dispersion surface shown in figure 7.5(a) shows a complete gap between the eighth and the ninth eigenvalue. The band gap is more evident in figures 7.6 and 7.7. The wave motion does not occur in this range of the angular frequency as the solution to the eigenvalue problem shown in equation 7.14b does not exist for this range of angular frequency ω. However, all other angular frequencies are on the dispersion surface implying that the wave motion occurs for those values. In addition to the complete band-gap, partial band-gaps can also be observed in the three figures. A partial band-gap means the range of the angular frequency in which the wave motion does not take place for certain values of the wave vector $\mathbf{k}$.

However, the dispersion surface of the second re-entrant honeycomb structure does not exhibit any complete band gap behavior. The results for the second case are shown in figures 7.5(b). For the adopted geometrical configuration and material properties, the honeycomb structure does not exhibit any band gap behavior. Although there exist some partial band gaps as observed in figures 7.5 - figure 7.7, there is no range of frequency in which the motion does not take place for any values of k_1 and k_2. Two honeycomb structures considered in this study were modelled using same cell member material properties, with h/l and θ as the only differences between the two models. However, by simply varying the re-entrant angle θ and the aspect ratio h/l, the characteristic of the wave propagation could be significantly altered in a honeycomb structure.

The results presented in figure 7.5 and figure 7.7 are similar to each other. Thus, it validates the assumption that the dispersion analysis can be limited to the irreducible edge of the first Brillouin zone. This technique significantly reduces the computation effort to identify the band gap characteristics of the honeycomb structure. In addition, the dispersion relation obtained along this zone can also be used to determine the dilatation and shear wave velocity of the honeycomb structure which is discussed in detail in the next section.

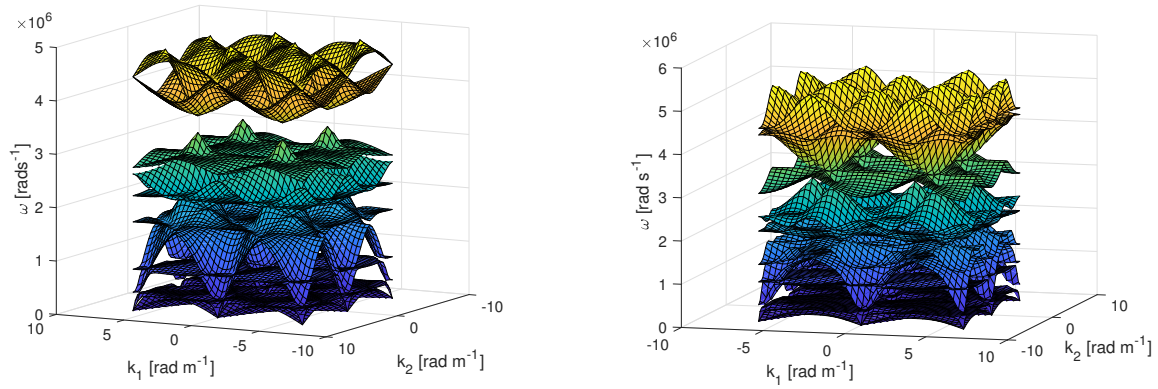

(a) $\theta = -60°, h/l = 3.0$ (b) $\theta = -30°, h/l = 2.5$

Figure 7.5: 3D dispersion surface showing the band gap behavior of re-entrant honeycomb structures with different θ and h/l

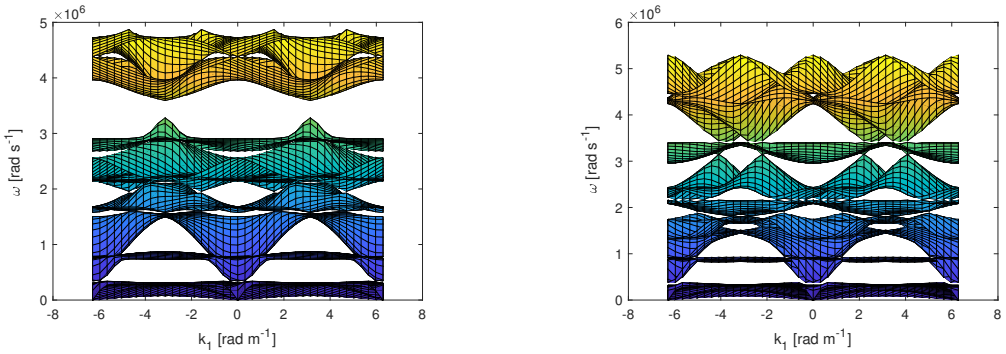

(a) $\theta = -60°, h/l = 3.0$ (b) $\theta = -30°, h/l = 2.5$

Figure 7.6: Dispersion surface observed in $\omega - k_1$ plane for re-entrant honeycomb structures with different θ and h/l

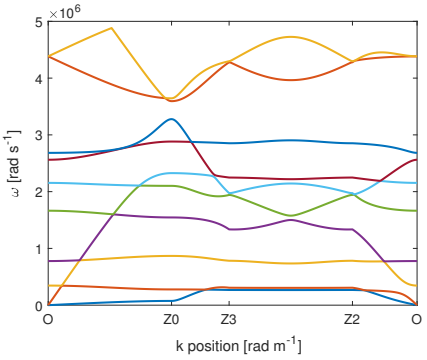

(a) $\theta = -60°, h/l = 3.0$

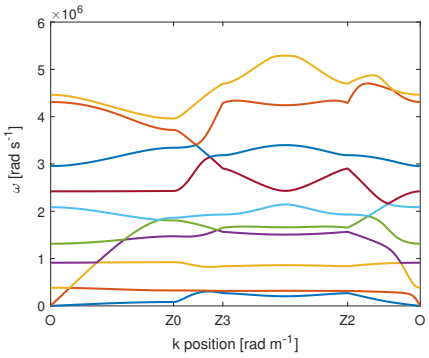

(b) $\theta = -30°, h/l = 2.5$

Figure 7.7: Dispersion curve obtained by varying k_1 and k_2 along the edge of the irreducible First Brillouin Zone for re-entrant honeycomb structures with different θ and h/l

7.2. WAVE VELOCITIES FROM BAND GAP

The point O in figure 7.7 represents the origin of the first Brillouin zone which also corresponds to the long wavelength limit. It can be observed in the figure that two curves start from the origin O. These two curves represent the dilatational wave and shear wave. The first branch corresponds to the shear wave and the second branch corresponds to the dilatational wave in X2 direction. The dispersion relation containing only these two curves is shown in figure 7.8.

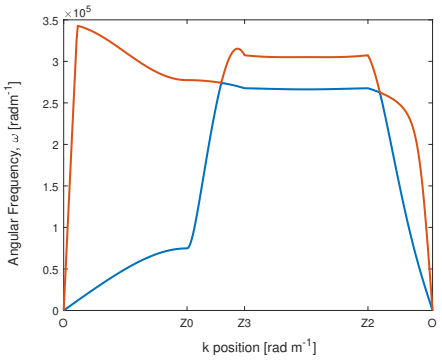

(a) $\theta = -60°, h/l = 3.0$

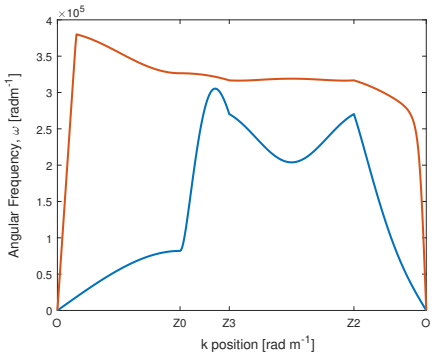

(b) $\theta = -30°, h/l = 2.5$

Figure 7.8: Dispersion curve showing only two branches starting at origin O

It is known that the tangent to the dispersion curve at a point, corresponds to the group velocity. Therefore, the tangent to the two branches shown in the figure above at any point in the low frequency range gives the group velocities which are equal to the dilatational and shear wave velocities. It indicates that the honeycomb structure appears to be non-dispersive at low frequency, high wavelength limit. The group velocities obtained from the results presented in figure 7.8 are compared with the continuum approach approximation of dilatational and shear wave velocities. According to continuum approach, the dilatational and shear wave velocities are given by:

$$c_{1,X2} = \sqrt{\frac{E_2}{\rho^\star (1 - \nu_{12}\nu_{21})}} \tag{7.15a}$$

$$c_2 = \sqrt{\frac{G_{12}}{\rho^\star}} \tag{7.15b}$$

where $c_{1,X2}, c_2, E_2, G_{12}, \nu_{12}, \nu 21, \rho^\star$ represent dilatational wave velocity in X2 direction, shear wave velocity, effective Young's modulus in X2 direction, effective shear modulus, Poisson's ratio in X1 direction, Pois-

son's ratio in X2 direction and effective density respectively.

As mentioned earlier, the wave velocity can be obtained from the dispersion relation shown in figure 7.8 by finding the slope of the tangent at any point in the dispersion curve i.e. $c = \frac{\Delta\omega}{\Delta|\mathbf{k}|}$. The wave vector $\mathbf{k}$ is given by equation 7.8. The results obtained from this method are then compared with the wave velocity results obtained using equation 7.15. The effective mechanical properties to be used in equation 7.15 are determined either by using analytical formulas presented in previous sections or through computational analysis. The comparative study of estimation of wave velocities using the Bloch wave method and continuum approach is done for a range of values of h/l and θ. The aspect ratio h/l and the re-entrant angle θ are varied between [1.5, 2.0, 2.5, 3.0] and $[-15°, -30°, -45°, -60°, -75°]$ respectively. As the ratio $h/l = 1.5$ can not be used in conjunction with $\theta = -60°$ and $-75°$, 18 different cases are considered for the comparative study. The results are presented in tables 7.1 and 7.2. The index B, C and $E(\%)$ represent the wave velocity obtained from the Bloch wave method, the wave velocity obtained from continuum approach and the relative difference between the results respectively. It was found from the analyses that the Bloch wave method used in conjunction with Finite element method correctly estimated the wave velocity using effective mechanical properties of the honeycomb structure.

Table 7.1: Comparison of results of dilatational wave velocity in X2 direction obtained from Bloch wave method and continuum approach

h/l	**1.5**			**3**			**2.5**			**3.0**		
θ	**B** [ms^{-1}]	**C** [ms^{-1}]	**E(%)**	**B** [ms^{-1}]	**C** [ms^{-1}]	**E(%)**	**B** [ms^{-1}]	**C** [ms^{-1}]	**E(%)**	**B** [ms^{-1}]	**C** [ms^{-1}]	**E(%)**
-15	3302.79	3302.69	0.003	4205.60	4205.60	0.000	4960.99	4961.03	0.001	5603.99	5604.06	0.001
-30	4073.86	4073.88	0.0005	5341.17	5341.45	0.005	6325.18	6325.53	0.006	7111.33	7111.67	0.005
-45	3798.08	3798.11	0.001	5286.42	5286.74	0.006	6397.39	6397.79	0.006	7259.17	7259.55	0.005
-60	-	-	-	4911.97	4912.25	0.006	6123.21	6123.52	0.005	7050.08	7050.37	0.004
-75	-	-	-	4591.83	4592.01	0.004	5869.82	5870.00	0.003	6841.62	6841.79	0.003

Table 7.2: Comparison of results of shear wave velocity obtained from Bloch wave method and continuum approach

h/l	**1.5**			**3**			**2.5**			**3.0**		
θ	**B** [ms^{-1}]	**C** [ms^{-1}]	**E(%)**	**B** [ms^{-1}]	**C** [ms^{-1}]	**E(%)**	**B** [ms^{-1}]	**C** [ms^{-1}]	**E(%)**	**B** [ms^{-1}]	**C** [ms^{-1}]	**E(%)**
-15	439.80	439.50	0.067	388.05	387.63	0.109	344.35	343.90	0.131	308.51	308.07	0.144
-30	354.41	354.26	0.042	334.32	334.01	0.094	307.30	306.93	0.120	281.36	280.98	0.137
-45	281.03	280.97	0.020	288.14	287.91	0.079	275.43	275.13	0.110	258.01	257.67	0.130
-60	-	-	-	252.60	252.44	0.065	250.87	250.62	0.101	239.98	239.68	0.122
-75	-	-	-	229.72	229.60	0.053	234.77	234.55	0.094	227.96	227.69	0.118

However, at higher frequencies of wave propagation the wave velocity predicted using equations 7.15 do not hold. At higher frequencies (low wavelength limit), the honeycomb structure appears to be more dispersive, and the effective properties theory also no longer holds.

7.3. ISOTROPIC BEHAVIOR IN MICRO-STRUCTURE

From the computational and analytical results presented in Sections 5 and 6, it has already been noted that the re-entrant honeycomb structure is orthotropic in nature. The direct relation of the Poisson's ratio and other mechanical properties such as indentation resistance, fracture toughness, shear resistance etc. are only available for isotropic materials. Therefore, these relations can not be used directly for re-entrant honeycomb structures which exhibit strong auxetic behavior. In this section, the possibility of having an isotropic re-entrant honeycomb structure will be explored.

In an isotropic material, material properties are invariant in any direction, and there are only two independent elastic constants. Assuming that the Young's modulus and Poisson's ratio are two independent elastic constants, then the shear modulus (G) is related to two independent constants E and ν through $G = \frac{E}{2(1+\nu)}$. Therefore, the goal is to find the values of the geometrical parameters of re-entrant honeycomb structure which satisfies the condition of isotropy. The expressions of effective mechanical properties presented in equations 2.22 - 2.26 are considered in this process. These expressions were derived by Gibson [4] only considering the flexural deformation of cell members.

The isotropic behavior is only achieved in re-entrant honeycomb structure when the following relations

hold true between the effective mechanical properties:

$$E_1 = E_2 = E \tag{7.16a}$$

$$\nu_{12} = \nu_{21} = \nu \tag{7.16b}$$

$$G_{12} = \frac{E}{2(1+\nu)} \tag{7.16c}$$

As expressions of E_1, E_2, ν_{12} and ν_{21} are based on the relation $E_1\nu_{21} = E_2\nu_{12}$, enforcing $E_1 = E_2$, automatically leads to $\nu_{12} = \nu_{21}$. The expressions presented in equations 2.22 - 2.26 are substituted in equation 7.16. However, the solution to the set of equations presented in equation 7.16 does not exist. There is not any combination of the real values of aspect ratio h/l and re-entrant angle θ that satisfies the relation of isotropy. Thus, it implies that it is not possible to have an isotropic re-entrant honeycomb structure for the considered deformation mechanism. The relation was checked for conventional honeycomb as well. And, it was found that only at $h/l = 1$ and $\theta = 30°$ i.e. a regular hexagonal honeycomb, the condition of isotropy is satisfied.

Now, with the finding that it is not possible to obtain completely isotropic re-entrant honeycomb structure, the possibility of having a re-entrant honeycomb structure with equal Young's modulus and Poisson's ratio in two lateral directions is examined. The relation given in equation 7.16a is solved to find the relation between two geometrical parameters, the aspect ratio h/l and the re-entrant angle θ which results to equal effective Young's modulus in X1 and X2 direction. The required relation between h/l and θ is found to be:

$$h/l = -\frac{1}{sin\theta} \tag{7.17a}$$

$$h/l = -\frac{2sin^2\theta - 1}{sin\theta} \tag{7.17b}$$

The additional conditions regarding the values of h/l i.e. $h/l > 0$ and $h/l > 2 \mid sin\theta \mid$ (for re-entrant honeycomb) mean the solution obtained in equation 7.17b is not applicable. The values of h/l and re-entrant angle θ that satisfies the above mentioned two conditions and the equation 7.17a is shown in figure 7.9.

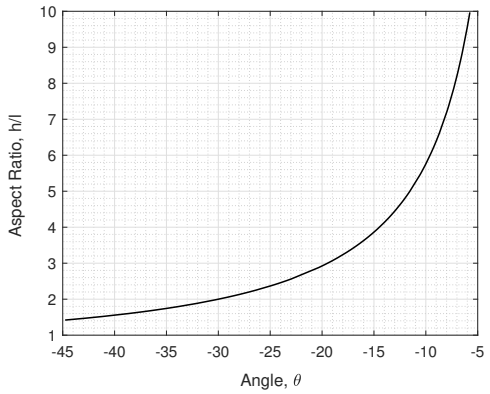

Figure 7.9: Combination of values of h/l and θ resulting in equal effective elastic modulus in two lateral directions

Masters et al. [13] investigated the behavior of re-entrant structures using different deformation mechanism. Stretching and hinging deformation were taken into account in addition to the flexure of the inclined ribs. It was found that near isotropic re-entrant structures can be obtained when only stretching was taken into account. However, when any other deformation mechanism was combined with it, the isotropy could no longer be achieved [13].

8

CONCLUSIONS AND RECOMMENDATIONS

8.1. CONCLUSIONS

The main objective of this thesis was to examine the deformation behavior of auxetics. Computational tools were developed and validated to perform numerical analyses of continuum models of auxetic material and the re-entrant honeycomb micro-structures subjected to different static and dynamic loading conditions. The finite element code programmed to analyze a continuum model resolves the limitation of many commercial finite element packages which can not be used to analyze isotropic auxetics. Similarly, the code programmed to analyze a re-entrant honeycomb structure can be used to have a better understanding of the cellular structure, such as: response to geometrical nonlinear conditions, bending etc. that are not possible just through the analytical relations. The finite element analyses results obtained in this thesis have not only unveiled the deformation behavior of auxetics, but also pointed a direction for future research. The main conclusions of the thesis are described referring to the research questions presented earlier in section 1.2

1. *How is dynamic wave propagation affected in an auxetic continuum?*

   The effect of a negative Poisson's ratio on the speed of a dilatational wave and shear wave was studied in the computational analysis of a one-dimensional wave motion. The results from the computational analyses of a one-dimensional wave motion were found to be in agreement with the theoretical predictions for a linear elastic isotropic material. As the shear modulus in such a material increases with the decrease in a Poisson's ratio, the shear wave velocity was also found to be increasing with the increase in the auxetic effect. Like the shear wave speed, the dilatational wave speed also increases with the increase in the auxetic effect. However, the effect of auxeticity is more pronounced on the shear wave velocity compared to the dilatational wave speed. Therefore, the ratio of the dilatational wave speed to the shear wave speed decreases continuously in the auxetic range of negative Poisson's ratio.

   After obtaining a close comparison of the computational results and the theoretical predictions regarding one dimensional motion in an isotropic auxetic continuum, the finite element code was then used to analyze the two-dimensional wave motion; a beam impact problem. The computational analysis of the beam impact problem presented some complications due to the presence of the spurious finite element modes modes. Modal analysis and the B-bar method were preferred over the standard finite element method to analyze the beam impact problem. The relative difference of the results obtained from the Modal analysis and the B-bar method were less than 5%, and the methods were useful to fix the problem of spurious modes in the middle portion of the beam. However, the results on the top edge of the beam were still found to suffer from the problem of spurious modes and mesh dependency. Computational analysis of a beam impact problem supported the theoretical prediction that in an auxetic structure, the material flows towards the point of impact. Also, the results highlighted that the wave propagates faster but with a reduced intensity of deformation in highly auxetic materials. This characteristic of auxetic materials can be useful to mitigate shock and impact forces in a structure.

2. *How can a cellular structure be modelled in order to exhibit a negative Poisson's ratio?*

   The shape and configuration of a cellular structure such as a honeycomb structure can be modified such that it exhibits a negative Poisson's effect solely due to its geometrical configuration. When a

honeycomb structure is formed with a re-entrant angle between a horizontal and an inclined rib, the honeycomb structure displays an auxetic behavior. The magnitude of the Poisson's ratio exhibited by a re-entrant honeycomb structure depends on its geometrical parameters; the aspect ratio h/l and the re-entrant angle θ. In addition to the geometrical parameters, the effective mechanical properties of a re-entrant honeycomb structure also depend on the direction of loading, indicating its strongly orthotropic characteristics. The finite element analyses of re-entrant honeycomb structures with varying aspect ratio h/l and a re-entrant angle θ revealed the possibility of achieving a Poisson's ratio more negative than -1. This particular feature can be exploited in defense related applications as a small longitudinal compression results in a large lateral compression.

The computational results of the Poisson's ratio exhibited by a unit cell was noted to be less than 1% different than the analytical predictions. Such a close comparison of results mean the finite element code was validated and therefore could be used to assess other behaviors of a re-entrant honeycomb structure such as geometrical nonlinear behavior, response to bi-axial loading, response to bending etc. The geometrical nonlinear analysis of a re-entrant honeycomb structure highlighted that the re-entrant structure becomes stiffer and more auxetic with the increase in the compressive deformation in X2 direction. This characteristic of a re-entrant structure makes it more attractive in alleviating the effect of impact.

The good resemblance of the results obtained from the computational analyses of the assembled structure of the re-entrant honeycomb unit cells and an equivalent continuum subjected to bi-axial loading and bending laid out the possibility of assessing the global behavior of a cellular structure using its homogenized mechanical properties. The results from both models were found to be less than 6% different. The error is expected to decrease in the analysis of an assembled discrete model with the increased number of unit cells for the same structural size. The link between the assembled cellular model and an equivalent continuum model means that it is possible to perform a pre-analysis in a continuum model and then use the continuum results to design a suitable re-entrant honeycomb structure.

3. *How do auxetic cellular structures respond to dynamic loading conditions?*

   The characteristics and the average speed of a wave propagation in an auxetic cellular structure was studied through the finite element analysis of a re-entrant honeycomb structure subjected to dynamic loading conditions. The wave propagation in a re-entrant honeycomb structures is the result of several reflection, transmission, mode conversion and super position of waves occurring at the connection of cell members. The proportion of these processes is dependent on the magnitude of the re-entrant angle between the cell ribs. Therefore, it is possible to control the wave propagation characteristics simply by modifying the re-entrant angle between the cell members. The apparent longitudinal wave velocities in X1 and X2 directions, and the shear wave velocity computed from the dynamic analysis of the assembly of re-entrant honeycomb unit cells presented the dependence of the wave velocities on the geometrical parameters of a unit cell; the aspect ratio h/l and a re-entrant angle θ. The wave speed obtained from the continuum approach estimation using the effective mechanical properties and the computational analyses was found to have a similar trend and variation with respect to h/l and θ. However, the results of the longitudinal wave speed in X1 and X2 direction were computed to be approximately 10% different than the continuum approach estimation. Additional finite element analyses using the increased number of unit cells for the same structural size showed that the error was reduced to about 5%. This indicates that the close to homogeneous response is obtained on using the large number of unit cells for the same structural size. The relative difference between the results from a cellular modal and the continuum approach was less than 5% in the estimation of shear wave velocities.

   Furthermore, in an additional study, the stop-pass band characteristics exhibited by the re-entrant honeycomb structures subjected to dynamic loading was investigated as well. The study was performed by using the Bloch wave theorem in conjunction with the finite element analysis. The results showed that the frequency range in which the stop-band is exhibited by a re-entrant honeycomb structure can be controlled by modifying the geometrical parameters; the aspect ratio h/l and a re-entrant angle θ. This finding presented the possibility to have a structure with desired acoustic filtering application. The dispersion curve obtained from the Bloch wave analysis indicated that the wave velocity in a re-entrant honeycomb cellular structure in high wavelength limit can be correctly estimated using the continuum approach with homogenized mechanical properties.

4. *What are the mechanical requirements of a cellular structure elements and nodes to enable auxetic dynamic behavior?*

   The cell members of a re-entrant honeycomb cellular structure were assumed to be rigidly connected to each other in this thesis. As a result of the fully stiff connection between the cell members, the primary deformation of a unit cell loaded in either directions was the bending of the inclined ribs. The contribution of an axial and shear deformation was significant only for less slender cell members and the values of a re-entrant angle close to 0° and -90°. Besides, the rigidity of the connection between cell members is a matter of interest more from the dynamics point of view. As the process of wave reflection, transmission and mode conversion take place at the connection of cell members, the rigidity is expected to influence the dynamics characteristics significantly.

   Although the effective Poisson's ratio of a re-entrant honeycomb cellular structure is not dependent on the mechanical properties of cell members, the remaining effective mechanical properties exhibited by a cellular structure depends on the cell member properties. The effective in-plane elastic modulii and the effective density of the honeycomb structure is found to be reduced by the order of 2 to 3 compared to its cell member material properties. As a result, also the apparent longitudinal and shear wave velocities in a honeycomb cellular structure is slower than the wave speed in individual cell members. The reduction in the effective elastic modulii is considered to be one of the constraints in the design and practical use of auxetic cellular structures. However, the flexibility, light weight and auxetic behavior it possesses can be beneficial in applications that need high deformations under targeted loads.

8.2. RECOMMENDATIONS

This section presents the recommendations for future research related to the computational modelling of auxetics. The recommendations are provided based on the findings of this thesis, and the present and future focus related to the research on auxetic materials.

Auxetic Continuum

Although the results of the computational analyses of an auxetic continuum model for static loading and one dimensional wave problem was found to be consistent with the theoretical predictions, the numerical model of an unconstrained wave motion suffered from spurious modes. The use of Modal analysis and the B-bar method reduced the problem to some extent, but these additional techniques are not robust enough as the results on the top edge were still found to be mesh dependent and subjected to spurious modes. It is recommended to further develop the computational approaches with additional kinematic constraints on the top edge to get rid of spurious modes and have mesh independent results.

The results from the beam impact analysis showed that the waves travel faster but with the reduced intensity with the increase in auxeticity. Based on the principle of the conservation of energy the increase in the kinetic energy in auxetic materials is compensated by the decrease in potential(deformation) energy. This finding indicated the possible use of auxetic as a mechanical transformer. Therefore, the new research could be focused on having in depth study about this particular aspect as well.

Micro-structure Static Analysis

The research on a re-entrant honeycomb structure in this thesis was based on an ordered structure. A re-entrant honeycomb unit cell was repeated uniformly along X1 and X2 directions to form a structural component. The possibility of achieving auxeticity in a disordered or a less ordered assembly of re-entrant honeycomb unit cells could be investigated. The study of disordered structure would be closer to reality as seldom a real structure is an assembly of perfectly ordered unit cells. Besides, this thesis only focused on a re-entrant honeycomb structure loaded in shear in X1 direction. It is evident from the configuration of a re-entrant honeycomb unit cell that the structure can be loaded in shear in X2 direction as well. It is recommended to investigate the response of a re-entrant honeycomb structure when loaded in shear in X2 direction. This study would also provide results to examine the shear wave velocity in X2 direction and not just X1 direction.

The present research was based on the computational modelling of a two dimensional re-entrant honeycomb structure. The effective mechanical properties and deformation behavior were found to be in agreement with the theory. However, the detailed understanding of a material can only be obtained with an analysis of a three dimensional structure. It is recommended to extend the present study to the computational analysis of a three dimensional auxetic structure. The computational tool developed during the research then would need extensive modification to incorporate higher order element types.

The results of the numerical analyses of a re-entrant honeycomb structure exhibited the orthotropic properties it possesses. The direct and simple relation of a Poisson's ratio and remaining mechanical properties such as indentation resistance, fracture toughness, shear resistance etc. is only available for isotropic materials. However, since the available auxetics are strongly anisotropic in nature, the available simple relations can not be used. Therefore, the orthotropic characteristics of a re-entrant structure is also one of the restraining factor for not being able to unfold the deformation behavior and mechanics of auxetics. It is recommended to study the possibility of achieving isotropic auxetic cellular structure by modifying the existing design of cellular structures.

Micro-structure Dynamic Analysis

The dynamic analysis of a beam impact problem on an auxetic continuum model showed the interesting prospects of the use of auxetics in mitigating impact forces. Similarly, the comparison of the results from a cellular model and an equivalent continuum model showed that the two models give consistent results with respect to each other. Therefore, it is recommended to perform a dynamic analysis of a beam impact problem on a cellular model. As the auxeticity in practice is achieved through cellular structures, the study is expected to provide a better insight into the real applications of auxetic structures. During this study it should be noted that the analysis would be computationally too expensive and it might be necessary to develop advanced computational tools to not have same problems as experienced in the continuum analysis of a beam impact problem.

This thesis only focused on the wave propagation characteristics and apparent wave speed in re-entrant honeycomb structures. Although these investigations provide insights in one of the most important aspects of dynamics study, other aspects of the dynamic characteristics of re-entrant structures are still uncovered domain. In this thesis, the dynamic load that was applied on a re-entrant structure had the wavelength smaller than the unit cell size. It is recommended to investigate the effect of wavelength larger than the unit cell size. Also, the possible use of auxetic structures to mitigate impact loading increases the relevance of studying the energy absorption characteristics of auxetic structures. In addition, auxetic structures subjected to high impact load would be expected to have degradation of material properties thus revealing the need of investigating physical nonlinear behavior of auxetic structures.

The study of the wave propagation characteristics showed that the processes of wave reflection, transmission and mode conversion occur at the connection of cell members. The connection nodes were modelled as fully stiff nodes for this thesis. From the design and practical application point of view it is important to investigate the effect of the rigidity of the connection nodes. It would be interesting to examine the behavior of re-entrant structure with not fully stiff connection when subjected to dynamic loading condition. It is highly recommended to study if the structure collapses immediately or does the collapse occur only at the high frequency load and the structure can sustain the load with low frequency load.

The research on auxetic structure is still new and many questions need to be answered before its extensive use in the industry. Hopefully in the near future the mysteries of auxetics will be unfolded further and they will be used in the wider range of applications.

BIBLIOGRAPHY

[1] KL Alderson, A Alderson, PJ Davies, G Smart, N Ravirala, and G Simkins. The effect of processing parameters on the mechanical properties of auxetic polymeric fibers. *Journal of materials science*, 42(19):7991–8000, 2007.

[2] Alderson A Evans Kenneth E. Auxetic Materials, Functional Materials and Structure From Lateral Thinking. *Advanced Materials*, 12(9):617–628, 2000.

[3] L. J. Gibson, M. F. Ashby, G. S. Schajer, and C. I. Robertson. The Mechanics of Two-Dimensional Cellular Materials. *Proceedings of the Royal Society A: Mathematical, Physical and Engineering Sciences*, 382(1782):25–42, 1982.

[4] Lorna J Gibson. A dissertation submitted to the University of Cambridge for the Degree of Dbctor of Philosophy Churchill College August 1981. 1981.

[5] Lorna J Gibson and Michael F Ashby. *Cellular solids: structure and properties*. Cambridge university press, 1999.

[6] Stefano Gonella and Massimo Ruzzene. Analysis of in-plane wave propagation in hexagonal and re-entrant lattices. *Journal of Sound and Vibration*, 312(1-2):125–139, 2008.

[7] A. Hönig and W. J. Stronge. In-plane dynamic crushing of honeycomb. Part I: Crush band initiation and wave trapping. *International Journal of Mechanical Sciences*, 44(8):1665–1696, 2002.

[8] Jian Huang, Qiuhua Zhang, Fabrizio Scarpa, Yanju Liu, and Jinsong Leng. In-plane elasticity of a novel auxetic honeycomb design. *Composites Part B: Engineering*, 110:72–82, 2017.

[9] H MA Kolken and AA Zadpoor. Auxetic mechanical metamaterials. *RSC Advances*, 7(9):5111–5129, 2017.

[10] Michael J. Leamy. Exact wave-based Bloch analysis procedure for investigating wave propagation in two-dimensional periodic lattices. *Journal of Sound and Vibration*, 331(7):1580–1596, 2012.

[11] Teik-Cheng Lim. *Auxetic Materials and Structures*. Springer, 2014.

[12] Zi Xing Lu, Xiang Li, Zhen Yu Yang, and Fan Xie. Novel structure with negative Poisson's ratio and enhanced Young's modulus. *Composite Structures*, 138:243–252, 2016.

[13] I. G. Masters and K. E. Evans. Models for the elastic deformation of honeycombs. *Composite Structures*, 35(4):403–422, 1996.

[14] Mariam Mir, Murtaza Najabat Ali, Javaria Sami, and Umar Ansari. Review of mechanics and applications of auxetic structures. *Advances in Materials Science and Engineering*, 2014:1–18, 2014.

[15] A. Srikantha Phani, J. Woodhouse, and N. A. Fleck. Wave propagation in two-dimensional periodic lattices. *The Journal of the Acoustical Society of America*, 119(4):1995–2005, 2006.

[16] Yunan Prawoto. Seeing auxetic materials from the mechanics point of view: A structural review on the negative Poisson's ratio. *Computational Materials Science*, 58:140–153, 2012.

[17] Krishna Kumar Saxena, Raj Das, and Emilio P. Calius. Three Decades of Auxetics Research Materials with Negative Poissons Ratio A Review. *Advanced Engineering Materials*, 18(11):1847–1870, 2016.

[18] V P W Shim, Y B Guo, and X L Teng. Elastic Wave Propagation in Honeycomb Structures.

[19] Mozafar Shokri Rad, Yunan Prawoto, and Zaini Ahmad. Analytical solution and finite element approach to the 3D re-entrant structures of auxetic materials. *Mechanics of Materials*, 74:76–87, 2014.

[20] Chris W Smith, JN Grima, and KenE Evans. A novel mechanism for generating auxetic behaviour in reticulated foams: missing rib foam model. *Acta materialia*, 48(17):4349–4356, 2000.

[21] Biyu Tian. *Numerical simulation of elastic wave propagation in honeycomb core sandwich plates*. PhD thesis, Châtenay-Malabry, Ecole centrale de Paris, 2012.

[22] F P van der Meer. Lecture notes. *CIE5144: Stability of Structures - Delft University of Technology*, February, 2017.

[23] F P van der Meer. Matalab finite element code for analysis of frames. *CIE5144: Stability of Structures - Delft University of Technology*, June, 2017.

[24] Zhengyue Wang and Hong Hu. Auxetic materials and their potential applications in textiles. *Textile Research Journal*, 84(15):1600–1611, 2014.

[25] Garth N Wells. Matalab finite element code. *CIE5123: Introduction to Finite Element Method - Delft University of Technology*, 2005.

[26] Chulho Yang, Hitesh D. Vora, and Young Chang. Behavior of auxetic structures under compression and impact forces. *Smart Materials and Structures*, 27(2):25012, 2018.

[27] Shu Yang, Chang Qi, Dong Ming Guo, and Dong Wang. Energy Absorption of an Re-Entrant Honeycombs with Negative Poisson's Ratio. *Applied Mechanics and Materials*, 148-149:992–995, 2012.

A

VERIFICATION OF DYNAMIC FE CODE FOR CONTINUUM

The finite element code programmed by Wells [25] for the course CIE 5123 Introduction to Finite Element Method at Delft University of Technology was used in the thesis. The code programmed by Wells only included static analysis. The script to run Dynamic analysis using Explicit Scheme and Newmark Implicit scheme was programmed during the thesis. In addition, stress recovery at nodes was also programmed to extract element stresses at nodes. The programmed section was verified using different numerical techniques and by comparing results with commercial finite element software, DIANA. As it is not possible to input negative Poisson's ratio in analysis of isotropic material in DIANA, the validation was done based on positive value of Poisson's ratio. First, time step sensitivity analyses are run in MATLAB using Implicit time integration scheme and Explicit time scheme integration scheme. The results obtained from simulations in MATLAB code are compared with the theoretical predictions. Later, the results obtained from MATLAB code are compared with the results obtained from DIANA software.

TIME STEP SENSITIVITY ANALYSIS FOR IMPLICIT DYNAMIC ANALYSIS

Time step sensitivity analysis in implicit time integration scheme is adopted as the first validation technique. A bar 1 m long, 0.1 m high and unit thickness is modelled using four noded quadrilateral elements. The plain strain condition is used for the two-dimensional problem. A uniaxial strain boundary condition is enforced in the model, that is, the bar is only allowed to deform in longitudinal direction. The vertical displacement is restrained in all nodes. The left end of the bar is fixed in horizontal direction as well, and the right end is subjected to dynamic load. The bar is discretized into 80 elements along the length and 1 element along the height. The model showing the loading and boundary conditions, and the load-time profile applied at the right end of the bar is shown in figure A.1.

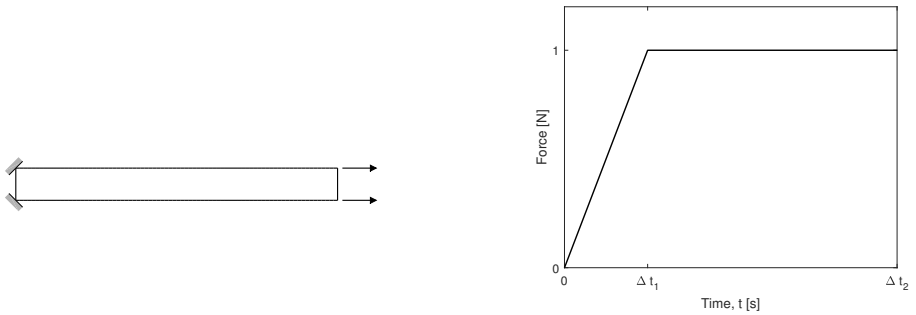

(a) Computational model of the bar

(b) Load time profile used in dynamic analysis

Figure A.1: Computational model of the bar and load profile used in dynamic analysis

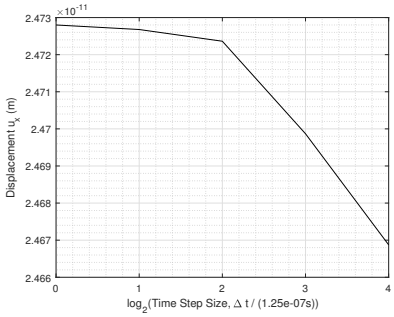

Figure A.2: Time Step Sensitivity Analysis using Implicit Scheme

The material properties used in the analysis are: Elastic Modulus (E) = 2e11 Nm^{-2}, density (ρ) = 7800 kgm^{-3} and Poisson's ratio ν = 0.45. Newmark time integration scheme was used with β = 0.25 and γ = 0.5. As this combination of β and γ results in unconditionally stable Newmark method, the time step size can be considered independently.

The analysis is run with five different time step sizes i.e. [1.25e-7 s, 2.5e-7 s, 5e-7 s, 1e-6 s, 2e-6 s]. The analysis is run upto 2e-4 s. The loading profile used in the analysis is such that the distributed load has a rise time of 2e-5 s to reach the value of 1 Nm^{-1}. After 2e-5 s, the load stays constant at 1 Nm^{-1}. The displacement of the node at the bottom edge in the right end is observed at the end of the analysis. After five analyses, the displacement observed at the considered node is plotted against the corresponding time step size. The result is shown in figure A.2. The results tend to converge with the smaller time step size as expected.

TIME STEP SENSITIVITY ANALYSIS FOR EXPLICIT DYNAMIC ANALYSIS

The model described in previous section is now analyzed using Explicit time integration scheme. The analysis is run for all five time step sizes mentioned above i.e. [1.25e-7 s, 2.5e-7 s, 5e-7 s, 1e-6 s, 2e-6 s]. The loading condition, boundary condition and material properties are kept the same. Also, the node and the time step at which the displacement is observed after the analysis is kept the same. The results of times step sensitivity analysis using explicit time integration scheme is shown in figure A.3. The figure A.3(a) shows the results including all five time step sizes, whereas the figure A.3(b) shows the results including the time step sizes [1.25e-7 s, 2.5e-7 s, 5e-7 s] only.

It can be observed in the figure that the results of the analyses using Δt equal to 1e-6 s or 2e-6 s, are not stable. The displacement is observed to be in the order of 10^{27} m while using those time step sizes. Whereas, the results of the analysis while using Δt equal to 1.25e-7 s or 2.5e-6 s or 5e-7 s follow the expected trend. The displacement is in the order of 10^{-11} m as observed from the implicit time integration scheme. For these values of time step sizes, the results tend to converge for the smaller time step size.

This observation can be explained based on the time step restriction of the explicit time integration scheme. In an explicit time integration scheme, the adopted time step size cannot be larger than the critical time step. If the time step size is larger, it leads to unstable result as observed in figure A.3(a). The critical

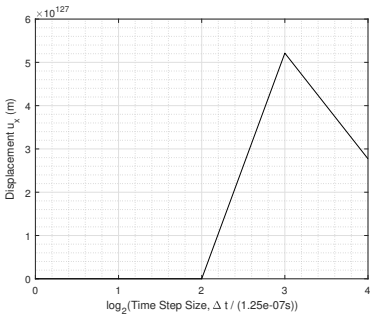

(a) Sensitivity Analysis including $\Delta t > t_{cr}$

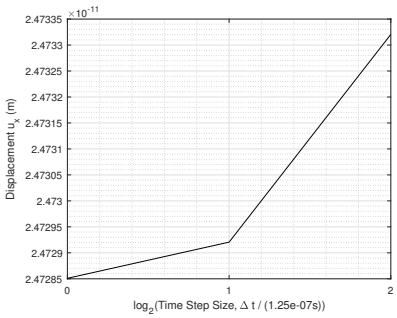

(b) Sensitivity Analysis excluding $\Delta t < t_{cr}$

Figure A.3: Time Step Sensitivity Analysis using Explicit Scheme

time step for the considered model was computed to be 7e-7 s. As time step sizes [1.25e-7 s, 2.5e-7 s, 5e-7 s] are smaller than the critical time step, correct results are obtained for these time step sizes as shown in figure A.3(b). However, the time step size [1e-6 s, 2e-6 s] are greater than the critical time step size (Δt_{cr}). Therefore, the results are numerically amplified during the analysis.

The results obtained from both explicit and implicit time integration scheme satisfies the theoretical predictions. Therefore, it provides a basis for the validation of the code. Now, the results obtained from the MATLAB code are compared with the results from DIANA as final part of the validation.

Comparison of MATLAB results and DIANA results

Th bar described previously is modelled in DIANA. The boundary conditions and material properties are kept the same. The right edge of the bar is subjected to dynamic loading. The load has a rise time of 1e-5 s to reach 1 Nm^{-1}. The load then stay constant for the rest of the analysis. The time step used in the analysis is Δt = 5e-7 s. As similar modelling technique and modelling parameters are used in both analyses, the results are expected to be same as well.

As an output, horizontal stress (S_{xx}) is observed at the bottom edge of the bar at various time steps. The results are used for the comparison and to observe the propagation of the horizontal stress along the length of the bar. The results obtained at 90th, 200th, 250th and 300th time steps from MATLAB code and DIANA are shown in figure A.4. These results highlight the propagation stages of the stress along the length of the bar. At 90th time step, the wave is observed to be propagating towards the fixed end. The wave reaches the fixed end at 200th time step and reflects towards the free end. When the wave reflects from the fixed end, the horizontal stress doubles as expected from the theory. The process of wave propagation can be described by using the wave image technique as well. The results in 250th and 300th time step shows the reflected stress wave propagating towards the loaded end.

The horizontal stress computed at four integration points were extrapolated to the nodes and compared using DIANA and MATLAB. It can be observed in figure A.4 that the results obtained from both the sources overlap each other. As the results obtained from MATLAB code agrees with the theoretical explanation and results from a commercial finite element software, it can be concluded that the code programmed for dynamic analysis is validated.

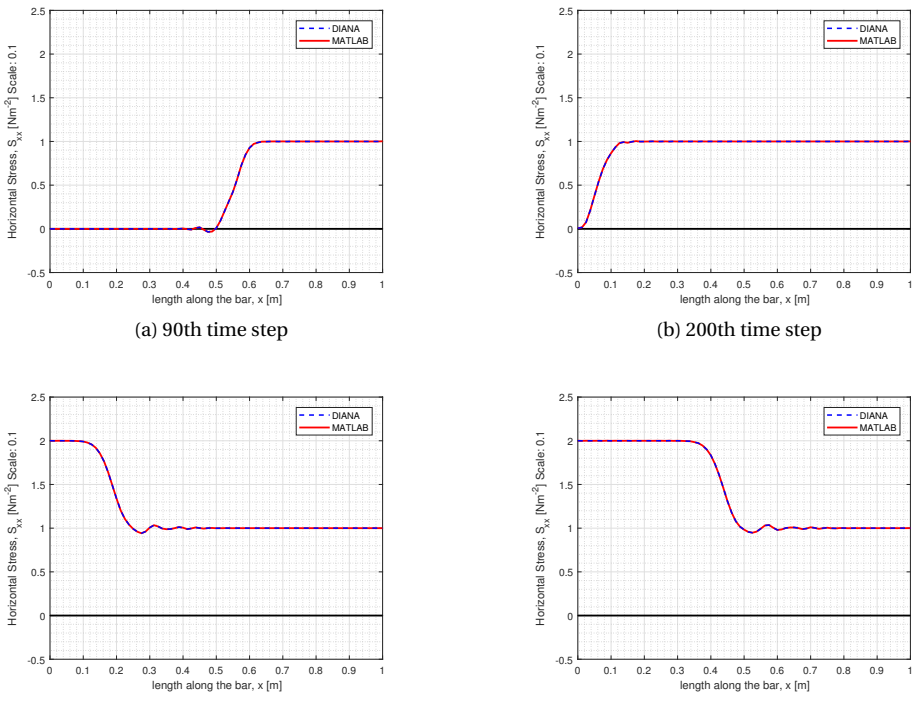

(a) 90th time step

(b) 200th time step

(c) 250th time step

(d) 300th time step

Figure A.4: Horizontal Stress - time graph at the bottom edge at various time steps

B

VALIDATION OF DYNAMIC FE CODE FOR BEAM

The finite element code programmed by van der Meer [23] for the course CIE 5144 Stability of Structures at Delft University of Technology was used in the thesis for numerical analysis of cellular structures. Various modifications were done in the code throughout the thesis. The main addition to the code was the inclusion of Dynamic Analysis. The results obtained from the code programmed in MATLAB were compared with the results from DIANA software to validate the code.

A re-entrant structure is modelled in both MATLAB and DIANA using 10 unit cells along the X1 direction. A unit cell comprises of two horizontal cell members of length 200 mm and four inclined cell members of length 100 mm. The angle between the horizontal and inclined members is adopted as $\theta = -cos^{-1}(0.6)$. The thickness of all cell members is 10 mm and the out of plane width is equal to 100 mm. The mechanical properties of the cell wall members used in the model are: Elastic modulus E_s = 2e8 Nm^{-2}, density ρ = 1 kgm^{-3} and Poisson's ratio $v_s = 0$.

The cell members are modelled using linear beam element in MATLAB code. The beam element is programmed using timoshenko beam theory. The element type and its formulation is briefly described in box 5.1.1. The cell members in DIANA is modelled using similar finite element type. The finite element used to model the cell member in DIANA is called Class III beam element. The element has two nodes and three degrees of freedom at each node.

Each cell member in the re-entrant structure is discretized into 8 elements. The cell members are rigidly connected to each other at all connections. The bottom edge of the model is restrained in vertical direction. In addition, one of the corner node at the bottom edge is restrained in horizontal direction to avoid rigid body translation. The model is subjected to vertical compressive load at the top. The dynamic load is applied to the corner nodes at the top edge. The load has a rise time of 5μ s to the value of 10 N, stays constant for next

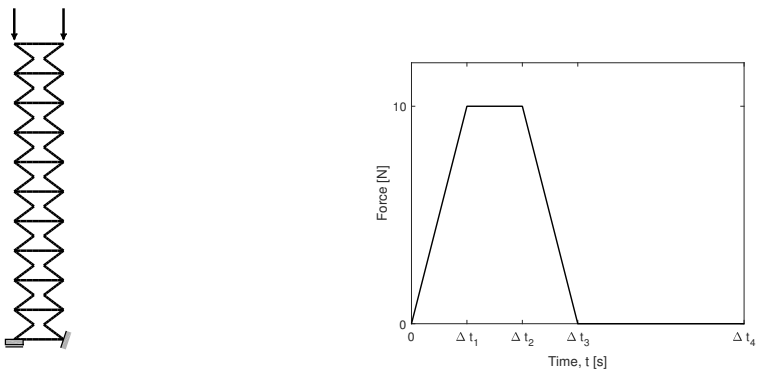

(a) Model of re-entrant structure

(b) Load Profile used in dynamic analysis

Figure B.1: Model of re-entrant structure and load profile used in dynamic analysis

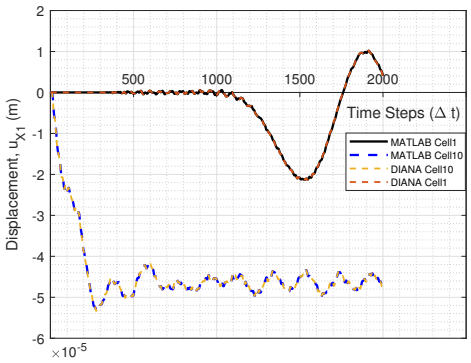

Figure B.2: Displacement time graph of two nodes in 1st and 10th cell to compare results from DIANA and MATLAB

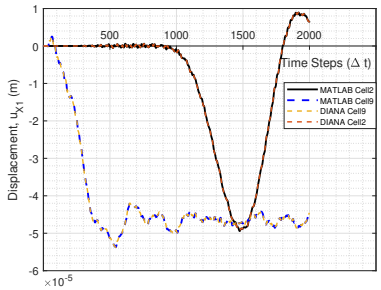

(a) 2nd and 9th cell

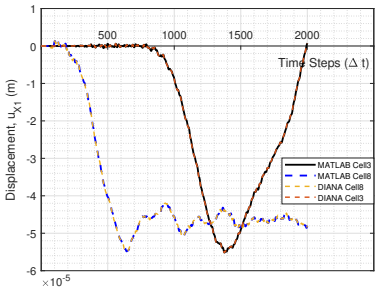

(b) 3rd and 8th cell

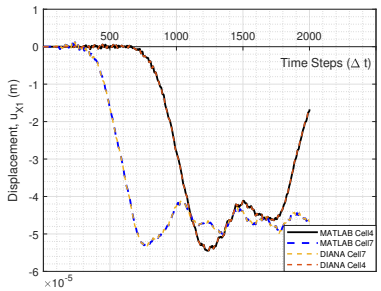

(c) 4th and 7th cell

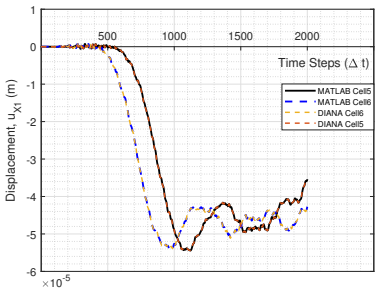

(d) 5th and 6th cell

Figure B.3: Displacement time graph of various nodes to compare results from DIANA and MATLAB

5μ s and falls to 0 N again in 5μ s. The analyses are run for 2000 time steps in both the models. The model of the re-entrant structure and load profile is shown in figure B.1.

The displacement time graph is obtained as the output of the analyses for comparison of results from MATLAB code and DIANA software. The displacement in X1 direction (i.e. vertical direction) is observed at the connection of two inclined members. The re-entrant structure is modelled using 10 unit cell members. These unit cells are numbered from 1 to 10, with 1 representing the unit cell at the bottom edge and 10 representing the unit cell at the top edge. The displacement in X1 direction is observed at 10 connection of inclined members on the right edge. The result can also be used to estimate the wave velocity in X1 direction as discussed in Chapter 5.

The results of the displacement in X1 direction at the connection of inclined members in cell 1 and cell 10 is shown in figure B.2. The results from both MATLAB and DIANA are shown in the figure. It can be observed that results from both the sources overlap each other. To increase the consistency of the results, the comparison is done for the remaining connection nodes as well. The displacement in X1 direction observed

at the connection of inclined members in Cell 2 and Cell 9, Cell 3 and Cell 8, Cell 4 and Cell 7, and Cell 5 and Cell 6 is shown in figure B.3. The results from MATLAB analysis is found to be equal to the corresponding results obtained from the dynamic analysis in DIANA. In addition to this, the MATLAB code was also used in various cases for the validation, such as: computing the longitudinal and shear wave velocity in a beam member, time sensitivity analysis in implicit time integration method, and time sensitivity analysis in explicit time integration method using time step size higher and lower than critical time step. All results were found to be positive thus validating the finite element code.

Besides dynamic analysis, other addition to the code were mesh and model generation tool for re-entrant structure with θ and h/l as the parameters, and various post processing tools.

C

IRREDUCIBLE ZONE OF FIRST BRILLOUIN ZONE

The corners of the first Brillouin zone are represented in terms of the reciprocal basis vectors $\mathbf{x_1^\star}$ and $\mathbf{x_2^\star}$. The derivation is based on a conventional honeycomb. However, as it is already known that the re-entrant honeycomb can simply be obtained by using a re-entrant angle instead of the positive angle, the derivation holds true for the re-entrant honeycomb structure as well. Also the dimensions of the cell member are represented in terms of h and l. Thus, the outcome of this derivation can be used for any general hexagonal honeycomb structure.

A two dimensional hexagonal cellular structure can be defined by three different direct lattice vectors. The three different lattice vectors and their corresponding reciprocal lattice are shown in figure C.1. The direct lattice vector are represented by subscript and the reciprocal lattice vectors are represented by superscript. In this derivation, three different lattice vectors are represented by $(\mathbf{x_1}, \mathbf{x_2})$, $(\mathbf{y_1}, \mathbf{y_2})$ and $(\mathbf{z_1}, \mathbf{z_2})$. Similarly, the corresponding reciprocal lattice vectors are represented as $(\mathbf{x_1^\star}, \mathbf{x_2^\star})$, $(\mathbf{y_1^\star}, \mathbf{y_2^\star})$, and $(\mathbf{z_1^\star}, \mathbf{z_2^\star})$.

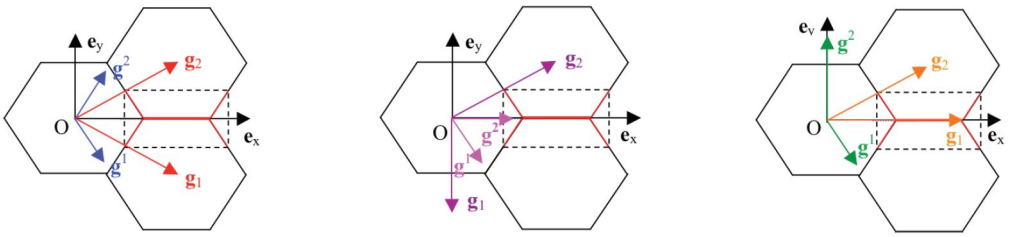

Figure C.1: Different direct lattice vectors and their corresponding recirprocal lattice [21]

Considering O as the center of the first Brillouin zone, reciprocal primitive cell is constructed for each set of reciprocal lattice vectors. The zone which is formed from the intersection of three reciprocal primitive cell is the first Brillouin zone of the hexagonal honeycomb structure. The first Brillouin zone for a conventional hexagonal honeycomb is shown in figure C.2. Z_1, Z_2, Z_3, Z_4, Z_5, Z_6 are the corners of the first Brillouin zone.

To reduce the size of the problem, the Bloch wave vector $\mathbf{k}$ is only varied in a part of the first Brillouin zone. The subdomain where the wave vector is varied is known as an irreducible zone of the first Brillouin zone. Contour in any one of the four quadrants of the first Brillouin zone can be considered as the irreducible zone. The wave vector $\mathbf{k}$ is varied along the edges of the contour in the first quadrant of the first Brillouin zone. Therefore, the position of the corners of the contour in the first quadrant O, Z_2, Z_3 and Z_0 (the intersection of edge Z_3 Z_4 with the axis e_x) is determined with respect to reciprocal lattice basis $\mathbf{x_1^\star}$ and $\mathbf{x_2^\star}$.

The direct lattice vectors $(\mathbf{x_1}, \mathbf{x_2})$, $(\mathbf{y_1}, \mathbf{y_2})$ and $(\mathbf{z_1}, \mathbf{z_2})$ represent the lattice vectors shown in figure C.1, left to right respectively. Three lattice vectors are represented in Cartesian basis as:

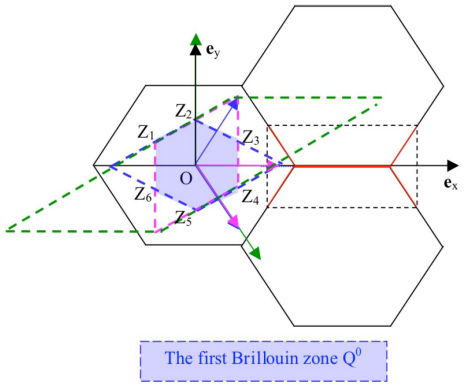

Figure C.2: First Brillouin zone of conventional hexagonal honeycomb [21]

$$\mathbf{x_1} = \begin{bmatrix} lcos\theta \\ h + lsin\theta \end{bmatrix}, \qquad \mathbf{x_2} = \begin{bmatrix} -lcos\theta \\ h + lsin\theta \end{bmatrix} \tag{C.1a}$$

$$\mathbf{y_1} = \begin{bmatrix} lcos\theta \\ 0 \end{bmatrix}, \qquad \mathbf{y_2} = \begin{bmatrix} -lcos\theta \\ h + lsin\theta \end{bmatrix} \tag{C.1b}$$

$$\mathbf{z_1} = \begin{bmatrix} 0 \\ h + lsin\theta \end{bmatrix}, \qquad \mathbf{z_2} = \begin{bmatrix} -lcos\theta \\ h + lsin\theta \end{bmatrix} \tag{C.1c}$$

The corresponding reciprocal lattice vectors are represented by $(\mathbf{x_1^\star}, \mathbf{x_2^\star})$, $(\mathbf{y_1^\star}, \mathbf{y_2^\star})$, and $(\mathbf{z_1^\star}, \mathbf{z_2^\star})$. The relation between direct lattice vectors and their corresponding reciprocal lattice vectors is give in equation 7.6. Using equation C.1 and 7.6, the reciprocal lattice vectors are obtained as:

$$\mathbf{x_1^\star} = \begin{bmatrix} \frac{1}{2lcos\theta} \\ \frac{1}{2(h+lsin\theta)} \end{bmatrix}, \qquad \mathbf{x_2^\star} = \begin{bmatrix} \frac{-1}{2lcos\theta} \\ \frac{1}{2(h+lsin\theta)} \end{bmatrix} \tag{C.2a}$$

$$\mathbf{y_1^\star} = \begin{bmatrix} \frac{1}{lcos\theta} \\ \frac{1}{h+lsin\theta} \end{bmatrix}, \qquad \mathbf{y_2^\star} = \begin{bmatrix} 0 \\ \frac{1}{h+lsin\theta} \end{bmatrix} \tag{C.2b}$$

$$\mathbf{z_1^\star} = \begin{bmatrix} \frac{1}{lcos\theta} \\ \frac{1}{h+lsin\theta} \end{bmatrix}, \qquad \mathbf{z_2^\star} = \begin{bmatrix} \frac{-1}{lcos\theta} \\ 0 \end{bmatrix} \tag{C.2c}$$

The goal is to express the position of corners of the irreducible zone of the first Brillouin zone in terms of $\mathbf{x_1^\star}$ and $\mathbf{x_2^\star}$). Therefore, the remaining reciprocal lattice vectors are first represented in terms of $\mathbf{x_1^\star}$ and $\mathbf{x_2^\star}$). Using expressions shown in C.2, following relations could be established:

$$\mathbf{y_1^\star} = 2\mathbf{x_1^\star} \tag{C.3a}$$

$$\mathbf{y_2^\star} = \mathbf{x_1^\star} + \mathbf{x_2^\star} \tag{C.3b}$$

$$\mathbf{z_1^\star} = 2\mathbf{x_1^\star} \tag{C.3c}$$

$$\mathbf{z_2^\star} = -\mathbf{x_1^\star} + \mathbf{x_2^\star} \tag{C.3d}$$

The position of the point O is (0,0). The position of the point Z_0 is $\frac{1}{2}\mathbf{y_2^\star}$. Using equation C.3, the position of point Z_0 in terms of the reciprocal lattice basis $(\mathbf{x_1^\star}, \mathbf{x_2^\star})$ is given by: (0.5, 0.5).

The Point Z_2 is intersection of perpendicular bisector of $-x_1^\star$ and $x_2^\star$. The edge Z_1 Z_2 is the perpendicular bisector of $x_1^\star$, and the edge Z_2 Z_3 is the perpendicular bisector of $x_2^\star$. The equation of edges Z_1 Z_2 and Z_2 Z_3 are computed in terms of Cartesian basis as:

$$y = -\frac{h + lsin\theta}{lcos\theta}x - \frac{(lcos\theta)^2 + (h + lsin\theta)^2}{4(h + lsin\theta)(lcos\theta)^2} \tag{C.4a}$$

$$y = \frac{h + lsin\theta}{lcos\theta}x + \frac{(lcos\theta)^2 + (h + lsin\theta)^2}{4(h + lsin\theta)(lcos\theta)^2} \tag{C.4b}$$

Intersection of these two lines gives the position of point Z_2 in terms of Cartesian basis. The position in terms of Cartesian basis is obtained to be: $\left(-\frac{(lcos\theta)^2+(h+lsin\theta)^2}{4(lcos\theta)(h+lsin\theta)^2}, 0\right)$. The position is now expressed in terms of reciprocal lattice vectors ($\mathbf{x_1^\star}$,$\mathbf{x_2^\star}$). Let a_1 and a_2 be defined such that:

$$a_1\mathbf{x_1^\star} + a_2\mathbf{x_2^\star} = \begin{bmatrix} -\frac{(lcos\theta)^2+(h+lsin\theta)^2}{4(lcos\theta)(h+lsin\theta)^2} \\ 0 \end{bmatrix} \tag{C.5}$$

Using equation C.1, the previous equation can be written as:

$$a_1\frac{1}{2lcos\theta} - a_2\frac{1}{2lcos\theta} = -\frac{(lcos\theta)^2+(h+lsin\theta)^2}{4(lcos\theta)(h+lsin\theta)^2} \tag{C.6a}$$

$$a_1\frac{1}{2(h+lsin\theta)} + a_2\frac{1}{2(h+lsin\theta} = 0 \tag{C.6b}$$

Solving these two simultaneous equations results to: $(a_1, a_2) = \left(-\frac{1}{4}\left(1+\left(\frac{lcos\theta}{h+lsin\theta}\right)^2\right), \frac{1}{4}\left(1+\left(\frac{lcos\theta}{h+lsin\theta}\right)^2\right)\right)$.

Finally, the position of Z_3 is found. This will complete the irreducible zone of the first Brillouin zone. The point Z_3 is the intersection of perpendicular bisector of reciprocal lattice basis $x_2^\star$ and $y_2^\star$. The edges Z_2 Z_3 and Z_3 Z_4 are the perpendicular bisectors of reciprocal lattice basis $x_2^\star$ and $y_2^\star$ respectively. The equation of edges Z_2 Z_3 and Z_3 Z_4 in terms of Cartesian basis are computed to be:

$$y = \frac{h+lsin\theta}{lcos\theta}x + \frac{(lcos\theta)^2+(h+lsin\theta)^2}{4(h+lsin\theta)(lcos\theta)^2} \tag{C.7a}$$

$$y = \frac{1}{2(h+lsin\theta)} \tag{C.7b}$$

As point Z_3 is the intersection of edges Z_2 Z_3 and Z_3 Z_4, the solution of two equations evaluated above gives the position of point Z_3 in terms of the Cartesian basis. The position in terms of the Cartesian basis is obtained as: $\left(\frac{(lcos\theta)^2-(h+lsin\theta)^2}{4(lcos\theta)(h+lsin\theta)^2}, \frac{1}{2(h+lsin\theta)}\right)$. The position of Z_3 is now determined in terms of the reciprocal lattice vectors ($\mathbf{x_1^\star}$,$\mathbf{x_2^\star}$). Let a_1 and a_2 be defined such that:

$$a_1\mathbf{x_1^\star} + a_2\mathbf{x_2^\star} = \begin{bmatrix} \frac{(lcos\theta)^2-(h+lsin\theta)^2}{4(lcos\theta)(h+lsin\theta)^2} \\ \frac{1}{2(h+lsin\theta)} \end{bmatrix} \tag{C.8}$$

Using equation C.1, the previous equation can be written as:

$$a_1\frac{1}{2lcos\theta} - a_2\frac{1}{2lcos\theta} = \frac{(lcos\theta)^2-(h+lsin\theta)^2}{4(lcos\theta)(h+lsin\theta)^2} \tag{C.9a}$$

$$a_1\frac{1}{2(h+lsin\theta)} + a_2\frac{1}{2(h+lsin\theta} = \frac{1}{2(h+lsin\theta)} \tag{C.9b}$$

Solving these two simultaneous equations results to: $(a_1, a_2) = \left(\frac{1}{4}\left(1+\left(\frac{lcos\theta}{h+lsin\theta}\right)^2\right), \frac{1}{4}\left(3-\left(\frac{lcos\theta}{h+lsin\theta}\right)^2\right)\right)$.

Therefore, the position of O, Z_2, Z_3 and Z_0 in terms of the reciprocal lattice basis ($\mathbf{x_1^\star}$, $\mathbf{x_2^\star}$) is given by: $\begin{bmatrix}0\\0\end{bmatrix}$, $\begin{bmatrix}0.5\\0.5\end{bmatrix}$, $\begin{bmatrix} -\frac{1}{4}\left(1+\left(\frac{lcos\theta}{h+lsin\theta}\right)^2\right) \\ \frac{1}{4}\left(1+\left(\frac{lcos\theta}{h+lsin\theta}\right)^2\right) \end{bmatrix}$ and $\begin{bmatrix} \frac{1}{4}\left(1+\left(\frac{lcos\theta}{h+lsin\theta}\right)^2\right) \\ \frac{1}{4}\left(3-\left(\frac{lcos\theta}{h+lsin\theta}\right)^2\right) \end{bmatrix}$ respectively.